Hamid Ghaednia
Department of Mechanical Engineering,
Auburn University,
Auburn, AL 36849

Xianzhang Wang
Department of Mechanical Engineering,
Auburn University,
Auburn, AL 36849

Swarna Saha
Department of Mechanical Engineering,
Auburn University,
Auburn, AL 36849

Yang Xu
Department of Mechanical Engineering,
Auburn University,
Auburn, AL 36849

Aman Sharma
Department of Mechanical Engineering,
Auburn University,
Auburn, AL 36849

Robert L. Jackson
Department of Mechanical Engineering,
Auburn University,
Auburn, AL 36849
e-mail: robert.jackson@eng.auburn.edu

A Review of Elastic–Plastic Contact Mechanics

In typical metallic contacts, stresses are very high and result in yielding of the material. Therefore, the study of contacts which include simultaneous elastic and plastic deformation is of critical importance. This work reviews the current state-of-the-art in the modeling of single asperity elastic–plastic contact and, in some instances, makes comparisons to original findings of the authors. Several different geometries are considered, including cylindrical, spherical, sinusoidal or wavy, and axisymmetric sinusoidal. As evidenced by the reviewed literature, it is clear that the average pressure during heavily loaded elastic–plastic contact is not governed by the conventional hardness to yield strength ratio of approximately three, but rather varies according to the boundary conditions and deformed geometry. For spherical contact, the differences between flattening and indentation contacts are also reviewed. In addition, this paper summarizes work on tangentially loaded contacts up to the initiation of sliding. As discussed briefly, the single asperity contact models can be incorporated into existing rough surface contact model frameworks. Depending on the size of a contact, the material properties can also effectively change, and this topic is introduced as well. In the concluding discussion, an argument is made for the value of studying hardening and other failure mechanisms, such as fracture as well as the influence of adhesion on elastic–plastic contact.
[DOI: 10.1115/1.4038187]

Keywords: asperity models, spherical contact, sinusoidal contact, hardness, yield strength, tangential loading, indentation, flattening, elastic–plastic

1 Introduction

Contact mechanics is critically important for a wide variety of applications, such as bearings, machine interfaces, mechanical seals, cams, electrical contacts, gears, tire/road contacts, joint structures, impact mechanics, and biomechanical systems. Physical surfaces are rarely perfectly flat where they come into contact. Surface curvature or roughness often causes the contact areas to be extremely small, and therefore, the resulting contact pressures and stresses are usually relatively high. In many cases, this results in failure or yielding in the contact regions. In metallic contacts especially, there is often plastic deformation. Such plastic deformation must be considered along with elastic deformation, and hence, metallic contacts are often labeled as elastic–plastic or elastoplastic.

This paper will summarize the state-of-the-art in the modeling of elastic–plastic contacts over a wide variety of geometries and loading situations. Specifically, it will focus on contact models for single peaks (often referred to as asperities), which can either be applied directly to single peak contact problems such as gears and rolling elements or integrated into statistical and multiscale mathematical frameworks that consider the complex case of rough surface contact. Due to the breadth of research into single asperity contact, cases of rough surface contact are only discussed briefly in Sec. 10.

Analytical solutions of contact problems are limited to very special geometries and constitutive behaviors [1–5]. Therefore, most works on elastic–plastic contact employ the finite element method (FEM) or a combination of elasticity theories and approximations (often referred to as semi-analytical models) to account for elastic–plastic behavior. Typically, a finite element model is created with the appropriate geometry, boundary conditions, mesh, and material properties. Next, a parametric study is performed by varying the material properties and geometrical parameters. Then, the outputs of the analysis, usually contact force, deformation, and contact area, are normalized in a logical way that consolidates them as much as possible. This normalization is often relative to a known elastic solution (such as Hertz contact theory) or to the initiation of plastic deformation. The initiation of plastic deformation can sometimes be found analytically by using a particular yield criterion (such as the von Mises criterion) and an appropriate elastic solution. The results of the finite element analysis (FEA) are next studied for trends and fitted to phenomenological equations. To be acceptable, such curve fits should be within a few percent of agreement with the results of the independent computational analysis. In some cases, they are also validated against experimental measurements. The goal of the phenomenological equations is to predict the behavior of elastic–plastic contact in science and engineering applications. One of the most important applications is to account for the asperity interactions between rough surfaces, which govern friction, plastic deformation, fatigue, and wear between solid surfaces.

Only a few previous reviews have been published on the topic of this paper [6–9]. These papers are over 16 years old, with minimal overlap with the current review, given considerable progress in the field of elastic–plastic contact mechanics has occurred since their publication. To achieve an even more thorough coverage over the area of contact mechanics, one could consider all four of these reviews in addition to the current paper. The review by Barber and Ciavarella [8] concentrates on elastic contact cases that include friction, wear, and roughness. The contemporaneous review by Adams and Nosonovsky [9] covers similar topics but concentrates on the forces occurring between contacting surfaces, including adhesion in elastic contact. The earlier work by Bhushan in 1998 [7] reviews the elastic–plastic contact of rough

Manuscript received September 16, 2016; final manuscript received October 4, 2017; published online November 14, 2017. Editor: Harry Dankowicz.

surfaces. The most closely related work to the current paper is the Bhushan [6] review of single asperity contacts from 1996 [6].

Bhushan and Peng [10] also reviewed the narrow area of numerical methods (including the boundary element method and the finite element method) applied to the contact mechanics of multilayered rough surfaces and should be referred to when considering that topic, although a considerable amount of work has been occurred since its publication in 2002 [11–16]. The current review will not focus on the effects of coatings or layered contacts. Recent work in the area includes research into the inception of yielding in spherical shells [17], layered elastic–plastic spherical contacts [13–16], and the indentation of thin coatings for characterization of their material properties [18,19]. Recently, Chen et al. [16] completed a work on a universal model of elastic–plastic contact of thin layered or coated spherical surfaces.

This paper is organized logically based first on the type of loading (i.e., normal or tangential) and then on the geometry of the asperity. For each asperity geometry, the regimes of elastic, elastic–plastic, and fully plastic contact may also be examined individually. Much more research has been conducted on spherical asperity geometries than any other shape. Accordingly, these are covered more extensively than other geometries in this paper. First, the results of purely normal contact problems, with no tangential load and shear traction, will be analyzed. These problems are much simpler to solve because there is only one load on the system that is coupled directly to the pressure or normal traction distribution. In contrast, when both normal and tangential tractions are present, their effects are coupled through the contact area, which makes such problems more difficult to solve.

2 Normal Cylindrical Contact

Surprisingly, little work has been published on the contact of a cylindrical geometry against a flat (also known as line contact), as shown in Fig. 1. In Fig. 1, δ is known as the interference or normal displacement, F is the contact load or force, b is the contact area half width, and L is the length of the cylinder. Perhaps this lack of work is because this contact condition is not seen much in practical situations due to misalignment and geometrical imperfections. Also, it cannot be used to consider asperities on rough surfaces, unless they are highly anisotropic. Nevertheless, such contact applies to many cases, e.g., wheel contacts, gear teeth interaction, and cylindrical roller bearings.

Many have suggested that most practical instances of cylindrical contact fall into the case of plane strain (when the ends of the cylinder are held rigid) such that there is no strain outside of the cross section perpendicular to the cylinder's axis of symmetry [5,20]. Alternatively, one might consider a cylindrical rolling element bearing to be closer to the case of plane stress, since it is unconfined at the ends and therefore should have no stress acting outside of the plane perpendicular to the cylinder's axis of symmetry. Similarly, applications such as gears and cams should be in the plane stress state because they are usually lubricated (low friction) and are unrestrained at their ends. However, even with a significant amount of friction, if two identical cylinders are in contact, there will be no relative motion between them. Therefore, two identical cylinders in contact which are unconfined at their ends will be in the plane stress state. This is the case for the meshing of two identical gears.

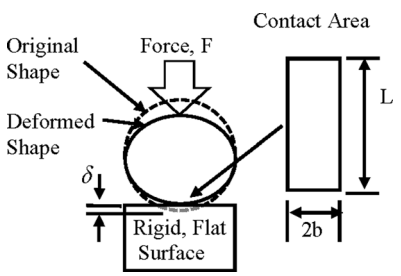

Fig. 1 Schematic of the contact between a cylinder and a flat surface. Here, *b* is the width of the contact area (often referred to as contact width), and *L* is the length of the cylinder.

The elastic solutions for a cylindrical contact geometry are well known and often attributed to Hertz [1], although it appears that he did not derive them directly, but only derived solutions for spherical and elliptical contact. It is not clear who originally analyzed the elastic cylindrical case, but Johnson [5] and Hamrock [21] both provide explicit solutions in their texts. Therefore, this review will start with Green's prediction [22] of the critical interference, δ_c, critical load, F_c, and the corresponding contact area, A_c at initial yielding of an elastic–plastic cylinder loaded against a flat surface. Here, interference or normal deflection is the distance a cylinder is translated into an opposing surface. Green used the von Mises stress criteria and the stress state from Hertz to conclude that

$$\delta_c = R\left(\frac{C_1 S_y}{E'}\right)^2\left[2\ln\left(\frac{2E'}{C_1 S_y}\right)-1\right];\quad \frac{F_c}{L}=\pi R\frac{(C_1 S_y)^2}{E'};\quad A_c = 4LR\frac{C_1 S_y}{E'} \tag{1}$$

in terms of the effective elastic modulus, E', the equivalent radius of curvature, R, the contact yield strength of the flat when the cylinder is considered rigid, S_y, where for the contact of a rigid cylinder and an elastic–plastic flat, E' and S_y are the flat's corresponding material properties, and R is the radius of the cylinder. The constant, C_1, depends on the Poisson's ratio and the assumption used to obtain two-dimensionality (i.e., plane strain or plane stress). For the plane stress condition, $C_1 = 1$, and for the plane strain condition

$$C_1 = \frac{1}{\sqrt{1+4(\nu-1)\nu}},\quad \nu \le 0.1938$$
$$C_1 = 1.164 + 2.975\nu - 2.906\nu^2,\quad \nu > 0.1938 \tag{2}$$

In the case of contact between different materials, the contact yield strength is typically assumed to equal the yield strength of the material with the lower value of $C_1 S_y$.

In the case of contact between two deformable cylinders with elastic moduli E_1 and E_2 and radii R_1 and R_2

$$\frac{1}{E'} = \frac{1-\nu_1^2}{E_1}+\frac{1-\nu_2^2}{E_2} \tag{3a}$$

$$\frac{1}{R} = \frac{1}{R_1}+\frac{1}{R_2} \tag{3b}$$

where Eq. (3*a*) is valid as shown for plane strain and axisymmetric problems. Equation (3*a*) applies to plane stress problems, such as cylindrical contact with unconfined ends and negligible friction, by setting ν_1 and ν_2 to zero. Note that Eqs. (3*a*) and (3*b*) are also valid for spherical contact and are often used when considering both elastic and elastic–plastic contact.

Although there has been some work on the use of FEM for the study of the elastic–plastic deformation of a cylinder in contact with a flat [23–26], little has been provided in the form of phenomenological equations predicting the behavior of this case. These referenced papers made useful contributions by characterizing the stress distribution of a contacting cylinder in plane strain. Cinar and Sinclair [20] compared their results to some existing theoretical predictions of hardness. For cylindrical contacts in plane strain, they found that the "hardness" or pressure was approximately $2.24S_y$. As will be discussed later, for spherical indentation the maximum pressure is approximately $2.8S_y$ [27], but varies from this value depending on the relative contact area. Slip-line theory was recently used to show that the average

pressure $\bar{p}$ during fully plastic plane strain contact is described by the following equation for the case of indentation of a rigid cylinder into a flat surface [28]:

$$\frac{\bar{p}}{S_y}=\frac{F}{2bLS_y}$$
$$=\frac{1}{2\sqrt{3}}\left(\frac{b}{R}\right)^{-1}\left[\begin{array}{l}\dfrac{\pi^2}{4}+\pi-\left(\cos^{-1}\left(\dfrac{b}{R}\right)\right)^2-2\cos^{-1}\left(\dfrac{b}{R}\right)\\ +\left\{\cos^{-1}\left(\dfrac{b}{R}\right)+1\right\}\sin\left(2\cos^{-1}\left(\dfrac{b}{R}\right)\right)+\left(\dfrac{b}{R}\right)^2\end{array}\right] \tag{4}$$

where $\bar{p}$ is the average pressure in the fully plastic regime.

Recently, Sharma and Jackson [29,30] analyzed the elastic–perfectly plastic case (with 1% bilinear hardening) in plane stress using the FEM. They considered a wide range of material properties and derived the following phenomenological equations:

$$\frac{A}{A_{\text{Hertz}}}=2\left(\frac{F}{F_c}\right)^{5/18}-1 \tag{5a}$$

$$\frac{A}{A_{\text{Hertz}}}=4.8\left(\frac{S_y}{E'}\right)^{-1/25}\left(\frac{\delta}{\delta_c}\right)^{0.106}-4.8\left(\frac{S_y}{E'}\right)^{-1/25}+1 \tag{5b}$$

relating the contact area, A, to the load, F, and interference, δ, provided that $b/R<0.4$ (the half contact width to cylinder radius ratio). It was found that the average error between the prediction of Eq. (5*a*) and the FEM results was 2.0% with a maximum error of 6.8%, while Eq. (5*b*) had an average error of 3.2% with a maximum error of 10.8%. The plane strain version of Eq. (3*a*) was used to calculate the E' in Eqs. (5*a*) and (5*b*) (i.e., the Poisson's ratios ν_1 and ν_2 were not set to zero). As predicted by these equations, the inclusion of plastic deformation will cause the contact area to be larger than in the elastic case. Very recently, this work was expanded to include the effects of strain hardening [30].

It is also interesting to note that the average normal pressure (hardness) for a cylindrical indentation contact in plane stress predicted by FEA is much smaller relative to the case of a spherical indenter (around 1.9 to 2.0 times the yield strength of the flat [29]). This also agrees with Cinar and Sinclair [20], but the magnitudes are slightly different. For the plane stress case, it is clear that hydrostatic stress cannot form in the contact, and therefore, plastic deformation from "distortion" based stress (i.e., deviatoric stress) occurs much more readily.

3 Normal Spherical Contact

Single asperity spherical contact (also known as point or Hertzian contact) is arguably the most important problem in contact mechanics and has been the concern of researchers for more than a century [5,8]. Many analytical, experimental, and numerical studies have been performed to simulate and predict various contact properties, such as the real radius of contact, stress distribution, and contact force. Spherical contact models are used by many researchers from different fields such as tribology, mechanical impact [31–35], and electrical contact [11,31,32,36–54]. Even though the spherical geometry is often used to consider asperity contact, it can also be used to consider the flattening of particles between surfaces, such as in anisotropic conductive films [51] or in the presence of wear particles [55] and nanoparticles [50]. As with the previously discussed case of cylindrical contact, spherical contact can be divided into three regimes: fully elastic, elastic–plastic, and fully plastic [5].

In the elastic regime, a closed-form analytical solution is available [1], although it is still approximate since it assumes a parabolic geometry. For the fully plastic regime, an analytical solution is only possible under simplifying assumptions, such as neglecting the effects of sink-in and pile-up. Although there have been many efforts to provide an analytical solution for the case of elastic–plastic contact, none of the presented models captures the full complexity of this condition. In the elastic–plastic regime, most of the published models simplify the analysis by studying the contact between a sphere and a flat and apply the finite element analysis to model this contact, starting with the works of Sinclair and Follansbee [56,57]. These models can be categorized into three main groups, namely, flattening models, indentation models, and more comprehensive models. In the flattening models, the flat surface is considered rigid, and the whole deformation occurs in the sphere. On the other hand, in the indentation models, the sphere is rigid, and the flat is deformable. Even though Jackson and Kogut [58] explicitly stated the differences between flattening and indentation, and the need to bridge between them, separate research on flattening and indentation has persisted without considering these differences. Only a few papers have considered general cases that account for deformation of both of the objects [32,41,59,60].

In Secs. 3.1–3.3, a summary of the investigations of the elastic regime, the fully plastic regime, and some of the most well-known elastic–plastic models is presented. The fully plastic regime is considered before the elastic–plastic regime, since it can be considered as the limit of the more complicated elastic–plastic cases. Finally, the results of original FEM simulations of three different contact cases representing flattening, indentation, and the intermediate case (by varying the ratios of yield strengths between the two bodies) are compared with the reviewed models.

3.1 Elastic Regime. For the elastic contact of two spheres, a closed-form analytical solution was provided by Hertz [1] and aroused considerable interest during the past century. Although the Hertzian theory approximates the spherical surfaces by parabolas, it is still very accurate for spheres. The Hertzian theory [1] can only be used for elastic contacts where no plasticity occurs. For contact involving metals, yield first occurs beneath the contact interface when a critical load/interference is applied and the stress state exceeds the strength of the material.

3.2 Fully Plastic Regime. Next, the fully plastic regime of normal spherical contact is examined because, along with the elastic case, it is another limit of the elastic–plastic problem. The fully plastic regime is considered reached, when plastic deformation has completely engulfed the contact area at high loads. Many researchers [5,41,52,61–73] have studied the average pressure in the fully plastic regime to match theoretical predictions against the experimental indentation results of Brinell [74] and Meyer [75]. Tabor's book on the hardness of materials has a very thorough but dated summary of this area [67]. On a side note, a popular (but erroneous) truncation model for the fully plastic regime is often incorrectly attributed to Abbott and Firestone [76]. The authors have obtained an original copy of this reference, and it appears to be on the bearing area curve used to characterize surfaces. Abbott and Firestone did not mention plastic deformation in their work.

As described earlier, flattening describes the case of a deformable sphere pressed against a rigid flat surface, while indentation describes the case of a rigid sphere pressed into a deformable flat surface. In the elastic regime, these can be considered equivalent contact conditions, but in the elastic–plastic and fully plastic regimes they differ significantly. Most work on spherical fully plastic contact has considered indentation as a way to characterize hardness (i.e., the average pressure during fully plastic contact). Hardness has historically been used as a way to define the strength of a material on its surface and actually originally derived from simple scratch tests [77]. However, it is now mostly defined as a measure of a surfaces resistance to normal indentation and varies between specific methodologies.

The hardness is defined by Meyer [75] as the contact force divided by the projected area of contact in the direction of the indentation, $F/\pi a^2$, where F is the contact force, and a is the radius of contact (i.e., hardness is the average pressure, $\bar{p}$). Alternatively, Brinell [74] suggested that hardness is the contact force divided by the total surface area of the contact.

Conventionally, from the experimental results of the Brinell indentation test by Tabor [67], the popular ratio of $\bar{p}/S_y = 2.84$ (although sometimes this is approximated as 3) was accepted for the relationship of the average pressure or hardness to the yield strength of fully plastic spherical contacts without strain hardening. This average pressure definition is now referred to as the conventional hardness. To reduce the effect of strain hardening, Tabor used work hardened materials in all of his tests. In 1944, Ishlinskii [27] provided a new way of drawing the slip lines that helped to provide an analytical model for the indentation of a rigid sphere into a fully plastic flat. Tabor's hardness ratios was also verified theoretically using slip-line theory by Ishlinskii [27], who suggested that the hardness ratio varies between 2.61 and 2.84 and does not significantly depend on the indentation depth. In 1972, Lee et al. [78] came to a similar conclusion via finite element simulations and experimental measurements of spherical indentation. However, recent studies [11,79–81] have shown the dependence of the average normal pressure on the indentation depth and deformed geometry.

Deviations from the conventional hardness value were first observed experimentally by Chaudhri et al. [81] when studying the compression or flattening of metal spheres. Mesarovic and Fleck [64,79], Ye and Komvopoulos [11], and Kogut and Komvopoulos [80] found the same trend using finite element analysis for both indentation and flattening. The effect of strain hardening was shown to counter the effect of the average pressure deviating from the conventional hardness in some cases. However, it was not theoretically understood or explained until the works of Jackson and Green [52,70,71,82]. Jackson and Green theorized that as a sphere is either flattened or indented into a surface, its geometry approaches that of a compressed column, and therefore, the contact pressure also approaches the yield strength, which is approximately one-third of the pressure obtained from a shallow spherical contact (i.e., the conventional hardness).

Storåkers et al. [83] later used theoretical similarity methods in an attempt to better describe viscoplastic contact and also included a discussion of spherical indentation. Their analysis accounted for time-dependent strain and could be applied to creep problems. They also included hardening exponents in their equations. The resulting equation for hardness or average pressure does not produce the trend of a decreasing hardness with deformation.

Based on the work of Ye and Komvopoulos [11], Kogut and Komvopoulos [80] showed that the average pressure in elastic–plastic spherical indentation often reaches a maximum value that is less than $2.84S_y$. They studied the dependence of the maximum average pressure on the material properties and proposed a phenomenological equation based on the ratio of the elastic modulus to the yield strength. However, as was shown in several subsequent papers described later, the deformed geometry is what directly affects the average pressure.

Later, Yu and Blanchard [69] investigated the same effect and provided the following equation:

$$\frac{\bar{p}}{S_y} = \frac{2}{\sqrt{3}}\left(2.845 - 0.4921\frac{a}{R}\right) \tag{6}$$

Alcalá and Esqué-de Los Ojos [61] also studied a similar effect for indentation without strain hardening and provided the following equation:

$$\frac{\bar{p}}{S_y} = 3.044 - 1.885\frac{a}{R} \tag{7}$$

Jackson and Green [52] showed that this trend occurs for flattening cases as well. Later they refined their model and proposed the following equations for the average pressure (i.e., hardness) in the fully plastic regime [53,84]:

$$\frac{\bar{p}}{S_y} = 2.84\left[1 - \exp\left(-0.82\left(\frac{a}{R}\right)^{-0.7}\right)\right] \tag{8a}$$

$$\frac{\bar{p}}{S_y} = 2.84 - 0.92\left[1 - \cos\left(\pi\frac{a}{R}\right)\right] \tag{8b}$$

Note that Eq. (8*a*) is from the original work by Jackson and Green (JG) [52], and Eq. (8*b*) is from work by Jackson et al. (JGM) [53,84]. The reason that the new equation was created is that theoretically when a/R approaches 1, the geometry approaches that of a compressed column and the average pressure should approach the yield strength. However, Wadwalkar et al. [72] showed that due to a barreling effect in flattening, R must be modified for large deformations for the average pressure to approach the yield strength when a/R approaches 1.

A recent paper by Olsson and Larsson [60] focused on modeling the contact of two elastic–plastic spheres with different radii of curvature. The authors provided an equation for the variation of the average pressure in the fully plastic regime by fitting to the finite element results from Mesarovic and Fleck [64]. Their equation is given by

$$\frac{\bar{p}}{S_y} = 3\left[1 - 0.0461\left\{\ln\left(\frac{a}{R}\right) - \ln(LD)\right\}^{2.214}\right] \tag{9}$$

provided that $a/R > LD$. For indentation, $LD = 0.1$, and for flattening, $LD = 0.041$.

Recently, Jackson et al. [2] presented a semi-analytical solution based on the slip-line theory and obtained a relation between the average pressure and the radius of contact for the indentation of a rigid perfectly plastic flat by a rigid sphere given by

$$\frac{\bar{p}}{S_y} = \frac{4}{3\sqrt{3}}\left(\frac{a}{R}\right)^{-2}\left[\frac{1}{3}\left(\frac{a}{R}\right)^{3} - \left(1 + \cos^{-1}\left(\frac{a}{R}\right)\right)\left(1 - \left(\frac{a}{R}\right)^{2}\right)^{\frac{3}{2}} - \frac{a}{R} + \frac{\pi}{2} + 1\right] \tag{10}$$

Their solution is based on the assumption of plane strain rather than axisymmetry (as these are mechanically very similar).

The comparison of Eqs. (6)–(10) with new FEM results for flattening and FEM results presented in Ref. [2] for indentation is shown in Fig. 2. The new FEM results for flattening employ a mesh of 29,541 elements and are for a material with $E/S_y = 2 \times 10^4$, to approximate the rigid perfectly plastic case and the fully plastic limit of the average pressure to yield strength ratio. The cases of indentation and flattening are compared separately in Figs. 2(*a*) and 2(*b*), respectively. It has to be noted that the FEM results presented in Ref. [2] do not represent a rigid perfectly plastic material, but are close to the fully plastic case by applying a very small yield strength relative to the elastic modulus. For indentation, Eqs. (9) and (10) appear to be closest to the FEM results. For flattening, all three models appear to be in approximate agreement when $a/R < 0.4$, with Eq. (8*b*) showing the best match. They all deviate for larger values of a/R. This may be due to large deformations of the sphere changing the effective radius, R. Notably, for low values of a/R, the average pressure to yield stress ratio approaches 2.84 [27], which differs from Eq. (9). Above $a/R = 0.4$, the original JG equation (Eq. (8*a*)) deviates from the FEM results, but the updated version (JGM, Eq. (8*b*)) shows relatively good agreement. Two versions of the FEM results are also provided. In the first version, a/R uses

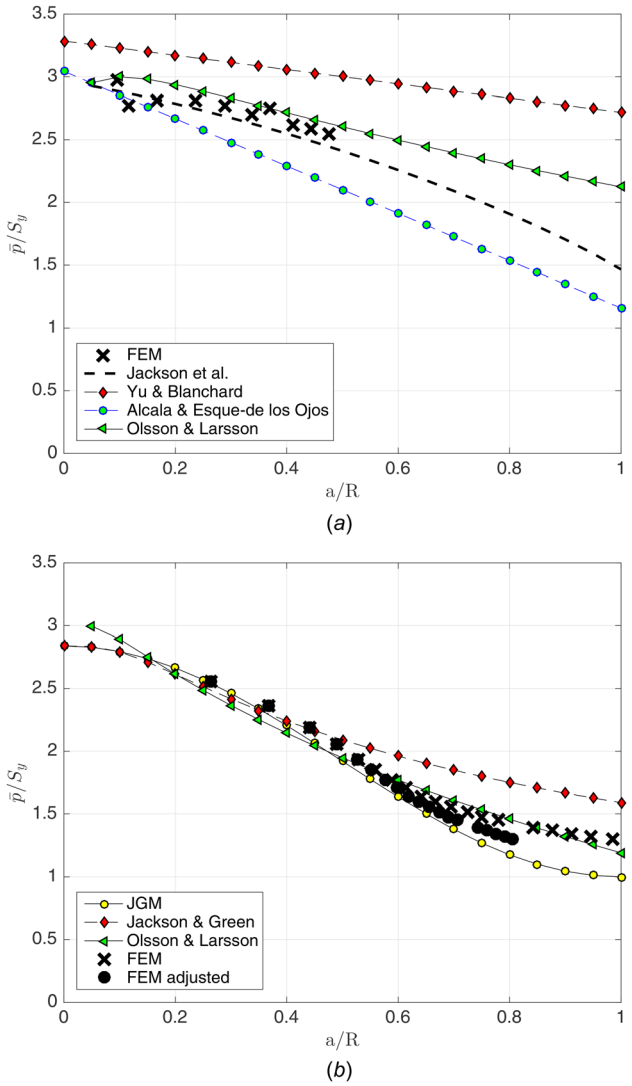

Fig. 2 Comparison between Eqs. (6) and (10) for indentation (*a*) and flattening (*b*) and with FEM results

the original radius of the sphere. The second version adjusts a/R to use the deformed radius of the sphere calculated from the base of the sphere. Both Eqs. (8*b*) and (9) fall in between these two versions. The JGM model (Eq. (8*b*)) follows the adjusted model more closely because it assumes that as contact radius, a, approaches the effective radius of the sphere, the pressure ratio will decrease to 1. The model by Olsson and Larsson (Eq. (9)) agrees better with the unadjusted FEM results because it was fit to other unadjusted FEM results.

3.3 Elastic–Plastic Regime. During contact, the material usually begins yielding at very small interferences, especially for metals. Therefore, the elastic regime only covers a small range of interferences. On the other hand, the fully plastic regime happens at very large interferences. For the majority of contacts, part of the material is in the elastic regime, and part of it undergoes plastic deformations. This is called the elastic–plastic regime. So far, there are no closed-form solutions for elastic–plastic contacts that are derived from fundamental principles.

A majority of the studies on elastic–plastic contact use finite element analysis to model, simulate, and mathematically describe the contact. In Secs. 3.3.1–3.3.5, some of the most well-known spherical contact models have been reviewed in three groups: flattening, indentation, and the general case of plastic deformation in both the flat and the sphere.

3.3.1 Spherical Indentation. The indentation of a flat by a rigid hemisphere has been studied for over a century by many researchers. As described earlier, the study of indentation contact sought to develop models for testing material hardness. In the indentation models, contact between a rigid sphere and a deformable flat is considered as shown in Fig. 3. Here, δ is the penetration, a is the radius of real contact area, a' is the radius of truncated contact area which neglects sink-in and pile-up deformations in the flat, and R is the radius of the sphere. In most experimental indentation studies, the indenter is considered to be rigid. However, elastic deformation in the indenter can cause prediction errors of up to 12%, as shown by Rodriguez et al. [59]. Since, in reality, there is no ideally rigid body, there is a need for a criterion in which the contact can be approximately defined as indentation. Tabor [66] suggested that the yield strength of a spherical indenter should equal 2.5 times that of the flat, to prevent plastic deformation of the indenter. Ghaednia et al. [41] verified that if the yield strength of the sphere is 1.7 times larger than the yield strength of the flat, the contact can be practically designated as indentation.

In 1971, Hardy et al. [85] pioneered using the FEM to analyze the indentation problem. They investigated the elastic–plastic indentation qualitatively, but did not provide any predictive formulations. Using an improved meshing scheme, Sinclair et al. [57] and Follansbee and Sinclair [56] also studied indentation using the finite element method and used this to obtain some approximate phenomenological formulations. They compared their numerical predictions with experiments [67] and other existing theories, such as Ishlinskii's [27] and Richmond's [65] slip-line theories. Per Sinclair and Follansbee, Hertzian theory applies to the elastic regime when $\bar{p}/S_{yf} \leq 1.1$, where S_{yf} is the yield strength of the flat. Similar to Johnson [5], Sinclair and Follansbee assumed the average normal pressure in the fully plastic regime to equal the conventional hardness, $\bar{p} = 2.8S_{yf}$, once the deformation reaches $aE'/RS_{yf} = 50$. However, as noted before, the assumption of a constant hardness is overly simplistic and makes predictions that can be erroneous.

In an attempt to characterize the indentation of layered surfaces, Komvopoulos and Ye [11,86] developed closed-form models by fitting phenomenological equations to finite element results. Komvopoulos and Ye [86] divided the contact into four phases: the elastic phase, the elastic–plastic small deformation phase, the elastic–plastic medium deformation phase, and the elastic–plastic large deformation phase. They define a nondimensional variable, Q, given by

$$Q = \left(\frac{E'}{S_y}\right)\left(\frac{\delta}{a'}\right), \quad a' = \sqrt{R^2 - (R-\delta)^2} \tag{11}$$

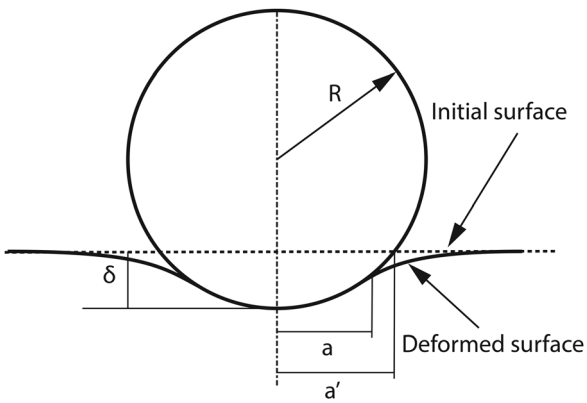

Fig. 3 In the indentation models, the sphere is rigid and the flat is deforming

and concluded that the elastic phase starts from $Q = 0$ and continues until $Q < 1.78$. Per the Hertzian contact model, in the elastic phase

$$\frac{F_e}{A} = \frac{4\sqrt{2}}{3\pi} Q S_y, \quad A = \frac{A'}{2}, \quad A' = \pi a'^2 \tag{12}$$

where F_e denotes the corresponding elastic contact force, and A and A' are the real and truncated contact areas, respectively. When $Q > 1.78$, the elastic–plastic small deformation phase persists until $Q \leq 21$. In this phase

$$\frac{F_{ep}}{A} = (0.7 \ln Q + 0.66) S_y \tag{13}$$

$$\frac{A'}{A} = 0.05(\ln Q)^2 - 0.57(\ln Q) + 2.41 \tag{14}$$

where F_{ep} denotes the corresponding elastic–plastic contact force. For $21 < Q \leq 400$, the contact is in the elastic–plastic medium deformation phase and has been considered to be consistent with the conventional hardness relation (note that this is the value assumed in their model)

$$\frac{F_{ep}}{A} = 2.9 S_y \tag{15}$$

where a is calculated from Eq. (14). For the elastic–plastic large deformation phase, when $Q > 400$, Eq. (15) is used while setting $A = A'/0.71$. Komvopolous and Ye also noted a decrease in the average pressure to yield strength ratio at large deformations. Kogut and Komvopolous [80] reformulated Komvopolous and Ye's model and not only considered loading, but the unloading phases as well.

Bartier et al. [87] also performed an experimental and numerical verification of analytical models in terms of contact radius in an indentation contact. They showed that the theoretical models, dependent only on the strain hardening exponent, overestimate the dimensionless contact radius. Another observation in their study was the coefficient of friction that had a non-negligible effect on the contact radius for large penetration depths.

By dividing the contact problem into three phases, Brake [47] recently formulated a semi-analytical model. The three phases are the elastic, elastic–plastic, and fully plastic phases. The elastic phase follows the Hertz theory, and the fully plastic phase follows Johnson's theory [5], which assumes a constant conventional hardness. Brake considered the elastic–plastic phase using a polynomial interpolation between the two limiting phases. The model was verified by the impact experiments of Kharaz and collaborators [88–90]. In a more recent work [48], Brake used the same methodology with different transition functions to connect the elastic phase and fully plastic phase. His formulation for the fully plastic phase uses the Meyer hardness exponent. Brake [48] also considered the frictional contact for the oblique impact case. This model shows an improvement over the previous model presented in Ref. [47].

3.3.2 Spherical Flattening. The case where a rigid flat is in contact with a deformable sphere is referred to as flattening and is schematically represented in Fig. 4. Note that a is the real radius of contact and δ is the relative normal displacement (i.e., the interference or penetration depth) of the sphere into the flat, if the sphere was not deforming.

As with indentation, there are still no closed-form solutions of elastic–plastic flattening problems, but there are a large number of models. Johnson [91] experimentally observed the contact of spheres and cylinders with a rigid flat in the fully plastic regime in 1968. The first elastic–plastic contact model was proposed by Chang, Etsion, and Bogy [92], often known as the CEB model. In the CEB model, the sphere remains elastic up to a critical

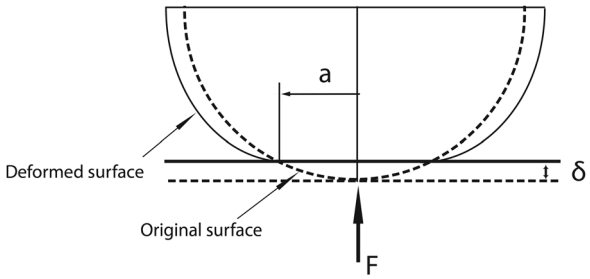

Fig. 4 In the flattening models, the flat is rigid and the sphere is deforming

interference. For larger interferences, the model imposes volume conservation of the deformed sphere during plastic deformation. It also assumes that the average pressure on the sphere is the conventional hardness and does not vary once the fully plastic regime is reached. Additionally, the contact force to interference relation, as well as the contact area to interference relation, contains a discontinuity at the transition point from elastic to plastic deformation. Zhao et al. attempted to correct this discontinuity by using a polynomial template for the transition between the elastic and plastic regimes [73]. Unfortunately, their correction was shown to compare very poorly to finite element predictions [52].

Thornton and Ning [42,43] formulated theoretical models of elastic–plastic contact with the aim of implementing them for the study of impact. With the development of the finite element method and access to computational resources, modeling capabilities were advanced by many researchers, including Li and Thornton [44], Wu et al. [45], Kogut and Etsion [93], and Jackson and Green [52]. Shankar and Mayuram [94] studied the transition from the elastic–plastic regime to the fully plastic regime based on the evolution of the plastic core. Lin and Lin [95] also examined the problem and compared their finite element results to several of the models that will be discussed later.

Although others have also made similar predictions of the critical values and initial yielding, the ones provided by Jackson and Green [52] using the von Mises yield criteria are slightly more accurate. According to their formulation, the critical value of interference at the initiation of plasticity is given by

$$\delta_c = \left(\frac{\pi C_2 S_{ys}}{2E'}\right)^2 R \tag{16a}$$

where S_{ys} is the yield strength of the sphere, E' is the effective modulus of elasticity, and

$$C_2 = 1.295 e^{0.736 \nu_s} \tag{16b}$$

where ν_s is the Poisson's ratio of the sphere. Furthermore, the critical area and the critical contact force are

$$A_c = \pi^3 \left(\frac{C_2 S_{ys} R}{2E'}\right)^2 \tag{17}$$

$$F_c = \frac{4}{3}\left(\frac{R}{E'}\right)^2 \left(\frac{C_2}{2}\pi S_{ys}\right)^3 \tag{18}$$

For the contact of two elastic–plastic bodies, it has been suggested that the yield strength of the weaker material is used for the effective yield strength in Eq. (16*a*) [96]. A better methodology is to use the lowest $C_2 S_y$ of the two materials [22].

Brizmer et al. [97] investigated the inception of yielding of spherical contact in more detail by considering the effects of brittle failure and stick on the surface. Based on a polynomial expansion, they provide an alternative equation for the case of frictionless yield inception of a spherical contact with

$C_3 = 1.234 + 1.256\nu_s$, which has a slightly larger error in comparison to the numerical solution than Eq. (16*b*). The full-stick boundary condition is then applied to the contact surface, which results in all points being rigidly conjoined once they are in contact. Brizmer et al. [97] used a finite element model to show that the stick boundary condition causes higher stresses to form in the contacting materials, which results in yield inception at lower interferences. In stick, they also found that for $\nu_s \leq 0.26$, initial yielding actually occurs on the surface, whereas for the frictionless slip case, it always occurs below the surface at the center of contact. The following equations are provided by Brizmer et al. to calculate the critical interference and force when stick is applied as the boundary condition:

$$\frac{(\delta_c)_{\text{stick}}}{\delta_c} = 6.82\nu_s - 7.83\left(\nu_s^2 + 0.0586\right) \tag{19a}$$

$$\frac{(F_c)_{\text{stick}}}{F_c} = 8.88\nu_s - 10.13\left(\nu_s^2 + 0.089\right) \tag{19b}$$

provided that $0.2 \leq \nu_s \leq 0.5$. Equations (16) and (18), along with C_3 substituted for C_2, should be used to calculate the denominators on the left side of Eqs. (19*a*) and (19*b*). Interestingly, when brittle failure is considered [97], the critical interference in stick is actually larger than that in frictionless slip, which is the reverse of the trend for ductile failure (Eq. (19*a*)).

Etsion's research group has also characterized the inception of yielding for coated or layered contacts [13–15]. Their work on layered surfaces predicts that the inclusion of a coating can actually increase the resistance of the surface to plastic deformation past that of a continuous surface composed entirely of either the substrate or coating material. There appears to be an optimal coating thickness that can be utilized by the coating industry to improve their design methodology. For instance, it has already been demonstrated that optimizing the coating thickness on machining tools can significantly prolong their lives [98].

Kogut and Etsion's [93] groundbreaking work empirically fitted the approximate solutions to the finite element results of a model of elastic–perfectly plastic contact between a hemisphere and a rigid flat. As with previous models, the elastic regime occurred at $\delta/\delta_c \leq 1$. They found it difficult to fit the results with one continuous function and therefore split the elastic–plastic regime into three divisions. The empirical equations between each division are not necessarily continuous in their values or slope at their intersection points. Additionally, Kogut and Etsion assumed an upper limit of the conventional hardness for the fully plastic pressure and set it to a constant of $2.8S_{ys}$ (which is for some cases incorrect, as discussed previously). However, the model provided by Kogut and Etsion has been shown to be very effective when $a/R < 0.1$ and it is also simple to use and incorporate into other models. The curve-fit equations of the Kogut and Etsion model are given as

$$\left(\frac{A}{A_c}\right) = 0.93\left(\frac{\delta}{\delta_c}\right)^{1.136};\quad \left(\frac{F}{F_c}\right) = 1.03\left(\frac{\delta}{\delta_c}\right)^{1.425},\quad 1 \leq \frac{\delta}{\delta_c} \leq 6$$
$$\left(\frac{A}{A_c}\right) = 0.94\left(\frac{\delta}{\delta_c}\right)^{1.146};\quad \left(\frac{F}{F_c}\right) = 1.40\left(\frac{\delta}{\delta_c}\right)^{1.263},\quad 6 < \frac{\delta}{\delta_c} \leq 110 \tag{20}$$

After $\delta/\delta_c = 110$ is exceeded, the contact is considered to be in the fully plastic regime and the average pressure is assumed to equal to the conventional hardness, i.e., $2.8S_{ys}$. Wang [99] improved the formulation of Kogut and Etsion, especially for the unloading phase that was presented in Ref. [54]. The predictions of Eq. (20), now referred to as the Kogut and Etsion model, were later confirmed using an optical measurement of the contact area [100].

Jackson and Green [52,70,71,82] also conducted a rigorous finite element analysis of the same elastic–perfectly plastic deformation of a sphere contacting a rigid flat. They proposed a new model empirically fitted to the finite element predictions. The model has been confirmed several times for a wider range of properties than considered originally, both by additional FEM results and experiments [41,70,101,102]. Although Jackson and Green again implemented the Hertz theory in the elastic regime, they suggested that the elastic phase can be effectively extended to $\delta/\delta_c \leq 1.9$. Note that Jackson and Green predicted that plastic deformation will occur below $\delta/\delta_c = 1.9$, but until this value, the amount of plastic deformation appears not to have a significant effect. After plasticity initiates and becomes significant, they suggest using the following equations for the contact force:

$$\frac{F}{F_c} = \left[e^{\left(-0.25(\delta/\delta_c)^{0.416}\right)}\right]\left(\frac{\delta}{\delta_c}\right)^{1.5} + \frac{4H_G}{C_2 S_{ys}}\left[1 - e^{\left(-0.04\left(\frac{\delta}{\delta_c}\right)^{0.55}\right)}\right]\left(\frac{\delta}{\delta_c}\right) \tag{21}$$

and the contact area

$$\frac{A}{A_c} = \frac{\delta}{\delta_c}\left(\frac{\delta}{1.9\delta_c}\right)^B \tag{22}$$

where B can be calculated as

$$B = 0.14e^{23S_{ys}/E'} \tag{23}$$

The symbol H_G/S_{ys} in Eq. (21) captures the geometrically varying hardness and is equivalent to $\bar{p}/S_y$ given by Eq. (8*b*). Substitution of Eq. (8*b*) into Eq. (21) is one of the biggest differences between Jackson and Green's model and previous models, since the former predicts that the hardness or the average pressure decreases as the contact radius increases. With larger deformations, the shape of the sphere approaches that of a cylindrical column loaded against a flat surface. In the fully plastic regime, the average pressure then decreases from the conventional hardness value of approximately $2.84S_{ys}$ as found by Tabor [67] and toward a value of S_{ys}.

Since the range of loads considered by Jackson and Green [52] were limited, Eqs. (9) and (21)–(23) are not valid beyond $a/R = 0.41$. Expanding on this work, Wadwalkar et al. [72] considered much larger loads and deformations at which the ratio of the contact radius to sphere radius was almost unity. Later, Sahoo and Chatterjee [103] also studied the effect of E'/S_y on the contact. Etsion's research group also removed the assumption of frictionless contact by considering full-stick between the surfaces [88,104]. Later, Megalingum and Mayuram [105] also revisited the spherical contact problem and confirmed that the hardness limit does not hold in the fully plastic regime. They provide a set of lengthy equations in the Appendix of their work for modeling spherical contact. The authors of the current review paper could not successfully include this model in the comparison with the other models.

Several researchers have also investigated the unloading of elastic–plastic spherical contacts [40,53,54,106]. In these works, the load is applied as before, but then it is removed incrementally to observe how the sphere recovers. In many of these works, it is assumed that the sphere recovers elastically and the Hertz model can be used to consider the elastic recovery of the sphere. Still, once the sphere is completely unloaded, a complex state of residual stresses remains in the body of the sphere due to the sustained plastic deformation. This residual stress is similar to that aimed for in the industrial practice of shot peening. Altering tensile and compressive stress regions are effective at stopping the propagation of cracks and, consequently, increasing fatigue life (i.e., cracks do not propagate in a compressive stress region).

Kadin et al. [107] found that all subsequent loading stages were elastic for both materials, with and without hardening, unless the original load is exceeded. This suggests that, in many repeated surface contacts, the deformation becomes elastic after the first

few loading cycles. Kadin et al. also postulated that a more realistic kinematic hardening law might predict continuing hardening and plastic deformation. The unloading curves predicted by the modeling of Etsion's group were later validated using an optical technique to measure contact area [106]. The experimental measurements of the unloaded and deformed radius of the spheres did not agree with the modeling predictions, perhaps due to differences in the boundary conditions at the surface.

Several unloading models were successfully used to describe the elastic recovery phase of spherical impacts [53]. The resulting models compared well with experimental measurements of the coefficient of restitution [31,32].

3.3.3 The General Case (Combined Flattening and Indentation). It was previously often assumed that the flattening and indentation models could be used for all contact cases. However, recently Ghaednia et al. [41] showed that there could be up to a 25% difference between these models, and that there is a transition phase between the flattening and indentation regimes. Jackson and Kogut [58] also found similar differences but did not provide a general model. Ghaednia et al. defined a new variable, the yield strength ratio, S_y^*, defined as the ratio of the yield strength of the sphere to that of the flat. They showed that the yield strength ratio could be used to formulate the transition between the two limiting models, i.e., flattening and indentation. The deformations of both bodies, contact radius, contact force, and hardness were analyzed. For the convenience of the comparison, the authors kept the minimum yield strength constant and changed the yield strength ratio. In this way, previous flattening and indentation models will result in the same predictions for all of the yield strength ratios. Ghaednia et al. [41] also provided phenomenological equations that were more general than the indentation and flattening models. Due to the length of these equations, they are listed in Appendix A.

A recent paper by Olsson and Larsson [60] provided a model for the elastic–plastic contact of two spheres, rather than a sphere and flat. The two spheres can also have different radii, which make this model more general. The model is based on a semi-analytical formulation and fitted to the finite element results. It appears to be aimed for use in modeling the compaction of powder. Unfortunately, the model is not in a closed form. However, it may be useful to predict the behavior of the general case. Olsson and Larsson's paper did provide a closed-form prediction of the variation of the average pressure (i.e., hardness) as a function of the deformed geometry in the fully plastic regime. Their equation was compared to others in Sec. 3.2.

Figure 5 shows the FEM predictions of the contact radius for different yield strength ratios compared to several of the discussed models. For this case, the Young's modulus and Poisson's ratio of both the sphere and the flat are $E_s = E_f = 200$ GPa and $\nu_s = \nu_f = 0.3$, respectively. The minimum yield strength is set to $S_{y,\min} = 503$ MPa, assigned to either the flat, the sphere, or both objects. The applied displacement is held constant at $0.04R$. The results show an interesting trend when the yield strength ratio is close to 1. At this point, the contact radius decreases sharply. The reason for such a trend is that the two objects then distribute and share the induced deformation thereby reducing the contact radius. Essentially, when the yield strengths are nearly equal, the amount of total plastic deformation approximately doubles at the same load compared to the ideal flattening or indentation cases.

Figure 6 shows the transition of the average normal pressure from flattening to indentation, as predicted by Ghaednia et al. [41]. For this case, the modulus of elasticity (Young's modulus) and Poisson's ratio of both the sphere and the flat are $E_s = E_f = 200$ GPa and $\nu_s = \nu_f = 0.3$, respectively. The minimum yield strength is set to $S_{y,\min} = 200$ MPa. Results show a sudden jump from the flattening regime with $\bar{p}/S_y = 2.4$ to the indentation regime with $\bar{p}/S_y = 2.7$. Note also that, for both cases, the average pressure never reaches the conventional value of the hardness or $\bar{p}/S_y = 2.84$. This is again due to relatively large deformations

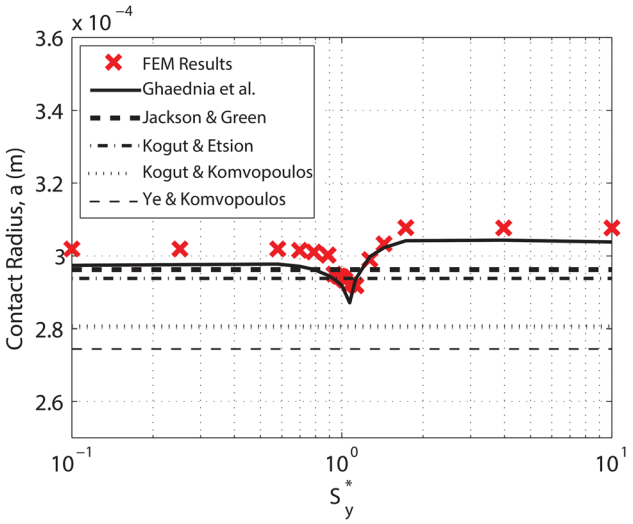

Fig. 5 Contact radius versus the yield strength ratio for a constant deflection

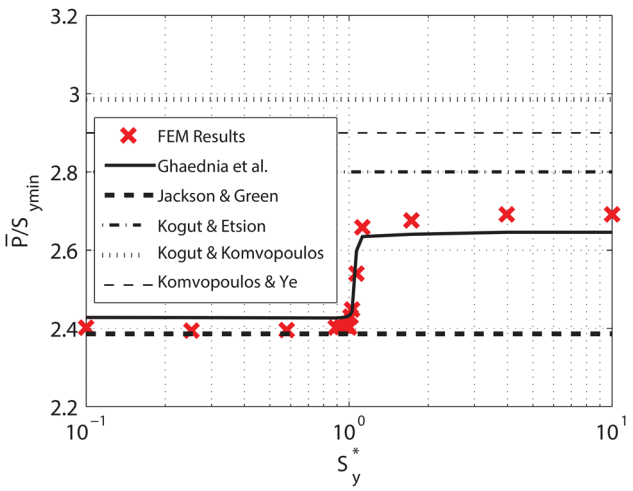

Fig. 6 Average pressure or hardness versus the yield strength ratio for spherical contact

and contact shapes morphing from that of a sphere toward a column geometry. Essentially, the angle between the surfaces at the edge of the contact is increased from very small values toward 90 deg.

Figure 7 shows the Ghaednia et al. [41] finite element predictions of the contact force for different yield strength ratios compared to several earlier models. For this case, the modulus of elasticity (Young's modulus) and the Poisson's ratio of the sphere and the flat are $E_s = 71.7$ GPa, $E_f = 200$ GPa and $\nu_s = 0.33$, $\nu_f = 0.3$, respectively. The minimum yield strength is set to $S_{y,\min} = 300$ MPa. The results show a slight decrease in force near a yield strength ratio of $S_y^* = 1$ and then a sudden increase in force in the indentation regime. This behavior during the transition is not captured by flattening or indentation contact models. However, the model provided by Ghaednia et al. agrees closely with the FEM predictions and captures the intermediate behavior between indentation and flattening.

3.3.4 Numerical Comparison of Sphere Models. Few of the well-known contact models for flattening and indentation that have been discussed in Secs. 3.3.1 and 3.3.2 have been compared to each other and to the FEM results. In this work, new numerical

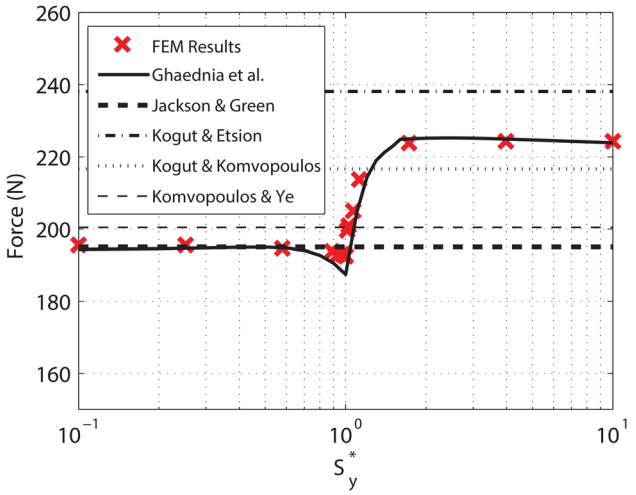

Fig. 7 Contact force versus the yield strength ratio for spherical contact

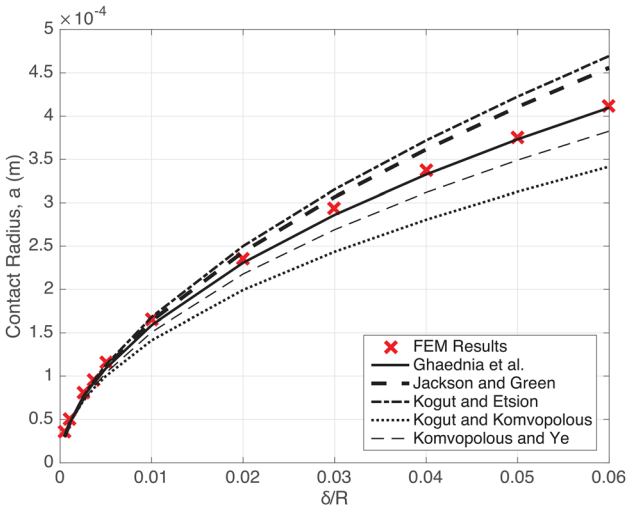

Fig. 8 Comparison between predicted contact radii during indentation for different contact models

results are obtained from finite element modeling. The same model and meshing described in Ref. [41] have been used, but the cases are different from that presented in Ref. [41]. The contact of a sphere with radius $R = 1$ mm has been modeled for two different cases: indentation, in which the flat is the weaker object (with lower yield strength), and flattening, in which the sphere is the weaker material.

Five different contact models have been studied here: the Jackson and Green [52] and Kogut and Etsion models [93] from the flattening group, the Komvopolous and Ye [11] and Kogut and Komvopolous [80] from the indentation group, and the Ghaednia et al. model [41], which is the only model that provides a closed-form formulation that considers the effect of deformation of both of the objects. A comparison between these models for impact experiments can also be found in Ref. [32].

In the case of indentation, the yield strengths of the flat and sphere are $S_{yf} = 100$ MPa and $S_{ys} = 1000$ MPa, respectively. This satisfies the criteria in Refs. [41] and [66] for an indentation, since the yield strength of the sphere is ten times larger than that of the flat. The modulus of elasticity and Poisson's ratio of both the flat and the sphere are $E = 200$ GPa and $\nu = 0.3$, respectively. The contact force and radius of contact have been analyzed for deformations from $\delta/R = 0.0005$ to $\delta/R = 0.06$. Note that the radius of contact here is the radius as projected onto the original flat plane. One should consider that because of the relatively small yield strength of the flat, the deformations are mostly in the elastic–plastic regime.

Figure 8 shows the contact radius as a function of displacement during indentation. The FEM results shown in this figure are obtained for a model developed for this specific comparison rather than from any of the models used in previous publications. Both of the flattening models [52,93] show larger contact radius values than the FEM results, while both of the indentation models predict smaller radii of contact. This is because the pure flattening models underpredict the pressure during fully plastic contact, while pure indentation models overpredict it. The predictions of the model in Ghaednia et al. [41] show the best match with the FEM results.

Figure 9 shows variations in the contact force due to varying displacement during indentation. The Kogut and Etsion model [93] shows a large difference with the FEM results, likely because the formulation provided in their model is for very small deformations compared to the deformations considered here. The Jackson and Green model [52] predicts only slightly lower values than predicted by the FEM analysis, as would be expected from a model developed for flattening contact. Kogut and Komvopoulos [80] also predicts lower values than predicted by the FEM analysis.

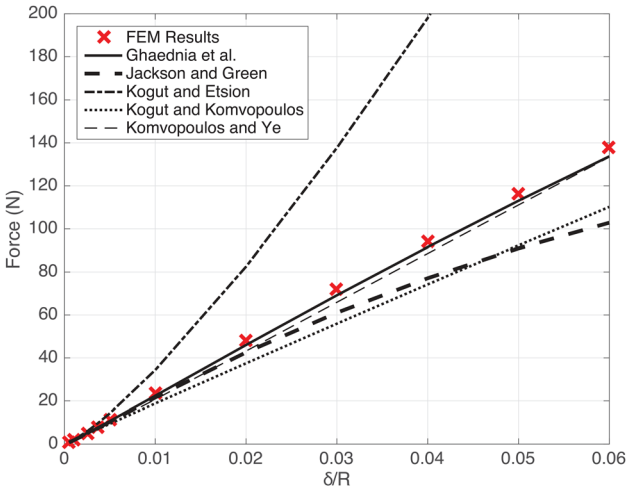

Fig. 9 Comparison between predicted contact forces during indentation for different contact models

Again, the Ghaednia et al. [41] and Ye and Komvopoulos models [11] agree most closely, which is as expected because this case can be classified as indentation.

Next, flattening is considered. In this case, the yield strength of the flat and sphere are $S_{yf} = 530$ MPa and $S_{ys} = 165$ MPa, respectively. The Young's modulus and the Poisson's ratio of the flat and sphere are $E_f = 201$ GPa, $E_s = 200$ GPa and $\nu_f = \nu_s = 0.3$, respectively. Similar to the previously considered indentation case, the deformations are mostly in the elastic–plastic regime.

Figure 10 shows the predicted changes in the contact radius due to the change in the displacement. Just as with indentation, both of the flattening models [52,93] predict larger values than predicted by the FEM analysis. In contrast, the indentation models [11,80] predict smaller values. Ghaednia et al. [41] and the Jackson and Green model [52] show better matches with the FEM results. These differences in prediction between the models are expected, since the finite element analysis used in this paper considers the deformation of both of the objects, while all the models but Ghaednia et al. do not. For example, for the flattening models, even very small deformations on the flat can decrease the contact radius significantly.

Figure 11 depicts the comparison of the predicted contact force between the models and the FEM results during flattening. As

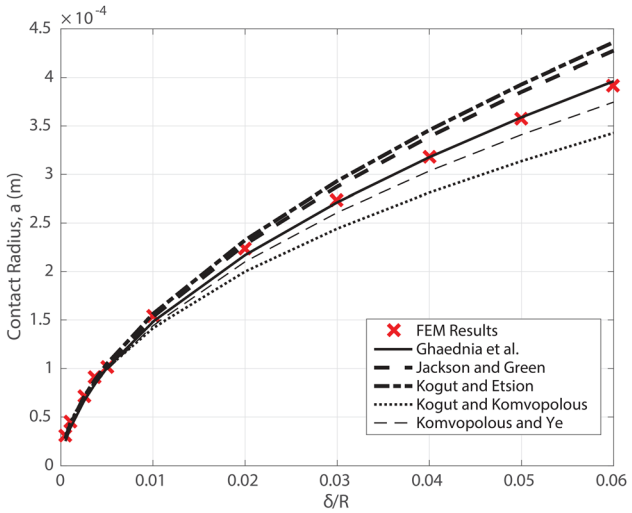

Fig. 10 Comparison between predicted contact radii during flattening for different contact models

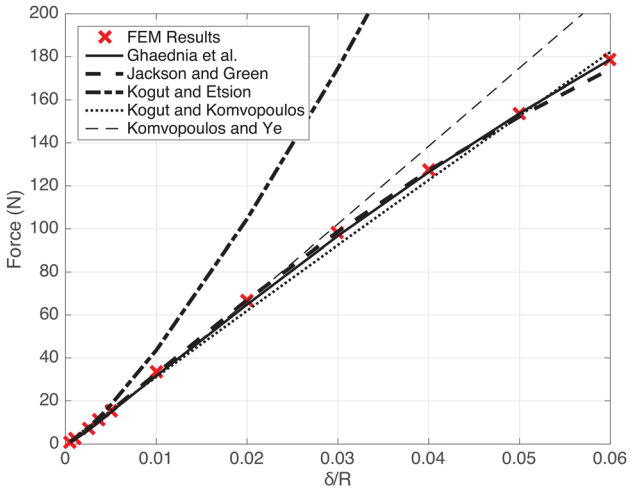

Fig. 11 Comparison between predicted contact forces during flattening for different contact models

with the indentation case, the Kogut and Etsion model shows large differences for large deformations. For this case, the models of Ghaednia et al., Jackson and Green, and Kogut and Komvopoulos all show good agreement with the FEM results. Ye and Komvopoulos also showed a good match for smaller displacements ($\delta/R \leq 0.03$).

It can be concluded from the numerical comparison that for the flattening case, the Jackson and Green [52] and Ghaednia et al. models [41] can provide better predictions for the contact force. For the indentation case, Ye and Komvopoulos [11] and Ghaednia et al. [41] show better agreement with the FEM. While the comparison here is not extensive, it has been performed for a wider range of material properties than in previous works.

3.3.5 Spherical Contact With Strain Hardening. One of the major simplifications of almost all of the studies, whether experimental, theoretical, or numerical, is neglecting the material strain hardening. Tabor used work hardened materials [66] in his tests to exclude the effect of strain hardening on the Brinell hardness test. In the aforementioned theoretical and numerical works, the material is often assumed to be elastic–perfectly plastic.

There are only a few studies that consider the effect of strain hardening, starting with Meyer's [75] hardness test, in which he formulated the relation between the average pressure and the contact radius, in the fully plastic regime and assuming a uniform pressure distribution, as

$$F_p = p_0 \pi \frac{a^n}{a_p^{n-2}} \tag{24}$$

Here, n is the Meyer hardness exponent [63,66] and is related to the strain hardening exponent, n_ϵ, by $n_\epsilon = n - 2$. It should be noted that $n = 2$ for elastic–perfectly plastic materials and $n = 3$ for elastic contact.

Another way of accounting for strain hardening in the stress–strain diagram is by using a material having bilinear isotropic properties. For bilinear materials, the tangent modulus, E_t, is defined in terms of the hardening parameter

$$\text{HP} = \frac{E_t}{E - E_t} \tag{25}$$

where HP varies from 0 to 0.5 for most practical materials. Hence, the upper limit of E_t could be one third of E. Brizmer et al. [88] analyzed the effect of a 2% tangent modulus (2% of the Young's modulus) on a sphere with bilinear material properties contacting a rigid flat. The tangent modulus was also used by Shankar and Mayuram [108] to improve the effort in Kogut and Etsion [93] to account for the strain hardening effect. Interestingly, Kogut and Etsion [93] stated in their paper that even a high amount of hardening (the tangent modulus was 10% of the Young's modulus) caused only a fairly small deviation from the elastic–perfectly plastic results. Shankar and Mayuram [108] proposed a new empirical formulation similar to the one developed by Kogut and Komvopoulos [80] for three different values of the tangent modulus: $E_t = 0.025E$, $E_t = 0.05\ E$, and $E_t = 0.1E$. They showed that the interference ratio at which the contact changes to fully plastic also changes based on the ratios S_y/E and E_t/E. Later, Sahoo et al. [109] studied the effect of the tangent modulus on the flattening case of spherical contact. They analyzed the effect of strain hardening on the contact area and contact force and discussed the difficulties and perhaps impossible task of developing a predictive formulation when hardening is important. Sahoo et al. also confirmed that small amounts of hardening ($E_t/E = 0.02$) do not influence the results significantly compared to the perfectly plastic case, but for HP = 0.1, the hardening results differ by up to 17% from the perfectly plastic case. For HP = 0.5, the load and area differ by up to 52% and 33%, respectively.

Brake [48] developed a semi-analytical formulation for the elastic–plastic indentation contact of a sphere. To account for the effect of strain hardening, Brake used Meyer's definition of the hardening exponent for the fully plastic regime of the contact. He used a reduced hardness to consider the combined plasticity of both surfaces, which is given as

$$\frac{1}{H} = \frac{1}{H_s} + \frac{1}{H_f} \tag{26}$$

This reduces the hardness, and as a result, the contact force values decrease for the fully plastic regime. Note that there appears to be no fundamental mechanics based derivation for Eq. (26) [48]. Instead, Eq. (26) is based on the similar equation for combining the elastic properties of two contacting bodies, which is derived from the theory of elasticity. However, a similar derivation is not possible for combining the plasticity properties of two contacting bodies. Brakes formulation has been verified with experimental results of indentation tests considering the effect of strain hardening.

Recently, Zhao et al. [110] considered the loading and unloading of an elastic–plastic sphere contacting a rigid flat in the

full-stick condition, while including power-law strain hardening in their finite element model. As expected, hardening decreased the contact area and increased the force at the same deflection compared to the elastic–perfectly plastic case. Zhao et al. also provided the following equations to predict the normalized contact area and force as a function of deflection that improved the empirical formulation developed by Brizmer et al. [88] by including hardening:

$$\frac{A}{A_c} = \frac{\delta}{\delta_c}\left\{1 + \exp\left(1 + \frac{1}{1 - \left[\frac{\delta}{\delta_c}\right]^q}\right)\right\}$$
$$\frac{F}{F_c} = \left(\frac{\delta}{\delta_c}\right)^{3/2}\left\{1 - \exp\left(1 + \frac{1}{1 - \left[\frac{\delta}{\delta_c}\right]^p}\right)\right\} \quad (27)$$
$$q = 0.179n^2 - 0.420n + 0.184\nu + 0.243$$
$$p = -0.159n + 0.0731\nu + 0.183$$

Here, n is the strain hardening exponent, and the critical values should be obtained for the full-stick case using Eq. (19). Additional equations were also provided for the permanent deformation of the sphere after unloading.

4 Elliptical Contact

Elliptical or ellipsoid contacts, i.e., contacts between surfaces with different principal radii or axes of curvature, have also been investigated, although not nearly as thoroughly as spherical contacts. Such elliptical contact could, for example, arise from the contact of two cylinders whose axes are not aligned. In the elastic regime, the case of elliptical contact can be analyzed using the Hertzian theory [6,15]. Horng [111] performed such analysis with a technique similar to that in the work of Chang et al. [92] on spherical contacts, which relied on a volume conservation approach for the elastic–plastic contact regime. Jeng and Wang [112] followed a similar methodology but with a template inspired by Zhao et al. [73]. Jamari and Schipper [113] also followed a similar approach, and their model was verified with the experimental data of Chaudhri et al. [81]. Lin and Lin [114] provided one of the first finite element analyses of elastic–plastic elliptical contacts and derived a phenomenological description that appears to be the most accurate formulation available for making predictions on the elastic–plastic elliptical contact. Their equations for predicted contact area, contact force, and deflection are provided in Appendix C.

5 Two-Dimensional Sinusoidal Contact

Westergaard [115] was the first to solve the case of elastic contact of a two-dimensional (2D) sinusoidal wavy surface with a flat, where the height of the surface is described as $z = \Delta(\sin(2\pi x/\lambda) + 1)$ in terms of the amplitude, Δ, and wavelength, λ. In Westergaard's work, the average pressure per length that when applied to the surfaces under plane strain conditions yields complete contact (i.e., no gaps between the surfaces) is found to equal

$$p^*_{\text{2D,elastic}} = \frac{\pi E' \Delta}{\lambda} \quad (28)$$

The contact area per unit thickness, A, is related to the average pressure, $\bar{p}$ (including the regions out of contact), by [15]

$$A = \frac{2\lambda L}{\pi}\sin^{-1}\left(\frac{\bar{p}}{p^*_{\text{2D,elastic}}}\right)^{1/2} \quad (29)$$

where L is the width of the wavy surface. Note that the contact area of the 2D wavy surface is rectangular, similar to cylindrical contact, and thus resembles a "line" contact.

Just as with cylindrical and spherical contacts, the pressure in a wavy or sinusoidal contact often results in stresses large enough to cause yielding. If the contact width is small in comparison to the wavelength, then one could simply use Eq. (1) but substitute in the relationship between the radius of curvature and the tip of a wavy profile given by

$$R = \frac{\lambda^2}{4\pi^2\Delta} \quad (30)$$

to obtain [116]

$$\delta_c = \frac{\lambda^2}{4\pi^2\Delta}\left(\frac{C_1 S_y}{E'}\right)^2\left[2\ln\left(\frac{2E'}{C_1 S_y}\right) - 1\right]$$
$$\frac{F_c}{L} = \frac{\lambda^2}{4\pi\Delta}\frac{(C_1 S_y)^2}{E'} \quad (31)$$
$$A_c = L\frac{\lambda^2}{\pi^2\Delta}\frac{C_1 S_y}{E'}$$
$$p_c = \frac{\pi C_1 S_y}{4}$$

To the best of our knowledge, Eq. (31) has not been presented previously. Gao et al. [117] provided an alternative to predicting the point of initial yield using a finite element model of elastic–plastic two-dimensional sinusoidal contact. In their work, the elastic limit is predicted by $A_c = L\lambda^2 S_y/(5E'\Delta)$. Although of the same form as Eq. (31), this differs from Eq. (31) by approximately a factor of 2. Of course, the approximations in Eq. (31) are limited to small contact areas.

Gao et al. [117] noticed some clear differences between sinusoidal and cylindrical contacts. In the former case, at heavy loads, the average pressure rose to approximately 5.8 times the yield strength and was not limited by the conventional hardness of three times the yield strength. These high pressures were required to press the surfaces together into complete contact. Krithivasan and Jackson [116] also observed this increase in pressure for three-dimensional (3D) sinusoidal surfaces (see Sec. 7) and stated that there is no upper limit to the pressure as the amplitude is increased. They deduced that the absence of such a limit was due to hydrostatic stresses dominating as complete contact is reached. Later, Sun et al. [118] also noted the same increase in pressure when using dislocation plasticity theory to describe the plastic deformation in flattened two-dimensional sinusoidal surfaces. These observations have important ramifications when considering rough surface contacts. For instance, if a self-affine fractal description of a surface is assumed, this will result in zero contact area and infinite contact stress between contacting elastic–plastic rough surfaces [119]. The experimentally observed phenomenon of asperity persistence [120] can also be explained by this mechanism.

6 Axisymmetric Sinusoidal Contact

An axisymmetric sinusoidal asperity model can be useful in describing the deformation associated with rough surface contact at the asperity level because the hemispherical asperity model, which is commonly used in the rough surface contact, is meaningless when the normal deflection is larger than the radius. An axisymmetric sinusoidal model can be captured by a 2D representation in the finite element model, while the 3D sinusoidal geometry discussed in Sec. 7 requires a 3D finite element model. Guduru [121], Guduru and Bull [122], and Waters et al. [123] investigated an axisymmetric wavy surface, but focused on elastic adhesion, with a radially propagating waviness resulting in a concentric ring structure. In contrast, the geometry first considered by Saha et al. [124] is given by

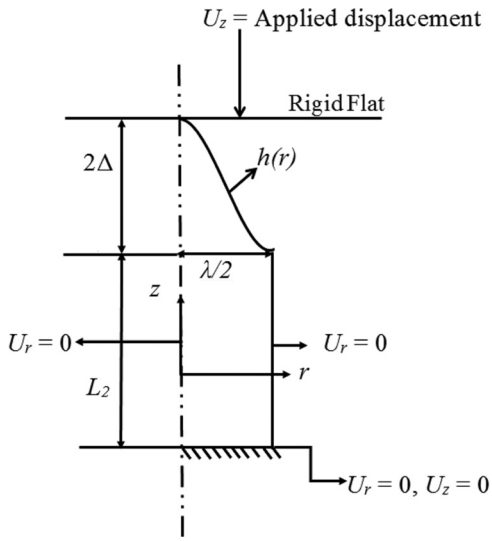

Fig. 12 Schematic of an axisymmetric sinusoidal asperity loaded with a rigid flat

$$h(r) = \Delta\left(1 + \cos\left(\frac{2\pi r}{\lambda}\right)\right), \quad r \le \frac{\lambda}{2} \tag{32}$$

and is graphically shown in Fig. 12. The elastic–plastic axisymmetric sinusoidal asperity that is described here considers interactions with adjacent asperities and also the effect of the substrate at the base of the asperity. Although the asperity contact described here may not be perfectly periodic due to the applied axisymmetric boundary conditions, it does effectively include interactions with adjacent asperities by having a confined boundary at the outer radius of the base. This is drastically different from single spherical asperity models which do not have this confinement and lateral interaction. Figure 12 shows the schematic and boundary conditions considered by this model.

The model has been developed for a broad range of material properties (yield strength in the range of $25\,\text{MPa} < S_y < 40{,}000\,\text{MPa}$, Young's modulus in the range of $50\,\text{GPa} < E < 400\,\text{GPa}$, and amplitude to wavelength ratios in the range of $0.00005 < \Delta/\lambda < 0.0125$). Bilinear hardening was also assumed by using a tangent modulus of $0.01E$. From the analysis of the finite element results, it is found that the dimensionless contact pressure depends on the dimensionless parameter, E/S_y. Figure 13 shows the effect of E/S_y (not E'/S_y) on the dimensionless contact pressure–area relation for $E = 100$ GPa and $\Delta/\lambda = 0.0125$. It is clear that as E/S_y increases, the pressure required to gain complete contact (with the entire surface in contact) increases.

The critical pressure, p^*_{ep}, at which the two surfaces reach complete contact for the elastic–plastic case is normalized by the critical pressure, p^*_e, for the elastic axisymmetric sinusoidal case [124] and plotted against $E'/S_y \cdot \Delta/\lambda$ in Fig. 14. The following equation effectively fits the collapsed curve:

$$\frac{p^*_{ep}}{p^*} = \frac{0.67}{0.653\left(\dfrac{E'\Delta}{S_y\lambda}\right)^{0.0027} + 0.22\left(\dfrac{E'\Delta}{S_y\lambda}\right)^{s}} \tag{33a}$$

$$s = 1.6\left(\frac{E'\Delta}{S_y\lambda}\right)^{-0.141} \tag{33b}$$

$$p^* = \frac{3}{4}\pi\frac{E'\Delta}{\lambda} \tag{33c}$$

This fit agrees with the curve very well and differs from it on average by 2.34% and overall by no more than 5.75%. Also note that p^*_{ep} can be much greater than conventional hardness for this geometry as well. This same phenomenon was also noted in other works considering the elastic–plastic contact of wavy surfaces [4,116,117,125,126].

From Fig. 14, it is observed that there is a cluster of points near $p^*_{ep}/p^*_e = 1$. The cases where p^*_{ep}/p^*_e equals 1 correspond to elastic contact, because the pressure required to cause complete contact for the elastic–plastic case cannot be greater than the pressure required for the elastic case. To determine the transition value, Δ_c, of the waviness amplitude, below which all cases will be elastic, an extrapolation is made of the points approaching $p^*_{ep}/p^*_e = 1$, which results in the following estimation:

$$\left(\frac{E'\Delta_c}{S_y\lambda}\right) = 0.28 \tag{34}$$

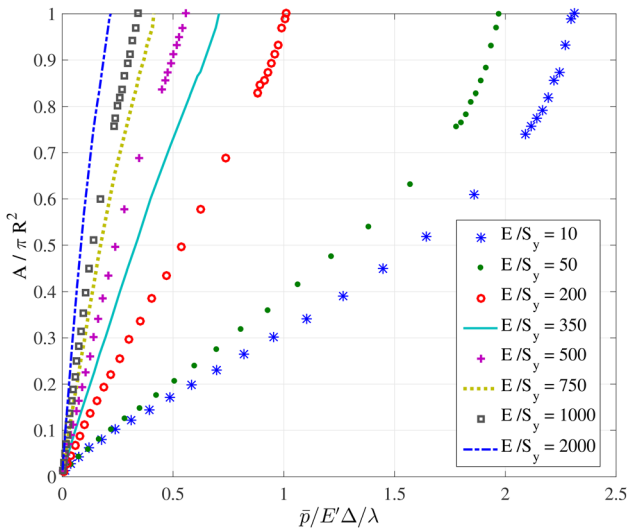

Fig. 13 Dimensionless contact pressure area relation for different values of E/S_y at $E = 100$ and $\Delta/\lambda = 0.0125$

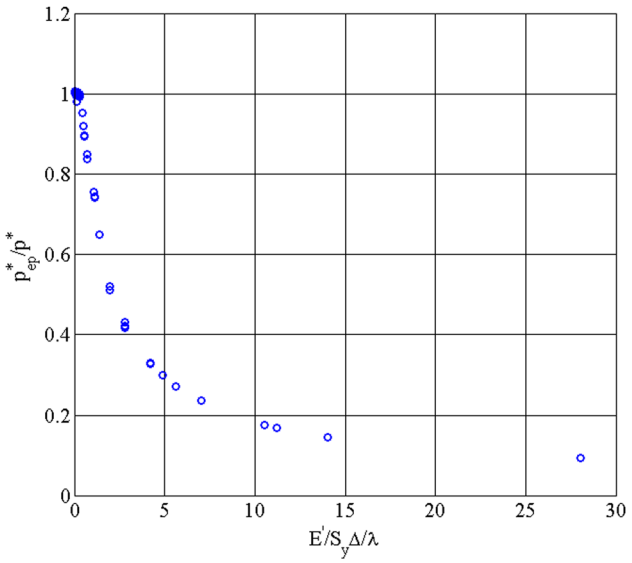

Fig. 14 Relation between p^*_{ep}/p^*_e and $E'/S_y \cdot \Delta/\lambda$ for all the cases analyzed

and, consequently

$$\Delta_c = 0.28\left(\frac{\lambda S_y}{E'}\right) \tag{35}$$

The cases that are found to be elastic using the above equation are confirmed by observing the von Mises stress predicted by the finite element analysis, which should be less than the yield strength for the elastic cases. For the elastic cases, the model proposed by Saha et al. [124] can be used to predict the contact area to pressure relation. For the elastic–plastic cases, the following equation is found by curve fitting to the finite element data:

$$\frac{A}{\pi R^2} = \frac{A}{\pi\left(\frac{\lambda}{2}\right)^2} = \frac{2}{\pi}\left(\frac{\bar{p}}{p^*_{ep}}\right)^{C'_2\left(\bar{p}/p^*_{ep}\right)}\left\{\sin^{-1}\left[\left(\frac{\bar{p}}{p^*_{ep}}\right)^{0.16}\right]\right\}^{C'_3} \tag{36}$$

$$C'_2 = 0.64 + \left[1.14 - \frac{1}{1.25}\left(\frac{E'\Delta}{S_y\lambda}\right)^{0.32}\right] \tag{37}$$

$$C'_3 = 1 + \frac{1}{200}\left(\frac{E'\Delta}{S_y\lambda}\right) \tag{38}$$

This agrees closely with the finite element predictions and differs from these on average by 3.69%.

Song et al. [127] recently examined the same case of elastic–plastic contact of a sinusoidal surface and included the effect of hardening. They also observed that the pressure was limited to three times the yield strength when no hardening is allowed (in contrast to the results presented in the previous paragraphs). In contrast, when hardening was considered, the pressure observed by Song et al. increased past $3S_y$, which is in contradiction with the results in Ref. [128]. To illustrate the possible increase in pressure with relatively little hardening, Eq. (33) is plotted in Fig. 15 as a function of $E'/S_y \cdot \Delta/\lambda$, while normalizing the pressure by the yield strength. Here, typical properties for a steel alloy were assumed ($E' = 110$ GPa and $Sy = 200$ MPa), and the amplitude over the wavelength was varied in the range of $0.00027 < \Delta/\lambda < 0.1$. Not only does the critical pressure deviate from three times the yield strength but also may far exceed this value.

Another recent paper on the topic is by Liu and Proudhon [129], which also includes the effect of strain hardening. Some of the results shown in this work appear to indicate that the average pressure does surpass the yield strength by up to a factor of 6, well past the conventional value of three. However, the authors attribute this to hardening and still state that the pressure reaches a limit of approximately three times the yield strength. They do note the decrease in the pressure with large deformations, as discussed earlier in this paper in Sec. 3.2 on spherical contact.

7 Three-Dimensional Sinusoidal Contact

The asperities of rough surfaces are typically described by spherical or parabolic geometries in most rough surface contact models. However, the geometries of actual asperities are much different than this, especially at the base of the asperities. This is especially important when an asperity is under a heavy load. Therefore, wavy or sinusoidal surface models are important for the consideration of rough surface contacts used for modeling electrical resistance, friction, and wear [116].

Johnson et al. [130] developed asymptotic solutions for the elastic contact of three-dimensional sinusoidal shaped surfaces (see Fig. 16). Here, the geometry is given by the equation

$$h = \Delta\left(1 - \cos\left(\frac{2\pi x}{\lambda}\right)\cos\left(\frac{2\pi y}{\lambda}\right)\right) \tag{39}$$

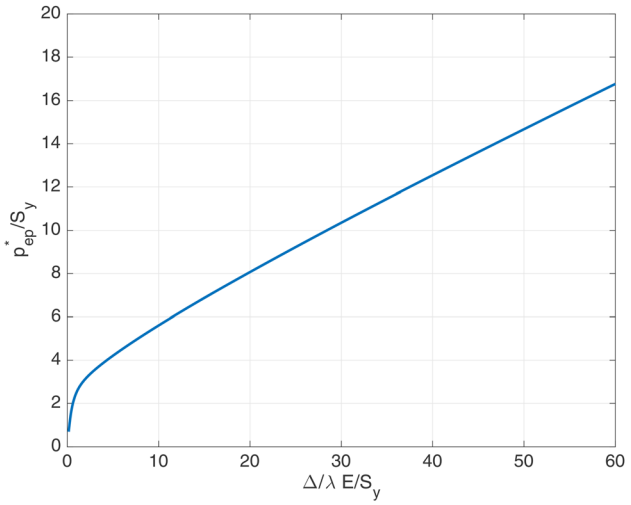

Fig. 15 Prediction of the critical pressure required to induce complete contact relative to the yield strength for an elastic–plastic axisymmetric sinusoidal asperity

In this case,

$$p^* = \sqrt{2}\pi E'\frac{\Delta}{\lambda} \tag{40}$$

Note that this p^* for the geometry defined by Eq. (39) differs from that for other geometries (Eqs. (28) and (33*c*)).

Similar to the previously considered contact geometries, as the contact force increases, the stress will increase and eventually cause yielding. If initial yielding occurs when the effective width of the contact area is small relative to the wavelength of the waviness, then the contact can still be modeled as spherical. Adapting the critical equations for spherical contact to sinusoidal contact by using Eq. (30), the critical load and area are given by

$$F_c = \frac{1}{6\pi}\left(\frac{1}{\Delta f^2 E'}\right)^2\left(\frac{C_2}{2}S_y\right)^3 \tag{41}$$

$$A_c = \frac{2}{\pi}\left(\frac{C_2 S_y}{8\Delta f^2 E'}\right)^2 \tag{42}$$

where C_2 is given in Eq. (16*b*) and $f = 1/\lambda$.

The following results build mostly on a finite element simulation of three-dimensional elastic–plastic sinusoidal contact conducted by Krithivasan and Jackson [116]. In their analysis, the range of material properties and geometries was somewhat limited ($0.00261 < S_y/E' < 0.0102$ and $0.01 < \Delta/\lambda < 0.04$). The studied range of Δ/λ was limited due to convergence difficulties of the nonlinear FEM model. The current work expands on this range.

Jackson et al. [126] used the solution of stresses for a sinusoidal pressure provided by Tripp et al. [131] to derive the critical amplitude, below which the contact in the three-dimensional sinusoidal contact will always be elastic. However, an error was recently found in Ref. [126] and is corrected in the derivation shown in Appendix B. The resulting corrected expression for the critical amplitude is given by

$$\Delta_c = \frac{\sqrt{2}S_y}{\pi E' f\left[3e^{-2(\nu+1)/3} + 2\left(\frac{1-2\nu}{1-\nu}\right)\right]} \tag{43}$$

Using Eq. (43) in lieu of the expression in Ref. [126], a new equation for the contact pressure required to cause complete

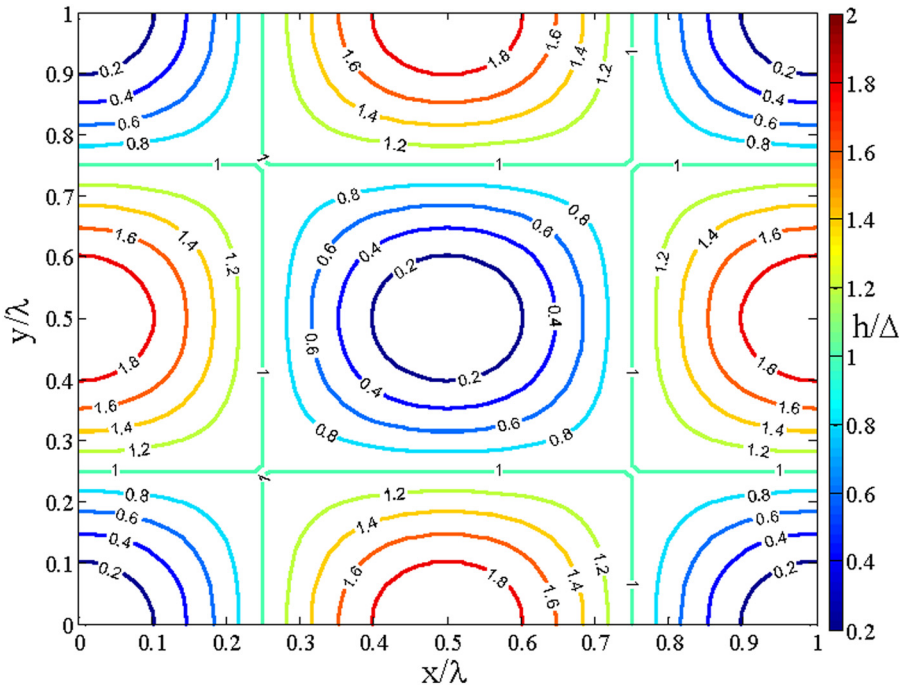

Fig. 16 Contour plot of the sinusoidal surface geometry

contact, p^*_{ep}, can then be fitted to the FEM data of Ref. [116] and additional data that were recently obtained, collectively covering an extended range of the parameters: 50 GPa $\leq E \leq$400 GPa, 0.1 GPa $\leq Sy \leq$ 2.5 GPa, $0.01 \leq \nu \leq 0.49$, and $0.001 \leq \Delta/\lambda \leq 0.05$. In particular, the phenomenological equation shown below is constructed to satisfy the constraint that $\Delta = \Delta_c$ implies $p^*_{ep} = p^*$

$$\frac{p^*_{ep}}{p^*} = 0.992\left[\left\{\left(\frac{\Delta}{\Delta_c}\right)^{\left(\frac{10}{3}\left(\frac{\Delta}{\Delta_c}\right)^{-0.39}+\frac{9}{4}\nu^4+0.64\right)}\right\}^{-1}\right] \tag{44}$$

Using Eq. (44), one can then fit additional equations to finite element results to predict the real contact area and surface separation as a function of the average pressure, as was performed in Refs. [116] and [132]. The resulting equation for predicting the real contact area, A, as a function of the average pressure is given by

$$A = A_p\left[1-\left(\frac{\bar{p}}{p^*_{ep}}\right)^{1.51}\right] + (A_{JGH})_2\left(\frac{\bar{p}}{p^*_{ep}}\right)^{1.04} \tag{45}$$

where

$$A_p = 2\left(\frac{A_c}{2}\right)^{1/(1+\mathrm{d})}\left(\frac{3\bar{p}}{4C_2S_y}\lambda^2\right)^{\mathrm{d}/(1+\mathrm{d})} \tag{46}$$

$$d = 3.8\left(\frac{E'\Delta}{S_y\lambda}\right)^{0.11} \tag{47}$$

$$(A_{JGH})_2 = \lambda^2\left(1-\frac{3}{2\pi}\left[1-\frac{\bar{p}}{p^*_{ep}}\right]\right) \tag{48}$$

Similarly, the average contact gap or distance between the surfaces, g, is given by

$$\frac{g}{\Delta} = \left(1-\left(\frac{\bar{p}}{p^*_{ep}}\right)^{A_1\frac{\bar{p}}{p^*_{ep}}+A_2}\right)^{5/2} \tag{49}$$

where

$$A_1 = -0.08\ln\left(\frac{\Delta}{\Delta_c}\right) \tag{50}$$

$$A_2 = \frac{1}{15}\left(\frac{\Delta}{\Delta_c}-1\right)^{0.44} + 0.99^{0.41\left(\frac{\Delta}{\Delta_c}-1\right)} - \frac{1}{2} \tag{51}$$

The contact of sinusoidal or wavy surfaces also shows some interesting differences when compared to spherical contact. In a spherical contact that is dominated by plastic deformation, the average pressure decreases as the load and the ratio of the contact radius to the radius of curvature increase (see Sec. 3.2). This pressure is approximately 2.84 multiplied by the yield strength for small contact areas and decreases toward a limiting value equal to the yield strength as the load is increased [72]. However, this trend does not occur in sinusoidal contacts. For the fully plastic case, Manners [4] used slip-line theory to show that as complete contact was approached, the pressure could grow beyond any bounds. This was due to the stress state becoming hydrostatic and therefore not allowing plastic deformation. In actual contacts, the surface pressure will remain bounded because elastic deformation allows for the surfaces to be pressed together. The average pressure does, however, increase relative to the yield strength and appears to have no upper limit. It increases with the amplitude of the sinusoidal surface being flattened.

8 Combined Normal and Tangential Loading

8.1 Sphere Normal and Tangential Loading, Presliding. The elastic–plastic contact of spheres under combined normal and tangential loading has been studied for a long time, beginning with the classic works of Cattaneo [133] in 1938, Mindlin in 1949

[134], and Mindlin and Deresiewicz in 1953 [135]. Interest in this area focused on deducing the underlying mechanics of friction. Mindlin used a predefined friction coefficient between two surfaces. He set an upper limit on the local shear stress, equal to the local normal stress multiplied by a predefined coefficient of friction. Known as the local Coulomb friction law, whenever the computed shear stress exceeds the upper limit, local slip takes place. Therefore, the sliding of the entire surface then occurs when all shear stresses over the contact area reach the upper limit, thereby satisfying the (global) Coulomb friction law. Mindlin also obtained the surface shear stress distribution for the full stick and partial slip conditions. Keer et al. [136] followed Mindlin's approach, obtaining the region for sliding of elastic bodies in contact. Hamilton [137] found the yield inception by using Hertz contact pressure and the Mindlin shear stress distribution. Sackfield and Hills [138] modified the stress distribution by considering the effect of the shear stress on surface displacements for two dissimilar cylinders.

Bowden and Tabor [139] presented a different approach, which considered the start of surface slip in relation to the mechanical properties rather than a local friction law as in Ref. [134]. They used a failure mechanism related to the material properties to determine the sliding inception. They suggested that the tangential load at sliding inception was equal to the real contact area times the material shear strength. Courtney-Pratt and Eisner [140] measured the contact area of a metallic sphere pressed against a smooth flat. They observed an increase in the contact area when the tangential load was increased. Tabor [141] defined this phenomenon as "junction growth," explaining that a contact area has already yielded plastically under a given preload and must grow when it is subjected to an additional tangential loading. This is because the tangential loading can reduce the mean contact pressure and require additional area to accommodate the additional shear stresses.

Chang et al. [92] treated the sliding inception as a failure mechanism based on the failure of small junctions between contact surfaces (this is the same CEB model that was discussed previously for normal elastic–plastic spherical contact). They gave an explicit formula to calculate the maximum tangential loads that a single spherical asperity can support for a given preload against a rigid flat before sliding inception. Then, the total tangential load for the rough surface contact was obtained using a statistical method. Kogut and Etsion [104] presented a semi-analytical solution for the sliding inception in both elastic and plastic cases. It was found that failure occurs either on or beneath the contact interface, depending on the normal load. Static friction is defined by the condition when the tangential force causes a continuous layer of yielded material that allows the contact to slide unrestrained. At this moment of initial slip, the tangential load is the static friction force. Using this local yielding criterion, Kogut and Etsion [104] provided an empirical expression for the single asperity static friction

$$\mu_s = \begin{cases} 0.516\left(\dfrac{F_n}{F_c}\right)^{-0.345}, & 0 < \omega/\omega_c \le 1 \\ -0.007\left(\dfrac{F_n}{F_c}\right)^{2.104} + 0.083\left(\dfrac{F_n}{F_c}\right)^{1.405} - 0.380\left(\dfrac{F_n}{F_c}\right)^{0.701} + 0.822, & 1 < \omega/\omega_c \le 6.2 \end{cases} \tag{52}$$

At approximately the same time as Kogut and Etsion, Zhang et al. [142] considered the sliding contact of a sphere against a flat surface using the finite element method. They were able to map the different regimes of elastic, elastic–plastic, and fully plastic contact with the sphere subjected to combined normal and tangential loading. They also examined the effect of the friction coefficient and tangential loading on the stress distribution, contact area, and load.

Brizmer, Kligerman, and Etsion [143] presented a new approach (referred to as the BKE model) for determining the sliding inception in the full-stick condition, known as the stiffness criterion. They assumed that the sphere starts sliding when the instantaneous tangential stiffness is equal to a small predefined value. By using this criterion, Brizmer et al. investigated several parameters such as junction stiffness, static friction force, and static friction coefficient. The evolution of the contact area (i.e., junction growth) was investigated in Ref. [144]; they found an empirical relation between the contact area and the normal preload by fitting to FEM results. The contact of a deformable sphere under combined normal and tangential loading by a rigid flat in the presliding regime was investigated by Zolotarevskiy et al. [145], who developed a model for the evolution of the static friction force and stiffness. During the process of increasing the tangential load with a normal preload, Brizmer et al. [143] found that the static friction coefficient is independent of the sphere radius and only slightly affected by the material properties. In their work, the phenomenological equation relating the static friction coefficient to the dimensionless normal force, F_n/F_c, was given by

$$\mu_s = 0.27 \coth\left(0.27\left(\frac{F_n}{F_c}\right)^{0.35}\right) \tag{53}$$

and, as a function of dimensionless interference, δ_s/δ_c, by

$$\mu_s = 0.26 \coth\left(0.27\left(\frac{\delta_s}{\delta_c}\right)^{0.46}\right) \tag{54}$$

Later, Li et al. [146] used a similar methodology as Ref. [143] to account for larger deformations on the asperity level by incorporating the effects of the Jackson and Green model [52]. Their model considered the statistical rough surface contact in the static friction model.

Other researchers used different criteria for slip on the surface. The model by Eriten et al. [147] limits the local shear stress by a critical friction shear stress. The critical friction shear stress is the local normal stress multiplied by a local Coulomb friction coefficient. Using this methodology, Patil and Eriten [148] used Coulomb friction to determine the contact interfacial strength and proposed the phenomenological equation

$$\mu_s = \min\left(\mu_{\text{local}}, \max\left(0.167, \alpha\left(\frac{F}{F_c}\right)^{\lambda}\right)\right)$$
$$\alpha = 0.0931\mu_{\text{local}}^{0.7153}, \quad \lambda = -0.223\mu_{\text{local}} + \left(-0.00002E/S_y + 0.0261\right) \tag{55}$$

where μ_{local} is the local Coulomb friction coefficient.

Wu et al. [149] proposed a frictional model based on the maximum frictional shear stress criterion for the sliding inception. They used a critical frictional shear stress rather than Coulumb's law to determine the critical shear strength. Their FEM-based model realized the friction transition from the local yield criterion of the KE model to the tangential stiffness criterion of BKE model. In Ref. [149], the shear strength ($\sigma_y/\sqrt{3}$) was set as the critical friction shear stress. Wu et al. [149] proposed the phenomenological equation

$$\mu_s = 0.3\coth\left(0.57\left(\frac{\delta_s}{\delta_c}\right)^{0.41}\right) \tag{56}$$

For all of the models listed, the dimensionless maximum tangential load can be obtained from

$$F_{t\max} = \mu_s F_n \tag{57}$$

Several experimental investigations of static friction and junction growth under combined normal and tangential loading in spherical contact have been reported in the literature. Static friction and contact area at sliding inception of a deformable sphere loaded against a rigid flat were measured by an experimental system employing load cells and displacement transducers in Ref. [150]. This work confirms that the effective static friction coefficient does indeed decrease with normal load as predicted by the theoretical results.

Later, a novel test rig, which enables real time and direct in situ measurements of static friction, contact area, and relative displacement, was developed in Ref. [100]. This rig allowed for the contact area between a sphere and a flat to be measured optically while under load. The initial results of the rig for normal loading were confirmed by Hertz theory and the Kogut and Etsion model [93]. The rig was also used to confirm the theory of unloading of elastic–plastic spherical contact [106]. Using this test rig, measurements of friction force and contact area at the instant of sliding inception were reported in Ref. [151]. In this work, several different materials and spheres of varying sizes were loaded against a hard sapphire flat. It was observed that the static friction coefficient is strongly dependent on the normal load.

To investigate the static friction occurring in tin-plated electrical connectors, measurements were also conducted on tin interfaces using an automated tilting plane apparatus [152]. The experiment measurement was of a nominally flat on flat interface. The static friction was observed to decrease with normal load. Good agreement between the measurements and the static friction model created by Li et al. [146] was obtained once the existence of the tin oxide on the surface was accounted for.

The phenomenon of junction growth, during which the contact area grows as tangential load is applied, was also confirmed experimentally using the same rig [153]. Junction growth was observed to increase the contact area by up to 45%. Based on the measurements in Ref. [151], Etsion [154] revisited the Cattaneo–Mindlin [134,155] concept of interfacial slip in tangentially loaded compliant bodies and presented an alternative approach that treats sliding inception as a failure mode involving material plastic strain. Etsion argued from recent finite element models and experiments that the original assumptions made by Cattaneo–Mindlin were nonphysical but allowed the analytical solution to be developed.

8.2 Normal and Tangential Loading of Sinusoidal Contact. This section described original results from finite element analysis of the sinusoidal geometry described by Eq. (38) rather than the typically assumed spherical geometry [156]. In these computations, normal loading is applied first with the sinusoidal surface and the flat assumed to be in full stick. Next, the tangential loading increases gradually while the normal preload remains constant. The maximum friction shear stress criterion is used to determine the sliding inception. Local sliding occurs when the frictional shear stress at one element on the contact area reaches τ_c. The sliding of the whole asperity occurs when all the elements on the contact area slide.

Figure 17 presents typical results for the instantaneous dimensionless tangential load, F_t/F_n, as a function of the dimensionless tangential displacement of the flat, u_x/ω_0, for several different combinations of material properties, geometrical parameters, normal pressure, and critical shear strength. In each case, as the tangential loading progresses, F_t/F_n increases gradually until a constant value of $F_{t\max}/F_n$ is approached, corresponding to the static friction coefficient. As shown in Fig. 17, all the model parameters have some effect on the static friction coefficient.

Figure 18 shows the isolated effects of different parameters on the static friction coefficient. It can be seen in Figs. 18(*a*)–18(*d*) that the static coefficient of friction decreases as E, ν, and Δ/λ increase and, in contrast, increases with S_y. An interesting finding is that when the geometric ratio, Δ/λ, is very small, it is very difficult to initiate sliding, and the static friction coefficient could be greater than 1, as shown in Fig. 18(*d*). This would be analogous to the high friction obtained from smooth clean surfaces in contact. For convenience, the nondimensional parameter, $\varphi = (E'/S_y)(\Delta/\lambda)$, proposed by Gao et al. [157] may be used to characterize the static coefficient of friction. From the finite element analysis, it was found that the static coefficient of friction decreases as φ increases.

Figure 18(*e*) shows the static coefficient of friction decreasing with increasing normal contact pressure. For low- and medium-strength contact pressures, the trend is the same as the spherical contact. However, under high contact pressures, the static coefficient of friction shows a different behavior. Under these pressures, the tangential load can cause complete contact for some cases, and in such a condition, the maximum shear force will not increase, no matter what the normal force is (i.e., the static friction coefficient will decrease continually).

In Ref. [149], the value of the critical shear stress τ_c was set to $S_y/\sqrt{3}$, representing the shear strength of two identical metal surfaces bonded together. However, τ_c often differs from this value as a function of temperature conditions, the presence of contaminants, and lubrication. The effect of τ_c on the static friction coefficient is shown in Fig. 18(*f*).

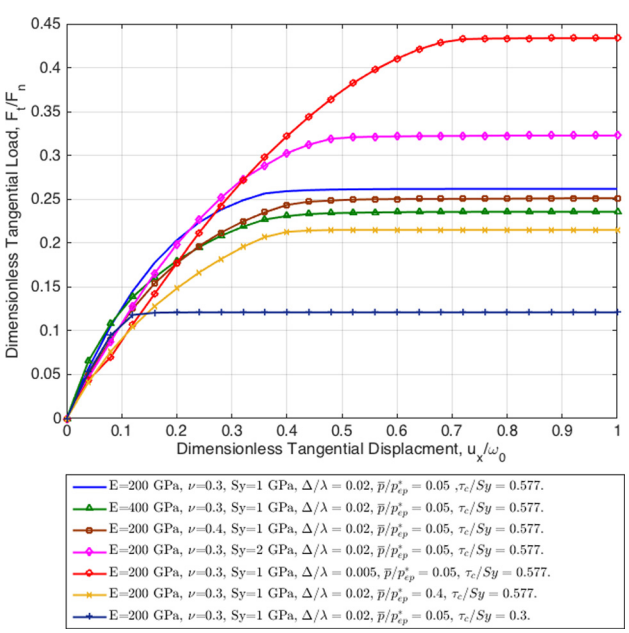

Fig. 17 The dimensionless tangential load versus the dimensionless tangential displacement for different parameters

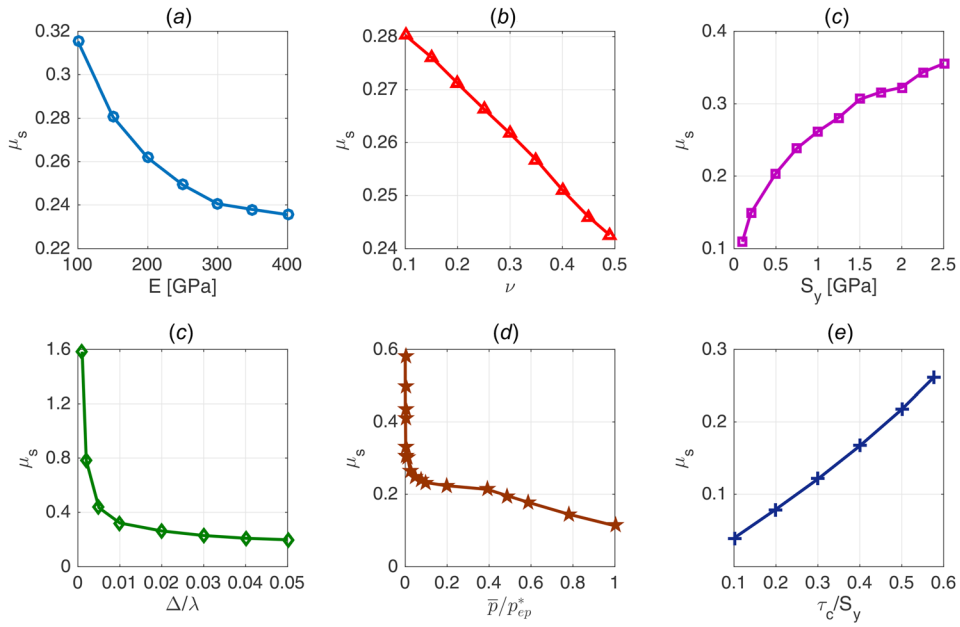

Fig. 18 The effects of different parameters on the static friction coefficient

Using the FEM data, the following phenomenological equation [156] relates the static friction coefficient to material properties, geometric parameters, the dimensionless contact pressure, and the critical shear strength:

$$\mu_s = \left[1.848\coth\left(6.5\,\varphi^{2/3}\left(\frac{\bar{p}}{p^*_{ep}}\right)^{1/3}\right) - 0.184\,\varphi^{\frac{1}{4}}\left(\frac{\bar{p}}{p^*_{ep}}\right)^{\frac{1}{8}} - 1.482\right] \times \left[\left(\frac{\tau_c}{S_y}\right)^2 + 2\frac{\tau_c}{S_y}\right] \tag{58}$$

Similar to the equations for the sliding inception of a sphere against a flat, Eq. (58) only represents the interface of a single asperity contact, not a randomly rough surface. While it cannot be considered the same as the coefficient of friction between two objects with rough surfaces, it may be considered as a qualitative friction coefficient that provides the expected trends of a rough surface contact. For example, Eq. (58) does effectively predict the static friction for a periodic sinusoidal surface with many points of contact loaded tangentially.

8.3 Sliding Contact of Spheres and Cylinders. A handful of papers have examined the sliding contact of two interacting curved surfaces. The case of a curved surface sliding against a flat surface has also been studied extensively, as noted in Sec. 8.2, but may not be representative of asperity interactions between two rough surfaces with similar magnitudes of roughness. This is because when two rough surfaces come into contact, most of the contact will occur between the asperities on both surfaces. Models of sliding of a curved surface against a flat would only be applicable to a rough surface when in contact with a much smoother surface.

For cylindrical line contact, Komvopoulos [24] studied the contact of a layered flat against a sliding rigid cylinder using FEM. One of the first papers to report using finite elements to study a sliding interaction between spheres is Faulkner and Arnell [158]. Their study neglected the recovery phase of the interaction and therefore could not be related to friction. Jackson et al. [159] later expanded the investigation to include the recovery of the surfaces after contact. This study included both a semi-analytical and finite element based approach in order to derive phenomenological equations describing the forces during the interaction. Boucly et al. [160] studied the sliding and rolling interaction of two-dimensional asperities. Vijaywargiya and Green [161] concurrently studied the sliding interaction and energy loss occurring between cylinders in contact. Mulvihill et al. [162] continued this work on the interaction of sliding spheres and cylinders, but also included the effect of adhesional shear strength at the interface. This work by Mulvihill et al. is very significant because it includes the effect of both plowing and adhesive friction. Shi et al. [163] investigated sliding interaction between hemispherical asperities and also included lateral misalignment (i.e., in the previous studies, the centers of the sphere's passed directly above each other). Finally, Zhao et al. [164] recently included the effect of strain hardening into the sliding interaction of asperities. Others have also used molecular dynamics to analyze these types of interactions at the nanoscale [165–167]. Nonetheless, this is an area that still requires a great deal of work. If scientists and engineers hope to one day predict friction at a fundamental level, it will begin with modeling elastic–plastic asperity contact. In some of the above works, there appears to be great promise as there is already agreement with some experimental observations.

9 Adhesive Contact in the Elastic–Plastic Regime

In most of the previously discussed works, there are only repulsive tractions acting between the surfaces of the asperities. However, in the actual contact of surfaces, there is also an attraction that acts on the surfaces when they are out of contact. This is due to the nature of the interaction between the atoms of the surfaces, as described by their potentials. Surfaces will be attracted to each other until they are close enough that the atoms on one surface begin to repel atoms on the opposing surface. Such adhesion will result in the contact area being larger than if only repulsive tractions are considered.

There is a large amount of research investigating the adhesion of elastically deforming surfaces, but only a relatively small amount of work investigating elastic–plastic adhesion of contacting surfaces. This may be due to the fact that adhesive contact has a significant effect only on softer materials (e.g., rubber and polymer). In contrast, elastic–plastic contact often occurs between metals which are rigid enough to effectively resist the adhesive

stress. Nonetheless, this section will provide a brief summary of research on elastic–plastic adhesive contacts.

As was the case with elastic–plastic spherical contact, probably the first work on elastic–plastic adhesive contact was performed by Chang et al. [168]. In the CEB model, a semi-analytical solution is found by expanding the Hertz elastic contact solution to assume fully plastic volume-conserving contact once plastic deformation has initiated. Adhesion was included in the model by using the well-known Derjaguin, Muller, and Toporov (DMT) model [169] for elastic contacts. The DMT model simply adds the adhesive pressures to the outside of the contact region of the spherical contact, which then effectively adjusts the contact force. The inclusion of adhesion increases the contact area relative to a model that only considers repulsion.

In 2000, Mesarovic and Johnson [170] investigated the effect of adhesion on elastic–plastic spherical contact. They included an extensive approximate derivation of the pull-off of an elastic–plastic contact by using the Maugis–Dugdale model [171] and rigid punch decomposition. By employing the finite element method, they found that the pressure distribution becomes uniform during loading, but then at the end of pull-off, returns to a parabolic distribution similar to Hertzian contact. Adhesion was included on top of the finite element model rather than explicitly in the model. Mesarovic and Johnson found that they could map the different mechanisms of pull-off by using two nondimensional parameters

$$\chi = \frac{\pi}{2\pi - 4}\frac{wE'}{p_0^2 a_0}, \quad S = \frac{\sigma_0}{p_0} \tag{59}$$

where w is the work of adhesion, σ_0 is the maximum adhesive tensile stress, p_0 is the average elastic–plastic pressure, a_0 is the elastic–plastic contact radius, and p_0 and a_0 are both approximated by the hardness (corresponding to the fully plastic contact case). Generally, as χ increases, more plasticity is expected, while S represents the transition from an unstable pull-off to a malleable one, during which the material between the surfaces yields rather than cracks ($S = 1$ is the approximate boundary between the two mechanisms).

Kogut and Etsion [172] followed in the footsteps of Chang et al. [168] by including adhesion directly in their semi-analytical solution in Eq. (20) (which was fitted to finite element results without adhesion) using the DMT model [150].

Sahoo and Banerjee [173] focused on elastic–plastic adhesive contact between rough surfaces, but also provided a methodology for including adhesion in elastic–plastic contact following the well-known Johnson, Kendall, and Roberts (JKR) model [174]. The JKR model includes the adhesive pressure within the contact area but neglects it outside of the contact area. The JKR model is considered more applicable to soft materials as opposed to the DMT model which is more applicable to harder surfaces. Sahoo and Banerjee's work showed that adhesion reduced the stiffness between the surfaces and suggested that roughness can reduce the pull-off force required to separate surfaces.

Du et al. [175] examined the adhesive contact of an elastic–plastic sphere by including an adhesive stress based on the Lennard-Jones potential in the finite element model and may have been the first to do so. This approach allowed for a clear observation of the bifurcation of the pull-off mechanism. In some cases, the pull-off was sudden and brittle, while in other cases there was a ductile failure and a neck of plastically deformed material formed between the surfaces. Du et al. also suggested that the parameter S proposed by Mesarovic and Johnson [170] could be used to predict which pull-off mechanism would occur. In a follow-up work, Du et al. [176] examined this transition and elastic–plastic spherical adhesion more closely. They found that the plasticity could be related to the applied interference relative to the critical interference. They also found that the transition from a brittle to ductile separation took place at approximately $S = 1.2$. Note that their calculations assumed that p_0 was equal to the hardness.

Later, Kadin et al. [177] performed a very similar analysis using FEM and spring elements to consider the adhesion between the surfaces. Here, again, the adhesive stress was based on the Lennard–Jones potential. Stress contours of the contacts during and after unloading were used to conclude that plastic deformation initiates just below the surface near the edge of the contact radius, as opposed to in an adhesionless contact where plastic deformation initiates just below the center of contact. The authors suggested that the yield strength should be substituted for p_0 in the expressions for S, and that the well-known Tabor parameter [178] was an important variable for characterizing elastic–plastic adhesive contact, in addition to S and the normalized deflection. High values of S and normalized deflection and low values of the Tabor parameter appeared to result in the most plastic deformation and hysteresis. Low values of the Tabor parameter appeared to cause more necking during pull-off.

10 Rough Surface Contact

This section is meant to only briefly introduce rough surface contact and ways that single asperity models are included in rough surface contact frameworks. There are many published papers in this area, and the references mentioned here are not exhaustive of the literature. If one seeks a more in-depth review of rough surface contacts, they can use one of the previous reviews on the topic [6–9,179], although these are somewhat out of date.

All surfaces are rough to some degree. The area in actual contact, labeled as the real contact area, is often much smaller than what it appears to be. It is very difficult to include this roughness in a model due to its complexity of randomness and features over multiple scales. Nonetheless, many researchers have approached this problem, and there are therefore many models that can be used to make predictions. It is very difficult to measure the real area of contact with precision to verify the models [151,180–188]; therefore, all of these models should be used with great care and caution.

After some early turmoil [189,190], in recent years researchers appear to be coming to a consensus of what a valid elastic rough surface contact model looks like and which of those in the literature meet these expectations [191–196] (except perhaps when adhesion is considered [197]). This type of progress has not yet been made with regards to elastic–plastic contact of rough surfaces. A few works have made some comparison between the various models, but it is extremely difficult to obtain a truly accurate deterministic model of elastic–plastic rough surface contact. Therefore, here the various kinds of models will be briefly introduced along with how they relate to single asperity models.

There are many possible ways to classify rough surface contact models, but the essential types are deterministic models, the hardness model, statistical models, stacked multiscale models, truncation models, and diffusion-based models. Many researchers also use fractal as a category, especially following the seminal work by Majumdar and Bhushan [198–200]. In this work, we do not consider fractals to be a category, because fractals actually characterize the multiscale nature of the surfaces and not the contact mechanics methodology used. Surfaces are now generally accepted to have features of roughness on many scales, and can, in some cases, exhibit a fractal structure. Many subsequent works [86,201–215] have employed fractals to characterize rough surfaces, typically using one the aforementioned models to handle the contact mechanics. Notably, natural surfaces may be rough but still not adhere strictly to a fractal description [216–219] or may be difficult to effectively characterize experimentally due to instrument limitations [220].

Each of the methodologies listed earlier for rough surface contact is summarized later and some representative works are discussed.

10.1 Deterministic Models. Deterministic models make very few assumptions about the surface geometry and are aimed at

solving the "complete" problem. Liu et al. [179] provide an in-depth summary of some of the various methods used to solve deterministic rough surface contact problems. There have been a few attempts at using finite element analysis to describe elastic–plastic rough surface contacts, but a consensus and thorough comparison to the existing theories has not yet been achieved. For example, when implementing deterministic models that require a mesh, it may be difficult to obtain adequate mesh density to reach mesh convergence and a reliable solution.

Liu et al. [26] used the FEM with plastic deformation and the simplex algorithm to consider cylindrical and 2D rough surface contact in plane strain. Somewhat different from other works, Jacq et al. [221] and Sainsot et al. [222] used a semi-analytical approach to solve the elastic–plastic problem. Their method relied on a modified boundary element method to account for plasticity and is more efficient than finite element models. It should be noted that this semi-analytical approach may be limited to cases where the plastic deformation is localized and not severe. Similarly, Wang et al. [223] performed a deterministic elastic–plastic rough surface analysis based on a semi-analytical approach that used the conjugate gradient method and the fast-Fourier transform. They validated their results using commercial finite element software. A similar work solved the coupled elastic–plastic contact and frictional heating thermal problem using a fast-Fourier transform solution methodology [224].

Pei et al. [211] used finite elements to investigate the elastic–plastic contact of self-affine fractal surfaces. They also provided fitted relationships for pressure and contact area as a function of surface and material properties. Liu et al. [225] also used finite elements to consider the elastic–plastic contact of rough surfaces in a microelectromechanical system. Sahoo and Ghosh [226] examined the deterministic contact of elastic–plastic fractal surfaces and made some comparisons to experimental measurements with mixed results. Thompson and Thompson [227,228] discussed the methodologies used to construct and implement rough surface contact finite element models with the aim of predicting thermal contact resistance. Specifically, they showed how to effectively incorporate real rough surfaces into a finite element mesh. Wang et al. [229] attempted to accelerate the elastic–plastic deterministic solution time by using a multilevel approach [230]. Megalingam and Mayuram [231] constructed a finite element based deterministic model of rough surface contact and made some comparisons to a hybrid statistical/deterministic model. In the hybrid model, they used the real surface geometry but considered individual asperity contacts as described by elastic–plastic spherical contact models.

10.2 Hardness Model. The so-called hardness model is one of the first and most basic rough surface contact models. Here, the contact area is predicted by dividing the applied load by the hardness, assumed to equal three times the yield strength. Based on the repeated discussions in this review of how pressure during fully plastic contact varies widely from this conventional hardness, one might conclude that this model has become antiquated. However, it can provide a quick order of magnitude estimate of the contact area between rough metallic surfaces. This model most likely was originally developed by Bowden and Tabor [139], but its provenance is uncertain.

10.3 Statistical Models. The most recognized model for rough surface contact is the statistical model created by Greenwood and Williamson [232], although there is also a belief that another research group formulated a similar model [233]. The model assumes that the asperity heights follow a statistical distribution given by $\phi(x)$. Although Greenwood and Williamson originally assumed a Gaussian distribution, others have employed other distributions [234,235]. Using this distribution, the contact area, A, can be computed in terms of the average surface separation, d, according to

$$A(d) = \eta A_n \int_d^\infty \bar{A}(z-d)\phi(z)dz \tag{60}$$

where η is the asperity density, A_n is the nominal or apparent area of contact, and $\bar{A}(z-d)$ is the contact area asperity model evaluated at the deflection of each asperity, $z-d$. Similarly, the total contact force, P, is given by

$$P(d) = \eta A_n \int_d^\infty \bar{P}(z-d)\phi(z)dz \tag{61}$$

where $\bar{P}(z-d)$ is the contact force asperity model. For $\bar{A}(z-d)$ and $\bar{P}(z-d)$, many of the elastic–plastic asperity models discussed in Secs. 3, 4, 6, and 7 of this review can be used. Note that an analytical solution of the original elastic and Gaussian version of the Greenwood and Williamson model is available in Ref. [191].

Although Greenwood and Williamson did not include an elastic–plastic model, many subsequent works have done this successfully [3,92,96,111,112,236–239]. It does appear that the roughness of the surface tends to average or reduce the influence of the chosen single asperity model (there is sometimes not much variation between rough surface contact models that employ different asperity models). Nonetheless, the accuracy of the chosen elastic–plastic asperity model is important and influences the resulting effectiveness of the rough surface contact model [240]. Although the statistical family of models is the most widely known and used, they are often criticized for considering the asperities to be all the same size and radius of curvature. Indeed, in its original form, it did not consider the multiscale nature of surfaces [241,242]. In addition, most statistical works employ spherical asperity models, which also results in the asperities being effectively isolated and unable to interact with adjacent asperities. However, refinements to the model have been proposed, and it is still considered a very useful model [202,243,244]. For example, the omission of adjacent asperity interaction might be corrected by using a wavy asperity model or a corrected asperity interaction model [245]. Shoulder to shoulder asperity contact when the asperities are misaligned could also be an important mechanism to consider [237,238]. Recently, Beheshti and Khonsari [101,102] considered the effect of an underlying curvature of a larger scale feature, such as a cylinder, on the elastic–plastic contact using a statistical model. Since they consider multiple scales of features, their analysis leads to the next type of models which inherently consider multiple feature scales.

10.4 Stacked Multiscale Models. One of the first rough surface contact models created before the statistical family of models is the stacked multiscale model of Archard [246]. This used the concept of stacking smaller and smaller asperities in order to capture the multiscale nature of surface roughness. The elastic–plastic multiscale model derived by Jackson and Streator [247] uses the same line of thought as Archard [246], but provides a method that can be easily applied to real surfaces. Purely elastic versions of the model which use a fractal description of the roughness have also been proposed [203,204]. Each scale or layer of asperities is stacked upon the previous layer, with larger scales being at the base and smaller scales on top. This results in each scale of asperities carrying the same load. Following this, the area of contact is then calculated iteratively using the factorial equation:

$$A_r = \left(\prod_{i=1}^{i_{\max}} \bar{A}_i \eta_i\right) A_n \tag{62}$$

where A_r is the real area of contact, $\bar{A}$ is the contact area of a single asperity on a certain scale of roughness, η is the real asperity

density, A_n is the nominal contact area, and the subscript i denotes a specific asperity scale level, with $i_{\max}$ denoting the smallest scale level considered. Since each scale bears the same load, $\bar{F}_i$, the single asperity load at the ith scale can be related to the total load by $F = \bar{F}_i \eta_i A_{i-1} F = \bar{F}_i \eta_i A_{i-1}$. This assumes that load is distributed uniformly across all of the asperities at a given scale, which may be a valid assumption for elastic–plastic contacts since the pressure distribution is often uniform. The spherical and sinusoidal elastic–plastic asperity contact models discussed in Secs. 3, 4, 6, and 7 can easily be employed in the multiscale model, as has been done in several previous works [119,185,247–251]. Gao and Bower [157] included elastic–plastic deformation in a similar multiscale model while assuming a Weierstrass fractal description of the surfaces. Goedecke et al. [205,206] later incorporated a fractal description of the surfaces into the multiscale model along with elastic–plastic deformation and creep, with the aim of predicting dynamic friction.

Simplified closed-form approximations of the elastic–plastic multiscale model have been derived in Ref. [208]. These approximations assume that the real contact pressure is equal to the maximum complete contact pressure of the surface. The idea is that for any of the surfaces to be in contact, the stiffest asperities in that area must be flattened. This is found from the maximum amplitude to wavelength ratio associated with the spectrum of the surface and using the pressure predicted by Eq. (44). The result is

$$\mathrm{A_r} = \frac{F}{\left(p^*_{ep}\right)_{\Delta/\lambda_{\max}}} = \frac{F}{\sqrt{2}\pi E' \left(\frac{\Delta}{\lambda}\right)_{\max} \cdot 0.992 \left[\left\{\left(\frac{\Delta_{\max}}{\Delta_c}\right)\left(\frac{10}{3}\left(\frac{\Delta_{\max}}{\Delta_c}\right)^{-0.39} + \frac{9}{4}\nu^4 + 0.64\right)\right\}^{-1}\right]} \tag{63}$$

with Δ_c as given by Eq. (43). Here, $\Delta_{\max}$ is the amplitude from the maximum amplitude to wavelength ratio and not the maximum amplitude of the entire surface spectrum. The fast-Fourier transform method is usually employed to obtain the spectrum for a surface. This method (Eq. (63)) has shown to be effective when compared to finite element results [252] and experimental measurements [185].

10.5 Truncation Models. One of the earliest models to employ a fractal description to describe rough surfaces also used a simple truncation of the rough surface geometry to determine the contact area [198–200]. In fact, many refer to this truncation model as a fractal model, but it is categorized differently here because other families of models can also employ fractals. The model determines the load on each contact patch using either elastic Hertz contact or, in the elastic–plastic regime, by assuming the pressure to equal the conventional hardness. Contrary to intuition, this resulted in the contact becoming more elastic as the size of the contact patches grew, because they have a larger radius of curvature. Although this model did advance the field at the time, it has been severely criticized for this counterintuitive behavior [253]. Nonetheless, the model did show reasonable agreement with some experimental measurements.

Later, Chung and Lin [254] modified this fractal truncation model to include the elliptical shape of the asperity contacts. They also made impressive comparisons to experimental measurements and other elastic–plastic models. In most cases, all of the data appeared to be in agreement.

10.6 Diffusion Models. Since surfaces are now considered to be multiscale in nature and perhaps fractal, they can contain many scales or layers of asperities. Since in real surfaces, these scales should possess a continuous rather than discrete spectrum, Persson [255] uses a diffusion theory to model rough surface contact. The general concept is that the pressure diffuses through the different scales of asperities. Persson's diffusion model has been shown to be very effective for elastic rough surface contact [255,256], but has not been thoroughly evaluated for elastic–plastic contact. Persson also appears to account for plasticity in a very simplistic way that is similar to the hardness model. The pressure appears to be simply truncated at the strength of the surface material.

There have been other attempts at comparing and verifying the accuracy of these various models, in addition to those discussed earlier. A comparison between various statistical models that incorporate several different spherical contact formulations was made by Jackson and Green [96]. Additionally, a comparison between fractal and statistical models was made by Kogut and Jackson [242]. This area clearly requires much more attention.

For any rough surface contact, it can be useful to determine if the contact is dominated by elastic (recoverable) or plastic (permanent) deformation. The plasticity index is often used to quantify this. The first such technique for characterizing the amount of plastic deformation was given by Greenwood and Williamson [232] and formalized as the plasticity index. The plasticity index is calculated from the surface properties and the critical interference, ω_c [236]

$$\psi = \sqrt{\frac{\sigma_s}{\omega_c}} \tag{64}$$

where σ_s is the RMS roughness of the surface asperities. To include the effect of dissimilar material properties, Green [22] stated that $C_2 S_y = \min\left(C_2(\nu_1) S_{y1}, C_2(\nu_2) S_{y2}\right)$. Yielding will occur first in the surface with the smaller $C_2 S_y$ value. Note that this technique can also be used when considering single asperity contacts (such as in Eqs. (1), (2), and (41–43)), Eq. (64) can be expanded by substituting from Eq. (16) to obtain

$$\psi = \frac{2E'}{\pi C_2 S_y}\sqrt{\frac{\sigma_s}{R}} \tag{65}$$

For typical engineering surfaces, plasticity indices range from $\psi = 0.1$ to $\psi = 100$. One shortcoming of this technique is that the roughness, σ_s, depends on the scale of the measured surface data and, therefore, the plasticity index is also dependent on scale [242]. To overcome this, Jackson and Green [191] proposed an alternative formulation based on the multiscale rough surface contact method:

$$\psi = \frac{B_{\max}}{B_c} \tag{66}$$

where $B_{\max}$ is the maximum amplitude to wavelength ratio found from a fast-Fourier transform of a multiscale surface, and B_c is the critical ratio between the amplitude and wavelength (corrected using Eq. (43)

$$B_c = \frac{\sqrt{2}S_y}{\pi E' \left[3e^{2/3(\nu+1)} + 2\left(\frac{1-2\nu}{1-\nu}\right)\right]} \tag{67}$$

Equations (65) and (66) have very similar forms even though they are derived from different methods for considering the roughness of the surface. As with the original plasticity index, higher values of ψ_m suggest that a surface is dominated by plastic deformation. When using Eq. (66), there is a clear transition to the elastic regime at $\psi_m = 1$.

Other works use slightly different variations of the surface geometry parameters when making a prediction of the plasticity index [236,243,257].

11 Scale-Dependent Properties

In some cases, it is important to consider the scale of contact when considering what material properties to include in a model. As a contact decreases below the microscale, the relevant materials properties, such as elastic modulus and yield strength, can change significantly from the bulk properties. The largest and most influential change usually occurs with the yield strength. Generally, with decreases in scale, the yield strength increases well past its bulk value until it reaches a theoretical limit of approximately a tenth of the elastic modulus [258]. For instance, the experimental results of Greer and Nix [259] showed how the yield strength of different diameter pillars in compression effectively changed with their diameter. Burek performed a similar study for tin [260].

The properties change with scale because certain features, such as grains and dislocations usually occur at a specific scale or become less influential at smaller scales. Nix and Gao [261] used a strain-gradient model to propose the following simple equation that can be used relatively easily to predict the change in yield strength with scale (here yield strength is substituted where the original work used hardness):

$$\mathrm{S_y} = (S_y)_{\mathrm{bulk}} \sqrt{1 + \frac{h^*}{h_p}} \tag{68}$$

Here, $(S_y)_{\mathrm{bulk}}$ is the bulk yield strength of the material, h^* is a characteristic length scale for the material, and h_p is the depth of plastic indentation. To employ strain-gradient plasticity in an asperity model, one needs to iteratively solve one of the elastic–plastic asperity models considered in this review while coupling it to Eq. (68) by the yield strength and plastic indentation depth. Additional information about scale effects and nanomechanics can be also found in a book by Bhushan [262].

Early research to consider scale-dependent properties in contact mechanics is found in Polonsky and Keer [263,264]. The authors modeled plastic deformation by considering matrix dislocation nucleation and motion, and so their model was inherently scale dependent. A later study by Bhushan and Nosonovsky [265] was likely the first to employ the strain-gradient method in surface interactions. They used a scale-dependent yield strength model based on strain-gradient plasticity and considered how this can affect contact and slip at small scales. Jackson [266] followed this by considering scale-dependent strength in an elastic–plastic statistical rough surface contact model. The scale-dependent strength tends to increase with smaller scales, and this work showed that the contact area, consequently, decreases when scale-dependent strength is included [266].

Almeida et al. [267,268] considered how scale-dependent properties could be important in the contact of microswitches in microelectromechanical systems. Their work used a stacked multiscale model rather than the statistical framework to consider rough surface contact and electrical contact resistance. Similarly, Adams et al. [269] considered how the friction force changes with the scale of the asperity contact area using a friction dislocation theory proposed by Hurtado and Kim [270,271] and also accounted for the effect of adhesion. A multiscale rough surface contact model was later formulated to predict the thermal contact resistance between surfaces while considering scale-dependent strength [185,272]. Jackson et al. [273] used a similar methodology to consider the multiscale rough surface electrical contact resistance. There, the scale dependence of both the strength and electrical resistivity was considered. The work suggested that not all rough surface contacts would be influenced by the scale-dependent properties.

As an alternative to considering scale-dependent plasticity as a result of scale-dependent yield strength, others have used FEMs structured into individual crystalline grains in the material. This type of model should inherently account for the size effect of the grain boundaries. Therefore, each grain is modeled as a set of elements with a different set of anisotropic material properties which correspond to their crystal orientation, Most of the research using this technique aims to analyze fretting fatigue. For example, Goh et al. [274] considered a rigid cylinder loaded normally and tangentially into a polycrystalline elastic–plastic flat surface. The grains were randomly oriented, about 1/200 the size of the cylinder radius, and consisted of 100 elements on average. The model made predictions of elastic shakedown after repeated load cycles and the onset of ratchetting and fretting.

Researchers have also used single crystalline structures with dislocations to consider the scale-dependent behavior of surface contact. Nicola et al. [275] considered a simplified rendering of a rough surface contact that was a periodic set of evenly spaced flat punches. They found that friction had a negligible effect on the results, and that there was a scale-dependent effect when the contacts were on the scale of microns (which is similar to strain-gradient theory). This scale effect was observed by comparing conventional plasticity predictions to the discrete dislocation predictions and predicts that the strength of the material effectively increased for small-scale contacts.

Sun et al. [276] used a similar discrete dislocation methodology to consider the flattening of a sinusoidal metallic surface. They also observed a size dependence, and that the pressure required to flatten the surface could nearly reach the theoretical limit of strength (approximately 1/10th of the elastic modulus). This was observed while decreasing the wavelength and holding the amplitude of the features constant, which also effectively increases the amplitude to wavelength aspect ratio of the asperity. Krithivasan and Jackson [116], Gao et al. [117], and Saha and Jackson [128] also noticed that the required pressure increased with this aspect ratio without the inclusion of any scale effects (as noted in Sec. 5). In addition to the scale effects, such an increase could therefore also be partially attributed to the effect noted by Krithivasan and Jackson [116] and Manners [4], where to reach complete contact (flattening) the stress becomes hydrostatic due to the periodic boundaries and plasticity reduction. Later, Sun et al. [118] also noted that the increase was due to the dislocation plasticity being limited by periodicity (i.e., the regular spacing between adjacent asperities). This might be understood as the same mechanism as described in Ref. [116] using von Mises plasticity, which theorizes that plastic deformation is only caused by deviatoric stresses. Hence, the observed increase in the pressure could be obtained with a combination of these effects. These effects also explain the observed phenomenon of asperity persistence from the 1970s [120] (where experiments on complete contact required pressures much higher than expected).

Very recently, Ng Wei Siang and Nicola [277] investigated contact between a 2D wavy surface against a flat, in which the surfaces were again rendered as single crystal structures (referred to as a discrete dislocation plasticity analysis). Therefore, their analysis is an effective model only of a very small-scale contact. Ng Wei Siang and Nicola also investigated the differences between flattening and indentation as discussed previously in Sec. 3. They suggested that under certain conditions, the contact of two

elastic–plastically deforming surfaces can be reduced to a case of a deformable surface against a rigid surface, but that this reduction should be performed with great care. They also noted some scale effects in the plastic deformation, but these diminished as the load was increased.

If one is considering the contact of nanoparticles, the scale-dependent strength becomes very important. Nanoparticles have been shown by experiments to possess an elevated strength [278–280] due to dislocations easily traveling to the surface, rendering a strong crystalline lattice in the particle. Many nanoparticles are spherical in shape, and so an elastic–plastic spherical model might be used in unison with scale-dependent properties to consider nanoparticle contact. Ghaednia and Jackson [50] applied such a model to the contact between nanoparticles dispersed between rough surfaces. They theorized that the particles are strong enough to increase the separation between the surfaces and therefore decrease the real area of contact which can decrease the friction.

12 Conclusion

This work provides a broad overview of the current state-of-the-art in modeling elastic–plastic asperity contact. Of course, this is a continuously growing area, and the current work is not exhaustive. For instance, it did not discuss in detail the interaction of coated (i.e., layered) surfaces [13–15] or time-dependent creep and relaxation [125,281–284]. Nonetheless, it is clear that elastic–plastic interactions are critically important for many engineering applications and not only for rough surface contacts. Due to the small size of typical surface contacts, it is very likely that plastic deformation will occur, especially in metallic contacts. Since most surfaces are now considered to be rough over many scales, similar to a fractal, it is not always obvious how to implement elastic–plastic models since the theory of elastic superposition no longer applies. Although many current models do exist [50,102,236], experimental testing of these models is one of the most important areas of future research.

This review highlighted the observation that the pressure during plastic contact is not strictly governed by the conventional hardness. Indeed, many works show that the average pressure can range from approximately the yield strength to an order of magnitude or more past it.

Another section examined the case where both surfaces are able to deform elastic–plastically, which differs from most previous analyses that only consider the deformation of either the asperity (flattening) or the flat (indentation). Interesting phenomena not captured by other models occur when the strengths of both materials are similar.

The derivation of the critical amplitude to allow plastic deformation of a sinusoidal contact was also corrected, and the critical values at which initial plastic deformation occurs in two-dimensional sinusoidal contacts were presented for perhaps the first time. However, it appears that the correction does not result in a drastic change in the results, and previous models of elastic–plastic sinusoidal contact are still very accurate.

Additionally, tangentially loaded contacts were summarized for spherical contacts and sinusoidal contacts. The offspring of these models may one day allow engineers to predict the friction based on the fundamental mechanics occurring between the surfaces.

Representative work in elastic–plastic adhesive contacts was given an overview. The work in this area has evolved from semi-analytical approximations to a more deterministic approach that incorporates adhesion in the elastic–plastic finite element models. Researchers have observed that there are different mechanisms of pull-off that depend on the stability and ductility. In the authors' opinion, this area of elastic–plastic adhesion requires the most focus and work in the future.

In another section, the concept of rough surface contact was introduced along with the various available models. This section is meant mostly as an introduction to the subject and to give an idea of how the individual asperity models can be used in a rough surface contact. The plasticity index was also reviewed as a way to qualitatively determine how much plastic deformation will occur in a rough surface contact.

Finally, Sec. 11 reviewed the subject of scale-dependent properties, and specifically scale-dependent yield strength. This is especially important in rough surface contacts where the small-scale asperities can possess strength much higher than bulk values. This will effectively reduce the area of contact between surfaces. Still, for some surfaces, the effect does not appear to be that important.

The modeling of elastic–plastic contact is clearly still a growing area that will continue to be a critical component of research. If the ultimate goal of tribologists is to predict friction, elastic–plastic contact mechanics will play a critical part in it. There are several areas that could benefit greatly from future research, for example, sliding elastic–plastic asperity contact, including adhesion in elastic–plastic contacts, as well as the inclusion of strain hardening in contact models. In addition, the analysis of scale-dependent properties is an area that is very important for rough surface contact, but that has received little attention.

Acknowledgment

Any opinions, findings, and conclusions or recommendations expressed in this material are those of the author(s) and do not necessarily reflect the views of the National Science Foundation.

Funding Data

- Division of Civil, Mechanical and Manufacturing Innovation, National Science Foundation (Grant No. 1362126).

Appendix A

In this section, we review the formulation developed by Ghaednia et al. [41] for the single asperity elastic–plastic contact of a deformable sphere with a deformable flat. The formulation is divided into five steps: finding deformations on each object, updating the radius of curvature, calculating the contact radius, calculating the hardness, and finding the contact force. The displacement of the center of the sphere is $\Delta = \delta_s + \delta_f$, where δ_s and δ_f denote the deformations of the sphere and the flat, respectively. These parameters are normalized as $\Delta' = \Delta/R$, $\delta_s^* = \delta_s/\Delta$, and $\delta_f^* = 1 - \delta_s^*$. Using the Ghaednia et al. formulation, the deformation ratio of the sphere, δ_s^*, may be expressed in terms of the normalized displacement, Δ', and the yield strength ratio, S_y^*, as shown here

For $S_y^* \leq 1$

$$\delta_s^* = 1.115(\Delta')^{0.0528}\sin\left[5.592(\Delta')^{1.37} + \frac{\pi}{2.37}\right] \times \sin\left[0.625\left(S_y^*\right)^2 + \frac{\pi}{2.16}\right] \tag{A1}$$

For $1 < S_y^* \leq 1.53$

$$\delta_s^* = -22.49\left(\frac{E'}{S_{y\min}}\right)^{-0.7}\sin\left[45.63(\Delta')^{1.75} + 0.094\pi\left(S_y^*\right)^{4.01}\right] \times \sin\left[1.546\left(S_y^*\right)^{-9.22} + 1.035\right] \tag{A2}$$

and for $1.53 < S_y^*$

$$\delta_s^* = 0.852\left(\frac{E'}{S_{y\min}}\right)^{-0.7}(\Delta')^{-0.41}S_y^*0.031 \times \tan^{-1}\left[0.142\ln\left(S_y^*\right)^{1.06\Delta'} + 3.22\right]e^{C_\delta} \quad \text{(A3)}$$

where $C_\delta = 2.307(\Delta')^{0.46S_y^*} - 0.7$.

Ghaednia et al. also related the change in radius of curvature in the contact to the deformations according to

$$\frac{R'}{R} = 1 + \delta_{s|f}^* - \Delta'\delta_{s|f}^* \quad \text{(A4)}$$

The contact radius has been divided into phases and subphases based on S_y^* and $\delta_n = \delta_s/\delta_c$, respectively, where δ_c is found from Eq. (16).

For $S_y^* \le 1.07$

$$\delta_n = \frac{\delta_s}{\delta_c}, \quad \frac{R'}{R} = 1 + \delta_f^* - \Delta'\delta_f^* \quad \text{(A5)}$$

$$a = \sqrt{R'\delta_s}, \quad \delta_n \le 3.7 \quad \text{(A6)}$$

$$a = R'\left(\frac{\pi CS_{ys}}{2E'}\right)\left[\delta_n\left(\frac{\delta_n}{1.9}\right)^B\right]\chi_{11}, \quad 3.7 \le \delta_n \le 408 \quad \text{(A7)}$$

$$a = R'\left(\frac{\pi CS_{ys}}{2E'}\right)\left[\delta_n\left(\frac{\delta_n}{1.9}\right)^B\right]\chi_{12}, \quad 408 \le \delta_n \quad \text{(A8)}$$

where $B = 0.14e^{23S_{ys}/E'}$, and

$$\chi_{11} = 0.4 + 0.55\delta_n^{0.022} + 0.283\delta_n^{-0.5}S_y^{*6} \quad \text{(A9)}$$

$$\chi_{12} = 1 + 0.024 - 0.004(\delta_n - 408)^{0.3814} + \left[0.013 + 2.2\times10^{-5}(\delta_n - 408)\right]S_y^{*6} \quad \text{(A10)}$$

For $S_y^* > 1.07$

$$\delta_n = \frac{\delta_f}{\delta_c}, \quad \frac{R'}{R} = 1 + \delta_s^* - \Delta'\delta_s^* \quad \text{(A11)}$$

$$a = \sqrt{R'\delta_f}, \quad \delta_n \le 3.7 \quad \text{(A12)}$$

$$a = R'\left(\frac{\pi CS_{ys}}{2E'}\right)\left[\delta_n\left(\frac{\delta_n}{1.9}\right)^B\right]\chi_{21}, \quad 3.7 \le \delta_n \le 408 \quad \text{(A13)}$$

$$a = R'\left(\frac{\pi CS_{ys}}{2E'}\right)\left[\delta_n\left(\frac{\delta_n}{1.9}\right)^B\right]\chi_{22}, \quad 408 \le \delta_n \quad \text{(A14)}$$

where

$$\chi_{21} = 0.4 + 0.55\delta_n^{0.022} + 0.283\delta_n^{-0.5}S_y^*C_{\chi_{21}} \quad \text{(A15)}$$

$$\chi_{22} = 1 + 0.024 - 0.004(\delta_n - 408)^{0.3814} + \left[0.013 + 2.2\times10^{-5}(\delta_n - 408)\right]S_y^*C_{\chi_{22}} \quad \text{(A16)}$$

and

$$C_{\chi_{21}} = -0.091e^{-0.008\delta_n} \quad \text{(A17)}$$

$$C_{\chi_{22}} = -0.0091[\log(\delta_n - 408)]^{3.53} \quad \text{(A18)}$$

In Ghaednia et al., the average normal pressure (hardness for the fully plastic regime) has a transition from the flattening to the indentation phase. For each phase, the hardness is a function of a/R and has been formulated as

$$\bar{p} = \frac{\bar{p}_i - \bar{p}_f}{\pi}\left[\tan^{-1}\left(300\log[S_y^* - 0.06]\right) + \frac{\pi}{2}\right] + H_f \quad \text{(A19)}$$

where $\bar{p}_i$ and $\bar{p}_f$ are the indentation and flattening hardness, given in Eqs. (10) and (8*b*), respectively. Finally, the contact force has been formulated as

$$F = W_eF_{es} + W_pF_p, \quad S_y^* \le 1.07 \quad \text{(A20)}$$

$$F = W_eF_{ef} + W_pF_p, \quad S_y^* > 1.07 \quad \text{(A21)}$$

where the fully elastic forces, F_{es}, F_{es}, follow Hertzian theory, the fully plastic force, $F_p = \pi a^2\bar{p}$, and W_e and W_f are the weights for the fully elastic and fully plastic regimes, respectively, and are calculated as follows:

For $S_y^* \le 1.07$

$$W_e = e^{-1.6(\delta_n - 1.9)^{0.16}} \quad \text{(A22)}$$

$$W_p = 0.95 - e^{-0.58\delta_n^{0.3}} \quad \text{(A23)}$$

And for $S_y^* > 1.07$

$$W_e = e^{-1.7(\delta_n - 1.9)^{0.26}} \quad \text{(A24)}$$

$$W_p = 1 - e^{-0.465\delta_n^{0.45}} \quad \text{(A25)}$$

Appendix B

The following is a correction to the derivation in Ref. [126] of the critical amplitude during elastic–plastic sinusoidal contact. First, start with the sinusoidal pressure distribution used in Tripp et al. [131]:

$$p = \sigma_z(x, y, 0) = p_0\cos(\alpha x)\cos(\beta y) \quad \text{(B1)}$$

Tripp et al. provides the 3D stress distribution for this sinusoidal pressure distribution as

$$\sigma_x = p_0\left(\frac{\alpha^2}{\zeta^2} - \frac{\alpha^2}{\zeta}z + 2\nu\frac{\beta^2}{\zeta^2}\right)e^{-\zeta z}\cos(\alpha x)\cos(\beta y) \quad \text{(B2)}$$

$$\sigma_y = p_0\left(\frac{\beta^2}{\zeta^2} - \frac{\beta^2}{\zeta}z + 2\nu\frac{\alpha^2}{\zeta^2}\right)e^{-\zeta z}\cos(\alpha x)\cos(\beta y) \quad \text{(B3)}$$

$$\sigma_z = p_0(1 + \zeta z)e^{-\zeta z}\cos(\alpha x)\cos(\beta y) \quad \text{(B4)}$$

where

$$\zeta = \sqrt{\alpha^2 + \beta^2} \quad \text{(B5)}$$

Since, in the current case, wavelengths in the x and y directions are equal, $\beta = \alpha = 2\pi f$.

For complete contact, a uniform average pressure, p_0, on the substrate must be added to Eq. (B1). This results in all of the pressures being positive (i.e., no tensile or adhesive tractions). This pressure must be handled differently since it is uniformly applied over the surface. The stress in the z direction, σ_z, will be equal to this uniform pressure, p_0, everywhere in the substrate. This and the other stresses resulting from p_0 can be found by starting with Hooke's law

$$\epsilon_x(x,y,z) = \frac{1}{E}[\sigma_x - \upsilon(\sigma_y + \sigma_z)] \tag{B6}$$

$$\epsilon_y(x,y,z) = \frac{1}{E}[\sigma_y - \upsilon(\sigma_x + \sigma_z)] \tag{B7}$$

$$\epsilon_z(x,y,z) = \frac{1}{E}[\sigma_z - \upsilon(\sigma_x + \sigma_y)] \tag{B8}$$

Setting $\epsilon_x(x,y,z) = \epsilon_y(x,y,z) = 0$ (considering the periodic boundary conditions), and then by solving for the stress, the stress distribution is obtained as

$$\sigma_x(x,y,z) = p_0\left(\frac{v}{1-v}\right) \tag{B9}$$

$$\sigma_y(x,y,z) = p_0\left(\frac{v}{1-v}\right) \tag{B10}$$

$$\sigma_z(x,y,z) = p_0 \tag{B11}$$

However, the total stress distribution is given by the superposition of Eqs. (B2)–(B4) and (B9)–(B11):

$$\sigma_x(x,y,z) = p_0\left[\left(\frac{\alpha^2}{\zeta^2} - \frac{\alpha^2}{\zeta}z + 2\nu\frac{\beta^2}{\zeta^2}\right)e^{-\zeta z}\cos(\alpha x)\cos(\beta y) + \left(\frac{v}{1-v}\right)\right] \tag{B12}$$

$$\sigma_y(x,y,z) = p_0\left[\left(\frac{\beta^2}{\zeta^2} - \frac{\beta^2}{\zeta}z + 2\nu\frac{\alpha^2}{\zeta^2}\right)e^{-\zeta z}\cos(\alpha x)\cos(\beta y) + \left(\frac{v}{1-v}\right)\right] \tag{B13}$$

$$\sigma_z(x,y,z) = p_0\left[(1+\zeta z)e^{-\zeta z}\cos(\alpha x)\cos(\beta y) + 1\right] \tag{B14}$$

In addition, setting $p_0 = p^*$, the pressure to cause complete contact is given by

$$p_{cc} = \sigma_z(x,y,0) = p^*[1 + \cos(2\pi f x)\cos(2\pi f y)] \tag{B15}$$

The maximum stress will occur along the z axis at $x = y = 0$. Therefore, from Eqs. (B12) and (B13), $\sigma_x = \sigma_y$, $\zeta = 2\sqrt{2}\pi f$, and the stresses simplify to

$$\sigma_x = \sigma_y = p^*\left[\left(\frac{1}{2} - \sqrt{2}\pi f z + \nu\right)e^{-2\sqrt{2}\pi f z} + \left(\frac{v}{1-v}\right)\right] \tag{B16}$$

$$\sigma_z = p^*\left[(1 + 2\sqrt{2}fz)e^{-2\sqrt{2}\pi f z} + 1\right] \tag{B17}$$

To consider the initial state of stress which will cause plastic deformation in the surface, the von Mises stress can be simplified to be

$$\sigma_{vm} = \sigma_z - \sigma_x \tag{B18}$$

By substituting in the predicted stresses (Eqs. (B16) and (B17)) into Eq. (B18) and simplifying, the following prediction for the von Mises stress is obtained:

$$\sigma_{vm} = p^*\left[\left(\frac{1}{2} + 3\sqrt{2}\pi f z - v\right)e^{-2\sqrt{2}\pi f z} + 1 - \left(\frac{v}{1-v}\right)\right] \tag{B19}$$

The argument of the absolute value is always positive for the possible range of υ, so the vertical bars can be removed. To find the location on the z-axis where initial yielding will occur (z_0), the point of highest stress must be found. This is easily done by taking the derivative of Eq. (B19)

$$\frac{d\sigma_{vm}}{dz} = p^* 2\sqrt{2}\pi f\left(3\sqrt{2}\pi f z - v - 1\right)e^{-2\sqrt{2}\pi f z} \tag{B20}$$

then by setting Eq. (B20) to zero, z_0 can be found

$$z_0 = \frac{v+1}{3\sqrt{2}\pi f} \tag{B21}$$

This is then substituted into Eq. (B19), along with Eq. (40), to obtain the maximum von Mises stress in the surface

$$\sigma_{vm} = \sqrt{2}\pi E' \Delta f\left[\frac{3}{2}e^{-2/3(v+1)} + \left(\frac{1-2v}{1-v}\right)\right] \tag{B22}$$

Finally, by setting the von Mises stress (σ_{vm}) equal to the yield strength (S_y) and solving for Δ, the critical amplitude during complete contact, here denoted Δ_c, is found to equal

$$\Delta_c = \frac{\sqrt{2}S_y}{\pi E' f\left[3e^{-2/3(v+1)} + 2\left(\frac{1-2v}{1-v}\right)\right]} \tag{B23}$$

Appendix C

The case of elastic–plastic contact between an ellipsoid in contact with a smooth rigid flat was investigated by Li and Lin [114]. From their work, the critical load, F_c, can be expressed as

$$F_c = \frac{\pi^3 R_e^2}{6E'^2}[F_1(e)]^2\left[K(k,v,Z^*)S_y\right]^3 \tag{C1}$$

where $F_1(e)$ is directly from Johnson's book [5] (note that F_c is not required for predicting the behavior of elastic–plastic ellipsoid contact that is given later). $K(k,\nu,Z^*)$ is a function of the ellipticity of the contact area, k, and Poisson's ratio, ν, and denotes the factor of maximum contact pressure at yielding. It is given by

$$K(k,v,Z^*) = \frac{1}{\sqrt{3f(k,\nu,Z^*)}} \tag{C2}$$

where Z^* represents the dimensionless z coordinate of the function's maximum value.

R_e is the equivalent radius of curvature and is given by

$$R_e = \sqrt{R_{1x}R_{1y}} \tag{C3}$$

Then, the critical interference is given as

$$\delta_c = \left(\frac{9F_c^2}{16E'^2R_e}\right)^{1/3}\frac{2}{\pi}k^{1/2}[F_1(e)]^{-1/3}K(e) \tag{C4}$$

Likewise, the critical contact area is

$$A_c = \pi\left(\frac{3F_cR_e}{4E'}\right)^{2/3}[F_1(e)]^{2/3} \tag{C5}$$

and the critical average contact pressure is

$$(p_{ave})_c = \frac{2}{3}\left(\frac{6F_cE'^2}{\pi^3R_e^2}\right)^{1/3}[F_1(e)]^{-2/3} \tag{C6}$$

However, the following solutions use the critical values from spherical contact rather than Eqs. (C1)–(C6) for elliptical contact. The critical values from spherical contact, $(\delta_s)_c$, $(F_s)_c$, and $(A_s)_c$ can all be predicted from Eqs. (16)–(18). The critical values are

used to normalize the parameters in their equations, resulting in F^*, A^*, and δ^*. Following this, the dimensionless elastic contact load, dimensionless elastic contact area, and dimensionless elastic average contact pressure are

$$F^* = \frac{F}{(F_s)_c (R_e/R)^{1/2}} = \left(\frac{2}{\pi}\right)^{-3/2} k^{-3/4} [F_1(e)]^{1/2} K(e)^{-3/2} (\delta^*)^{3/2} \tag{C7}$$

$$A^* = \frac{A}{(A_s)_c (R_e/R)} = \left(\frac{2}{\pi}\right) k^{-1/2} [K(e)]^{-1} F_1(e) \delta^* \tag{C8}$$

$$\frac{p_{\text{ave}}}{(p_{\text{ave}.s})_c} = \left(\frac{R_e}{R}\right)^{-1/2} k^{-1/4} \left(\frac{2}{\pi}\right)^{-1/2} [F_1(e)]^{-1/2} [K(e)]^{-1/2} (\delta^*)^{1/2} \tag{C9}$$

If the dimensionless elastic average contact pressure is redefined as (p_{ave}/S_y), then it can be written as

$$p^* = \frac{p_{\text{ave}}}{S_y} = K(k, v, Z^*) \times \left(\frac{R_e}{R}\right)^{-1/2} k^{-1/4} \left(\frac{2}{\pi}\right)^{-1/2} [F_1(e)]^{-1/2} \times [K(e)]^{-1/2} (\delta^*)^{1/2} \tag{C10}$$

Based on the FEM data, the factor of maximum contact pressure at yielding, K, was fitted by

$$K(k, 0.3, Z^*) = 1.794 - 0.552k + 0.5669k^2 - 0.1928k^3 \tag{C11}$$

The critical dimensionless interference, $\delta/(\delta_s)_c$, in the fully plastic deformation regimes considering an ellipticity,k_e, in the range of $(1/5 \le k_e \le 1)$ is given by

$$\frac{\delta_p}{(\delta_s)_c} = 142.63 - 58.47k_e - 14.46k_e^2 \tag{C12}$$

Three different ellipticities ($k_e = 1, 1/2,$ and$1/5$) were considered in Li and Lin's study. Based on the FEM results, the equations of dimensionless elastic–plastic average contact pressure were fitted for these three cases and are given as

$$p^* = \frac{p_{\text{ave}}}{S_y} = \exp\left[a_1 + a_2 \ln\left(\frac{\delta}{(\delta_s)_c}\right) + a_3 \left(\ln\left(\frac{\delta}{(\delta_s)_c}\right)\right)^2\right] \tag{C13}$$

where $a_n (n = 1, 2,$ and $3)$ are the constants used in Eq. (C13) and given by

$$a_n = \begin{cases} a_1 = 0.0519, a_2 = 0.4191, a_3 = -0.0449, & \text{when } k_e = 1 \\ a_1 = -0.1847, a_2 = 0.4748, a_3 = -0.0472, & \text{when } k_e = 1/2 \\ a_1 = -0.4222, a_2 = 0.5744, a_3 = -0.0604, & \text{when } k_e = 1/5 \end{cases} \tag{C14}$$

Likewise, the dimensionless elastic–plastic contact area is given by

$$A^* = \frac{A}{[(A_s)_c R_e/R]} = \exp\left[b_1 + b_2 \ln\left(\frac{\delta}{(\delta_s)_c}\right)\right] \tag{C15}$$

where $b_n (n = 1$ and $2)$ are the constants used in Eq. (C15) and given by

$$b_n = \begin{cases} b_1 = -0.0493, b_2 = 1.1269, & \text{when } k_e = 1 \\ b_1 = -0.1550, b_2 = 1.1341, & \text{when } k_e = 1/2 \\ b_1 = -0.3412, b_2 = 1.1616, & \text{when } k_e = 1/5 \end{cases} \tag{C16}$$

The fitted equations of dimensionless average elastic–plastic contact force are also given as

$$F^* = \frac{F}{\left[(F_s)_c (R_e/R)^{1/2}\right]} = \exp\left[c_1 + c_2 \ln\left(\frac{\delta}{(\delta_s)_c}\right) + c_3 \left(\ln\left(\frac{\delta}{(\delta_s)_c}\right)\right)^2\right] \tag{C17}$$

where $c_n (n = 1, 2,$ and $3)$ are the constants used in Eq. (C17) and given by

$$c_n = \begin{cases} c_1 = -0.0177, c_2 = 1.4803, c_3 = -0.0323, & \text{when } k_e = 1 \\ c_1 = 0.0218, c_2 = 1.5372, c_3 = -0.0359, & \text{when } k_e = 1/2 \\ c_1 = 0.0768, c_2 = 1.6564, c_3 = -0.0468, & \text{when } k_e = 1/5 \end{cases} \tag{C18}$$

The dimensionless elastic–plastic contact area was expressed as a function of the dimensionless contact load

$$A^* = \exp\left[d_1 + d_2 \ln(F^*) + d_3 (\ln(F^*))^2\right] \tag{C19}$$

where $d_n (n = 1, 2,$ and $3)$ are the constants used in Eq. (C19) and given by

$$d_n = \begin{cases} d_1 = 0.0205, d_2 = 0.7070, d_3 = 0.0217, & \text{when } k_e = 1 \\ d_1 = -0.0678, d_2 = 0.6631, d_3 = 0.0232, & \text{when } k_e = 1/2 \\ d_1 = -0.2084, d_2 = 0.5976, d_3 = 0.0277, & \text{when } k_e = 1/5 \end{cases} \tag{C20}$$

References

[1] Hertz, H., 1882, "Über Die Berührung Fester Elastischer Körper," J. Reine Angew. Math., **92**, pp. 156–171.
[2] Jackson, R. L., Ghaednia, H., and Pope, S., 2015, "A Solution of Rigid–Perfectly Plastic Deep Spherical Indentation Based on Slip-Line Theory," Tribol. Lett., **58**(3), pp. 1–7.
[3] Green, I., 2002, "A Transient Dynamic Analysis of Mechanical Seals Including Asperity Contact and Face Deformation," Tribol. Trans., **45**(3), pp. 284–293.
[4] Manners, W., 2008, "Plastic Deformation of a Sinusoidal Surface," Wear, **264**, pp. 60–68.
[5] Johnson, K. L., 1987, *Contact Mechanics*, Cambridge University Press, Cambridge, UK.
[6] Bhushan, B., 1996, "Contact Mechanics of Rough Surfaces in Tribology: Single Asperity Contact," ASME Appl. Mech. Rev., **49**(5), pp. 275–298.
[7] Bhushan, B., 1998, "Contact Mechanics of Rough Surfaces in Tribology: Multiple Asperity Contact," Tribol. Lett., **4**(1), pp. 1–35.
[8] Barber, J. R., and Ciavarella, M., 2000, "Contact Mechanics," Int. J. Solids Struct., **37**(1–2), pp. 29–43.
[9] Adams, G. G., and Nosonovsky, M., 2000, "Contact Modeling—Forces," Tribol. Int., **33**(5–6), pp. 431–442.
[10] Bhushan, B., and Peng, W., 2002, "Contact Mechanics of Multilayered Rough Surfaces," ASME Appl. Mech. Rev., **55**(5), pp. 435–480.
[11] Ye, N., and Komvopoulos, K., 2003, "Indentation Analysis of Elastic-Plastic Homogeneous and Layered Media: Criteria for Determining the Real Material Hardness," ASME J. Tribol., **125**(4), pp. 685–691.
[12] Goltsberg, R., and Etsion, I., 2015, "A Universal Model for the Load-Displacement Relation in an Elastic Coated Spherical Contact," Wear, **322–323**, pp. 126–132.
[13] Song, W. P., Li, L. Q., Etsion, I., Ovcharenko, A., and Talke, F. E., 2014, "Yield Inception of a Soft Coating on a Flat Substrate Indented by a Rigid Sphere," Surf. Coat. Technol., **240**, pp. 444–449.
[14] Song, W. P., Li, L. Q., Ovcharenko, A., Jia, D., Etsion, I., and Talke, F. E., 2012, "Plastic Yield Inception of an Indented Coated Flat and Comparison With a Flattened Coated Sphere," Tribol. Int., **53**, pp. 61–67.
[15] Goltsberg, R., Etsion, I., and Davidi, G., 2011, "The Onset of Plastic Yielding in a Coated Sphere Compressed by a Rigid Flat," Wear, **271**(11–12), pp. 2968–2977.
[16] Chen, Z., Goltsberg, R., and Etsion, I., 2017, "A Universal Model for a Frictionless Elastic-Plastic Coated Spherical Normal Contact With Moderate to Large Coating Thicknesses," Tribol. Int., **114**(Suppl. C), pp. 485–493.
[17] Li, L., Etsion, I., Ovcharenko, A., and Talke, F. E., 2010, "The Onset of Plastic Yielding in a Spherical Shell Compressed by a Rigid Flat," ASME J. Appl. Mech., **78**(1), p. 011016.
[18] Zhou, B., and Prorok, B. C., 2010, "A New Paradigm in Thin Film Indentation," J. Mater. Res., **25**(9), pp. 1671–1678.
[19] Sullivan, M., and Prorok, B. C., 2015, "Evaluating Indent Pile-Up With Metallic Films on Ceramic-Like Substrates," J. Mater. Res., **30**(13), pp. 2046–2054.

[20] Cinar, A., and Sinclair, G. B., 1986, "Quasi-Static Normal Indentation of an Elasto-Plastic Half-Space by a Rigid Circular Cylinder of Infinite Length," Int. J. Solids Struct., **22**(8), pp. 919–934.
[21] Hamrock, B. J., 1994, *Fundamentals of Fluid Film Lubrication*, McGraw-Hill, New York.
[22] Green, I., 2005, "Poisson Ratio Effects and Critical Values in Spherical and Cylindrical Hertzian Contacts," Int. J. Appl. Mech. Eng., **10**(3), pp. 451–462.
[23] Dumas, G., and Baronet, C. N., 1971, "Elastoplastic Indentation of a Half-Space by an Infinitely Long Rigid Circular Cylinder," Int. J. Mech. Sci., **13**(6), pp. 519–530.
[24] Komvopoulos, K., 1989, "Elastic-Plastic Finite Element Analysis of Indented Layered Media," ASME J. Tribol., **111**(3), pp. 430–439.
[25] Akyuz, F. A., and Merwin, J. E., 1968, "Solution of Nonlinear Problems of Elastoplasticity by Finite Element Method," AIAA J., **6**(10), pp. 1825–1831.
[26] Liu, G., Zhu, J., Yu, L., and Wang, Q. J., 2001, "Elasto-Plastic Contact of Rough Surfaces," Tribol. Trans., **44**(3), pp. 437–443.
[27] Ishlinskii, A., 1944, "The Problem of Plasticity With Axial Symmetry and Brinell's Test," J. Appl. Math. Mech., **8**, pp. 201–224.
[28] Jackson, R. L., 2016, *A Solution of Rigid Plastic Cylindrical Indentation in Plane Strain*, STLE Tribology Frontiers, Chicago, IL.
[29] Sharma, A., and Jackson, R. L., 2016, "A Finite Element Study of Elasto-Plastic Cylindrical Contact Against a Rigid Flat," STLE Annual Meeting, Las Vegas, NV, May 15–19.
[30] Sharma, A., and Jackson, R. L., 2017, "A Finite Element Study of an Elasto-Plastic Disk or Cylindrical Contact Against a Rigid Flat in Plane Stress With Bilinear Hardening," Tribol. Lett., **65**(3), p. 112.
[31] Ghaednia, H., and Marghitu, D. B., 2016, "Permanent Deformation During the Oblique Impact With Friction," Arch. Appl. Mech., **86**(1–2), pp. 121–134.
[32] Ghaednia, H., Marghitu, D. B., and Jackson, R. L., 2014, "Predicting the Permanent Deformation After the Impact of a Rod With a Flat Surface," ASME J. Tribol., **137**(1), p. 011403.
[33] Ghaednia, H., Cermik, O., and Marghitu, D. B., 2015, "Experimental and Theoretical Study of the Oblique Impact of a Tennis Ball With a Racket," Proc. Inst. Mech. Eng., Part P, **229**(3), pp. 149–158.
[34] Gheadnia, H., Cermik, O., and Marghitu, D. B., 2015, "Experimental and Theoretical Analysis of the Elasto-Plastic Oblique Impact of a Rod With a Flat Surface," Int. J. Impact Eng., **86**, pp. 307–317.
[35] Kardel, K., Ghaednia, H., Carrano, A. L., and Marghitu, D. B., 2017, "Experimental and Theoretical Modeling of Behavior of 3D-Printed Polymers Under Collision With a Rigid Rod," Addit. Manuf., **14**, pp. 87–94.
[36] Stronge, W., 1991, "Unraveling Paradoxical Theories for Rigid Body Collisions," ASME J. Appl. Mech., **58**(4), pp. 1049–1055.
[37] Stronge, W. J., 1990, "Rigid Body Collisions With Friction," Proc. R. Soc., A, **431**, pp. 169–181.
[38] Stronge, W., 1992, "Energy Dissipated in Planar Collision," ASME J. Appl. Mech., **59**(3), pp. 681–682.
[39] Stronge, W., 1995, "Theoretical Coefficient of Restitution for Planer Impact of Rough Elasto-Plastic Bodies," Joint Applied Mechanics and Materials Summer Meeting, Los Angeles, CA, June 28–30.
[40] Jackson, R., Chusoipin, I., and Green, I., 2005, "A Finite Element Study of the Residual Stress and Deformation in Hemispherical Contacts," ASME J. Tribol., **127**(3), pp. 484–493.
[41] Ghaednia, H., Pope, S. A., Jackson, R. L., and Marghitu, D. B., 2016, "A Comprehensive Study of the Elasto-Plastic Contact of a Sphere and a Flat," Tribol. Int., **93(Pt. A)**, pp. 78–90.
[42] Thornton, C., and Ning, Z., 1994, "Oblique Impact of Elasto-Plastic Spheres," First International Particle Technology Forum, pp. 14–19.
[43] Thornton, C., 1997, "Coefficient of Restitution for Collinear Collisions of Elastic-Perfectly Plastic Spheres," ASME J. Appl. Mech., **64**(2), pp. 383–386.
[44] Li, L., Wu, C., and Thornton, C., 2001, "A Theoretical Model for the Contact of Elastoplastic Bodies," Proc. Inst. Mech. Eng., Part C, **216**(4), pp. 421–431.
[45] Wu, C.-Y., Li, L.-Y., and Thornton, C., 2005, "Energy Dissipation During Normal Impact of Elastic and Elastic–Plastic Spheres," Int. J. Impact Eng., **32**(1), pp. 593–604.
[46] Marghitu, D. B., Cojocaru, D., and Jackson, R. L., 2011, "Elasto-Plastic Impact of a Rotating Link With a Massive Surface," Int. J. Mech. Sci., **53**(4), pp. 309–315.
[47] Brake, M., 2012, "An Analytical Elastic-Perfectly Plastic Contact Model," Int. J. Solids Struct., **49**(22), pp. 3129–3141.
[48] Brake, M., 2015, "An Analytical Elastic Plastic Contact Model With Strain Hardening and Frictional Effects for Normal and Oblique Impacts," Int. J. Solids Struct., **62**, pp. 104–123.
[49] Ghaednia, H., Rostami, A., and Jackson, R. L., 2012, "The Influence of Thermal Expansion and Plastic Deformation on a Thermo-Electro Mechanical Spherical Asperity Contact," 58th IEEE Holm Conference on Electrical Contacts (Holm), Portland, OR, Sept. 23–26, pp. 16–22.
[50] Ghaednia, H., and Jackson, R. L., 2013, "On the Effect of Nanoparticles on the Real Area of Contact, Friction and Wear," ASME J. Tribol., **135**(4), p. 041603.
[51] Jackson, R. L., and Kogut, L., 2007, "Electrical Contact Resistance Theory for Anisotropic Conductive Films Considering Electron Tunneling and Particle Flattening," IEEE Trans. Compon. Packag. Technol., **30**(1), pp. 59–66.
[52] Jackson, R. L., and Green, I., 2005, "A Finite Element Study of Elasto-Plastic Hemispherical Contact Against a Rigid Flat," ASME J. Tribol., **127**(2), pp. 343–354.
[53] Jackson, R. L., Green, I., and Marghitu, D. B., 2010, "Predicting the Coefficient of Restitution of Impacting Elastic-Perfectly Plastic Spheres," Nonlinear Dyn., **60**(3), pp. 217–229.
[54] Etsion, I., Kligerman, Y., and Kadin, Y., 2005, "Unloading of an Elastic-Plastic Loaded Spherical Contact," Int. J. Solids Struct., **42**(13), pp. 3716–3729.
[55] Ghaednia, H., Jackson, R. L., and Gao, J., 2014, "A Third Body Contact Model for Particle Contaminated Electrical Contacts," 60th IEEE Holm Conference on Electrical Contacts (Holm), New Orleans, LA, Oct. 12–15, pp. 24–28.
[56] Follansbee, P., and Sinclair, G., 1984, "Quasi-Static Normal Indentation of an Elasto-Plastic Half-Space by a Rigid Sphere—I: Analysis," Int. J. Solids Struct., **20**(1), pp. 81–91.
[57] Sinclair, G., Follansbee, P., and Johnson, K., 1985, "Quasi-Static Normal Indentation of an Elasto-Plastic Half-Space by a Rigid Sphere—II. Results," Int. J. Solids Struct., **21**(8), pp. 865–888.
[58] Jackson, R. L., and Kogut, L., 2006, "A Comparison of Flattening and Indentation Approaches for Contact Mechanics Modeling of Single Asperity Contacts," ASME J. Tribol., **128**(1), pp. 209–212.
[59] Rodriguez, S. A., Alcala, J., and Martins Souza, R., 2011, "Effects of Elastic Indenter Deformation on Spherical Instrumented Indentation Tests: The Reduced Elastic Modulus," Philos. Mag., **91**(7–9), pp. 1370–1386.
[60] Olsson, E., and Larsson, P. L., 2016, "A Unified Model for the Contact Behaviour Between Equal and Dissimilar Elastic–Plastic Spherical Bodies," Int. J. Solids Struct., **81**, pp. 23–32.
[61] Alcalá, J., and Esqué-de los Ojos, D., 2010, "Reassessing Spherical Indentation: Contact Regimes and Mechanical Property Extractions," Int. J. Solids Struct., **47**(20), pp. 2714–2732.
[62] Alcala, J., Giannakopoulos, A., and Suresh, S., 1998, "Continuous Measurements of Load-Penetration Curves With Spherical Microindenters and the Estimation of Mechanical Properties," J. Mater. Res., **13**(5), pp. 1390–1400.
[63] Biwa, S., and Storåkers, B., 1995, "An Analysis of Fully Plastic Brinell Indentation," J. Mech. Phys. Solids, **43**(8), pp. 1303–1333.
[64] Mesarovic, S. D., and Fleck, N. A., 1999, "Spherical Indentation of Elastic–Plastic Solids," Proc. R. Soc. London A, **455**(1987), pp. 2707–2728.
[65] Richmond, O., Morrison, H., and Devenpeck, M., 1974, "Sphere Indentation With Application to the Brinell Hardness Test," Int. J. Mech. Sci., **16**(1), pp. 75–82.
[66] Tabor, D., 1948, "A Simple Theory of Static and Dynamic Hardness," Proc. R. Soc. London A, **192**(1029), pp. 247–274.
[67] Tabor, D., 2000, *The Hardness of Metals*, Oxford University Press, New York.
[68] Taljat, B., and Pharr, G., 2004, "Development of Pile-Up During Spherical Indentation of Elastic–Plastic Solids," Int. J. Solids Struct., **41**(14), pp. 3891–3904.
[69] Yu, W., and Blanchard, J. P., 1996, "An Elastic-Plastic Indentation Model and Its Solutions," J. Mater. Res., **11**(9), pp. 2358–2367.
[70] Quicksall, J. J., Jackson, R. L., and Green, I., 2004, "Elasto-Plastic Hemispherical Contact Models for Various Mechanical Properties," Proc. Inst. Mech. Eng., Part J, **218**(4), pp. 313–322.
[71] Jackson, R. L., and Green, I., 2003, "A Finite Element Study of Elasto-Plastic Hemispherical Contact," ASME Paper No. 2003-TRIB-0268.
[72] Wadwalkar, S. S., Jackson, R. L., and Kogut, L., 2010, "A Study of the Elastic-Plastic Deformation of Heavily Deformed Spherical Contacts," IMechE Part J, **224**(10), pp. 1091–1102.
[73] Zhao, Y., Maletta, D. M., and Chang, L., 2000, "An Asperity Microcontact Model Incorporating the Transition From Elastic Deformation to Fully Plastic Flow," ASME J. Tribol., **122**(1), pp. 86–93.
[74] Brinell, J., 1900, "Way of Determining the Hardness of Bodies and Some Applications of the Same," Tek. Tidskr., **5**, p. 69.
[75] Meyer, E., 1908, "Investigations of Hardness Testing and Hardness," Z. Phys., **9**, pp. 66–74.
[76] Abbott, E. J., and Firestone, F. A., 1933, "Specifying Surface Quality: A Method Based on Accurate Measurement and Comparison," Mech. Eng., **55**, pp. 569–572.
[77] Mohs, F., 1820, *The Characters of the Classes, Orders, Genera, and Species: Or, The Characteristic of the Natural History System of Mineralogy. Intended to Enable Student of Discriminate Minerals on Principles Similar to Those of Botany and Zoology*, W. and C. Tait, Edinburgh, Scotland.
[78] Lee, C., Masaki, S., and Kobayashi, S., 1972, "Analysis of Ball Indentation," Int. J. Mech. Sci., **14**(7), pp. 417–420.
[79] Mesarovic, S. D., and Fleck, N. A., 2000, "Frictionless Indentation of Dissimilar Elastic-Plastic Spheres," Int. J. Solids Struct., **37**(46–47), pp. 7071–7091.
[80] Kogut, L., and Komvopoulos, K., 2004, "Analysis of the Spherical Indentation Cycle for Elastic–Perfectly Plastic Solids," J. Mater. Res., **19**(12), pp. 3641–3653.
[81] Chaudhri, M. M., Hutchings, I. M., and Makin, P. L., 1984, "Plastic Compression of Spheres," Philos. Mag. A, **49**(4), pp. 493–503.
[82] Jackson, R. L., and Green, I., 2003, "A Statistical Model of Elasto-Plastic Asperity Contact Between Rough Surfaces," ASME/STLE International Tribology Conference, Ponte Vedra Beach, FL, Oct. 26–29, Paper No. 2003TRIB-102.
[83] Storåkers, B., Biwa, S., and Larsson, P.-L., 1997, "Similarity Analysis of Inelastic Contact," Int. J. Solids Struct., **34**(24), pp. 3061–3083.
[84] Jackson, R. L., Marghitu, D., and Green, I., 2006, "Predicting the Coefficient of Restitution of Impacting Elastic-Perfectly Plastic Spheres," ASME Paper No. IJTC2006-12292.
[85] Hardy, C., Baronet, C., and Tordion, G., 1971, "The Elasto-Plastic Indentation of a Half-Space by a Rigid Sphere," Int. J. Numer. Methods Eng., **3**(4), pp. 451–462.
[86] Komvopoulos, K., and Ye, N., 2001, "Three-Dimensional Contact Analysis of Elastic-Plastic Layered Media With Fractal Surface Topographies," ASME J. Tribol., **123**(3), pp. 632–640.

[87] Bartier, O., Hernot, X., and Mauvoisin, G., 2010, "Theoretical and Experimental Analysis of Contact Radius for Spherical Indentation," Mech. Mater., **42**(6), pp. 640–656.
[88] Brizmer, V., Zait, Y., Kligerman, Y., and Etsion, I., 2006, "The Effect of Contact Conditions and Material Properties on Elastic-Plastic Spherical Contact," J. Mech. Mater. Struct., **1**(5), pp. 865–879.
[89] Kharaz, A., and Gorham, D., 2000, "A Study of the Restitution Coefficient in Elastic-Plastic Impact," Philos. Mag. Lett., **80**(8), pp. 549–559.
[90] Kharaz, A., Gorham, D., and Salman, A., 1999, "Accurate Measurement of Particle Impact Parameters," Meas. Sci. Technol., **10**(1), p. 31.
[91] Johnson, K. L., 1968, "An Experimental Determination of the Contact Stresses Between Plastically Deformed Cylinders and Spheres," *Engineering Plasticity*, J. Heyman and F. A. Leckie, eds., Cambridge University Press, Cambridge, UK, pp. 341–361.
[92] Chang, W. R., Etsion, I., and Bogy, D. B., 1987, "An Elastic-Plastic Model for the Contact of Rough Surfaces," ASME J. Tribol., **109**(2), pp. 257–263.
[93] Kogut, L., and Etsion, I., 2002, "Elastic-Plastic Contact Analysis of a Sphere and a Rigid Flat," ASME J. Appl. Mech., **69**(5), pp. 657–662.
[94] Shankar, S., and Mayuram, M., 2008, "A Finite Element Based Study on the Elastic-Plastic Transition Behavior in a Hemisphere in Contact With a Rigid Flat," ASME J. Tribol., **130**(4), p. 044502.
[95] Lin, L. P., and Lin, J. F., 2006, "A New Method for Elastic-Plastic Contact Analysis of a Deformable Sphere and a Rigid Flat," ASME J. Tribol., **128**(2), pp. 221–229.
[96] Jackson, R. L., and Green, I., 2006, "A Statistical Model of Elasto-Plastic Asperity Contact Between Rough Surfaces," Tribol. Int., **39**(9), pp. 906–914.
[97] Brizmer, V., Kligerman, Y., and Etsion, I., 2006, "The Effect of Contact Conditions and Material Properties on the Elasticity Terminus of a Spherical Contact," Int. J. Solids Struct., **43**(18–19), pp. 5736–5749.
[98] Bar-Hen, M., and Etsion, I., 2017, "Experimental Study of the Effect of Coating Thickness and Substrate Roughness on Tool Wear During Turning," Tribol. Int., **110**, pp. 341–347.
[99] Wang, Z. Q., 2012, "A Compact and Easily Accepted Continuous Model for the Elastic-Plastic Contact of a Sphere and a Flat," ASME J. Appl. Mech., **80**(1), p. 014506.
[100] Ovcharenko, A., Halperin, G., Etsion, I., and Varenberg, M., 2006, "A Novel Test Rig for In Situ and Real Time Optical Measurement of the Contact Area Evolution During Pre-Sliding of a Spherical Contact," Tribol. Lett., **23**(1), pp. 55–63.
[101] Beheshti, A., and Khonsari, M. M., 2012, "Asperity Micro-Contact Models as Applied to the Deformation of Rough Line Contact," Tribol. Int., **52**, pp. 61–74.
[102] Beheshti, A., and Khonsari, M. M., 2014, "On the Contact of Curved Rough Surfaces: Contact Behavior and Predictive Formulas," ASME J. Appl. Mech., **81**(11), p. 111004.
[103] Sahoo, P., and Chatterjee, B., 2010, "A Finite Element Study of Elastic-Plastic Hemispherical Contact Behavior Against a Rigid Flat Under Varying Modulus of Elasticity and Sphere Radius," Engineering, **2**(4), pp. 205–211.
[104] Kogut, L., and Etsion, I., 2003, "A Semi-Analytical Solution for the Sliding Inception of a Spherical Contact," ASME J. Tribol., **125**(3), pp. 499–506.
[105] Megalingam, A., and Mayuram, M. M., 2014, "A Comprehensive Elastic-Plastic Single-Asperity Contact Model," Tribol. Trans., **57**(2), pp. 324–335.
[106] Ovcharenko, A., Halperin, G., Verberne, G., and Etsion, I., 2007, "In Situ Investigation of the Contact Area in Elastic–Plastic Spherical Contact During Loading–Unloading," Tribol. Lett., **25**(2), pp. 153–160.
[107] Kadin, Y., Kligerman, Y., and Etsion, I., 2006, "Multiple Loading–Unloading of an Elastic–Plastic Spherical Contact," Int. J. Solids Struct., **43**(22–23), pp. 7119–7127.
[108] Shankar, S., and Mayuram, M., 2008, "Effect of Strain Hardening in Elastic–Plastic Transition Behavior in a Hemisphere in Contact With a Rigid Flat," Int. J. Solids Struct., **45**(10), pp. 3009–3020.
[109] Sahoo, P., Chatterjee, B., and Adhikary, D., 2010, "Finite Element Based Elastic-Plastic Contact Behavior of a Sphere Against a Rigid Flat-Effect of Strain Hardening," Int. J. Eng. Technol., **2**(1), pp. 1–6.
[110] Zhao, B., Zhang, S., Wang, Q. F., Zhang, Q., and Wang, P., 2015, "Loading and Unloading of a Power-Law Hardening Spherical Contact Under Stick Contact Condition," Int. J. Mech. Sci., **94–95**, pp. 20–26.
[111] Horng, J. H., 1998, "An Elliptic Elastic-Plastic Asperity Microcontact Model for Rough Surfaces," ASME J. Tribol., **120**(1), pp. 82–88.
[112] Jeng, Y.-R., and Wang, P.-Y., 2003, "An Elliptical Microcontact Model Considering Elastic, Elastoplastic, and Plastic Deformation," ASME J. Tribol., **125**(2), pp. 232–240.
[113] Jamari, J., and Schipper, D. J., 2006, "An Elastic–Plastic Contact Model of Ellipsoid Bodies," Tribol. Lett., **21**(3), pp. 262–271.
[114] Lin, P. L., and Lin, J. F., 2007, "An Elliptical Elastic-Plastic Microcontact Model Developed for an Ellipsoid in Contact With a Smooth Rigid Flat," ASME J. Tribol., **129**(4), pp. 772–782.
[115] Westergaard, H. M., 1939, "Bearing Pressures and Cracks," ASME J. Appl. Mech., **6**, pp. 49–53.
[116] Krithivasan, V., and Jackson, R. L., 2007, "An Analysis of Three-Dimensional Elasto-Plastic Sinusoidal Contact," Tribol. Lett., **27**(1), pp. 31–43.
[117] Gao, Y. F., Bower, A. F., Kim, K. S., Lev, L., and Cheng, Y. T., 2006, "The Behavior of an Elastic-Perfectly Plastic Sinusoidal Surface Under Contact Loading," Wear, **261**(2), pp. 145–154.
[118] Sun, F., Van der Giessen, E., and Nicola, L., 2015, "Interaction Between Neighboring Asperities During Flattening: A Discrete Dislocation Plasticity Analysis," Mech. Mater., **90**, pp. 157–165.
[119] Wilson, W. E., Angadi, S. V., and Jackson, R. L., 2010, "Surface Separation and Contact Resistance Considering Sinusoidal Elastic-Plastic Multi-Scale Rough Surface Contact," Wear, **268**(1–2), pp. 190–201.
[120] Williamson, J. B. P., and Hunt, R. T., 1972, "Asperity Persistence and the Real Area of Contact Between Rough Surfaces," Proc. R. Soc. London A, **327**(1569), pp. 147–157.
[121] Guduru, P., 2007, "Detachment of a Rigid Solid From an Elastic Wavy Surface: Theory," J. Mech. Phys. Solids, **55**(3), pp. 445–472.
[122] Guduru, P., and Bull, C., 2007, "Detachment of a Rigid Solid From an Elastic Wavy Surface: Experiments," J. Mech. Phys. Solids, **55**(3), pp. 473–488.
[123] Waters, J. F., Lee, S., and Guduru, P. R., 2009, "Mechanics of Axisymmetric Wavy Surface Adhesion: JKR–DMT Transition Solution," Int. J. Solids Struct., **46**(5), pp. 1033–1042.
[124] Saha, S., Xu, Y., and Jackson, R. L., 2016, "Perfectly Elastic Axisymmetric Sinusoidal Surface Asperity Contact," ASME J. Tribol., **138**(3), p. 031401.
[125] Rostami, A., Goedecke, A., Mock, R., and Jackson, R. L., 2014, "Three-Dimensional Modeling of Elasto-Plastic Sinusoidal Contact Under Time Dependent Deformation Due to Stress Relaxation," Tribol. Int., **73**, pp. 25–35.
[126] Jackson, R. L., Krithivasan, V., and Wilson, W. E., 2008, "The Pressure to Cause Complete Contact Between Elastic-Plastic Sinusoidal Surfaces," Proc. Inst. Mech. Eng., Part J, **222**(7), pp. 857–864.
[127] Song, H., Van der Giessen, E., and Liu, X., 2016, "Strain Gradient Plasticity Analysis of Elasto-Plastic Contact Between Rough Surfaces," J. Mech. Phys. Solids, **96**, pp. 18–28.
[128] Saha, S., and Jackson, R. L., 2016, "Elastic-Plastic Axisymmetric Sinusoidal Surface Asperity Contact," IEEE 62nd Holm Conference on Electrical Contacts (Holm), Clearwater Beach, FL, Oct. 9–12, pp. 17–24.
[129] Liu, M., and Proudhon, H., 2016, "Finite Element Analysis of Contact Deformation Regimes of an Elastic-Power Plastic Hardening Sinusoidal Asperity," Mech. Mater., **103**, pp. 78–86.
[130] Johnson, K. L., Greenwood, J. A., and Higginson, J. G., 1985, "The Contact of Elastic Regular Wavy Surfaces," Int. J. Mech. Sci., **27**(6), pp. 383–396.
[131] Tripp, J. H., Kuilenburg, J. V., Morales-Espejel, G. E., and Lugt, P. M., 2003, "Frequency Response Functions and Rough Surface Stress Analysis," Tribol. Trans., **46**(3), pp. 376–382.
[132] Rostami, A., and Jackson, R. L., 2013, "Predictions of the Average Surface Separation and Stiffness Between Contacting Elastic and Elastic-Plastic Sinusoidal Surfaces," Proc. Inst. Mech. Eng. J, **227**(12), pp. 1376–1385.
[133] Cattaneo, C., 1938, "Sul Contatto Di Due Corpi Elastici: Distribuzione Locale Degli Sforzi," Rend. Accad. Naz. Lincei, **27**(6), pp. 342–348.
[134] Mindlin, R. D., 1949, "Compliance of Elastic Bodies in Contact," ASME J. Appl. Mech., **16**(3), pp. 259–268.
[135] Mindlin, R. D., and Deresiewicz, H., 1953, "Elastic Spheres in Contact Under Varying Oblique Forces," ASME J. Appl. Mech., **20**(3), pp. 327–344.
[136] Keer, L. M., Ahmadi, N., and Mura, T., 1984, "Tangential Loading of Elastic Bodies in Contact," Comput. Struct., **19**(1–2), pp. 93–101.
[137] Hamilton, G. M., 1983, "Explicit Equations for the Stresses Beneath a Sliding Spherical Contact," Proc. Inst. Mech. Eng. C, **197**, pp. 53–59.
[138] Sackfield, A., and Hills, D. A., 1988, "Sliding Contact Between Dissimilar Elastic Bodies," ASME J. Tribol., **110**(4), pp. 592–596.
[139] Bowden, F. P., and Tabor, D., 1967, *Friction and Lubrication*, Methuen, London.
[140] Courtney-Pratt, J. S., and Eisner, E., 1957, "The Effect of a Tangential Force on the Contact of Metallic Bodies," Proc. R. Soc. London Ser. A, **238**(1215), pp. 529–550.
[141] Tabor, D., 1959, "Junction Growth in Metallic Friction—The Role of Combined Stresses and Surface Contamination," Proc. R. Soc. London Ser. A, **251**(1266), pp. 378–393.
[142] Zhang, H., Chang, L., Webster, M. N., and Jackson, A., 2003, "Effects of Friction on the Contact and Deformation Behavior in Sliding Asperity Contacts," Tribol. Trans., **46**(4), pp. 514–521.
[143] Brizmer, V., Kligerman, Y., and Etsion, I., 2007, "Elastic-Plastic Spherical Contact Under Combined Normal and Tangential Loading in Full Stick," Tribol. Lett., **25**(1), pp. 61–70.
[144] Brizmer, V., Kligerman, Y., and Etsion, I., 2007, "A Model for Junction Growth of a Spherical Contact Under Full Stick Condition," ASME J. Tribol., **129**(4), pp. 783–790.
[145] Zolotarevskiy, V., Kligerman, Y., and Etsion, I., 2011, "The Evolution of Static Friction for Elastic-Plastic Spherical Contact in Pre-Sliding," ASME J. Tribol., **133**(3), p. 034502.
[146] Li, L., Etsion, I., and Talke, F. E., 2010, "Contact Area and Static Friction of Rough Surfaces With High Plasticity Index," ASME J. Tribol., **132**(3), p. 031401.
[147] Eriten, M., Polycarpou, A. A., and Bergman, L. A., 2010, "Physics-Based Modeling for Partial Slip Behavior of Spherical Contacts," Int. J. Solids Struct., **47**(18–19), pp. 2554–2567.
[148] Patil, D. B., and Eriten, M., 2014, "Effects of Interfacial Strength and Roughness on the Static Friction Coefficient," Tribol. Lett., **56**(2), pp. 355–374.
[149] Wu, A. Z., Shi, X., and Polycarpou, A. A., 2012, "An Elastic-Plastic Spherical Contact Model Under Combined Normal and Tangential Loading," ASME J. Appl. Mech., **79**(5), p. 051001.
[150] Etsion, I., Levinson, O., Halperin, G., and Varenberg, M., 2005, "Experimental Investigation of the Elastic–Plastic Contact Area and Static Friction of a Sphere on Flat," ASME J. Tribol., **127**(1), pp. 47–51.

[151] Ovcharenko, A., Halperin, G., and Etsion, I., 2008, "Experimental Study of Adhesive Static Friction in a Spherical Elastic-Plastic Contact," ASME J. Tribol., **130**(2), p. 021401.
[152] Ibrahim Dickey, R. D., Jackson, R. L., and Flowers, G. T., 2011, "Measurements of the Static Friction Coefficient Between Tin Surfaces and Comparison to a Theoretical Model," ASME J. Tribol., **133**(3), p. 031408.
[153] Ovcharenko, A., Halperin, G., and Etsion, I., 2008, "In Situ and Real-Time Optical Investigation of Junction Growth in Spherical Elastic–Plastic Contact," Wear, **264**(11–12), pp. 1043–1050.
[154] Etsion, I., 2010, "Revisiting the Cattaneo–Mindlin Concept of Interfacial Slip in Tangentially Loaded Compliant Bodies," ASME J. Tribol., **132**(2), p. 020801.
[155] Cattaneo, C., 1938, "Sul contatto di due corpi elastici: distribuzione locale degli sforzi," Rend. Accad. Naz. Lincei, **27**(6), pp. 342–348.
[156] Wang, X., Xu, Y., and Jackson, R. L., 2017, "Elastic–Plastic Sinusoidal Waviness Contact Under Combined Normal and Tangential Loading," Tribol. Lett., **65**(1), p. 45.
[157] Gao, Y. F., and Bower, A. F., 2006, "Elastic-Plastic Contact of a Rough Surface With Weierstrass Profile," Proc. R. Soc. A, **462**(2065), pp. 319–348.
[158] Faulkner, A., and Arnell, R. D., 2000, "Development of a Finite Element Model to Simulate the Sliding Interaction Between Two, Three-Dimensional, Elastoplastic, Hemispherical Asperities," Wear, **242**(1), pp. 114–122.
[159] Jackson, R. L., Duvvuru, R. S., Meghani, H., and Mahajan, M., 2007, "An Analysis of Elasto-Plastic Sliding Spherical Asperity Interaction," Wear, **262**(1–2), pp. 210–219.
[160] Boucly, V., Nelias, D., and Green, I., 2007, "Modeling of the Rolling and Sliding Contact Between Two Asperities," ASME J. Tribol., **129**(2), pp. 235–245.
[161] Vijaywargiya, R., and Green, I., 2007, "A Finite Element Study of the Deformation, Forces, Stress Formation, and Energy Loss in Sliding Cylindrical Contacts," Int. J. Non-Linear Mech., **42**(7), pp. 914–927.
[162] Mulvihill, D. M., Kartal, M. E., Nowell, D., and Hills, D. A., 2011, "An Elastic-Plastic Asperity Interaction Model for Sliding Friction," Tribol. Int., **44**(12), pp. 1679–1694.
[163] Shi, X., Zou, Y., and Fang, H., 2016, "Numerical Investigation of the Three-Dimensional Elastic–Plastic Sloped Contact Between Two Hemispheric Asperities," ASME J. Appl. Mech., **83**(10), p. 101004.
[164] Zhao, B., Zhang, S., and Keer, L. M., 2016, "Semi-Analytical and Numerical Analysis of Sliding Asperity Interaction for Power-Law Hardening Materials," Wear, **364–365**, pp. 184–192.
[165] Vadgama, B. N., Jackson, R. L., and Harris, D. K., 2015, "Molecular Scale Analysis of Dry Sliding Copper Asperities," Appl. Nanosci., **5**(4), pp. 469–480.
[166] Gao, J., Luedtke, W. D., Gourdon, D., Ruths, M., Israelachvili, J. N., and Landman, U., 2004, "Frictional Forces and Amontons' Law: From the Molecular to the Macroscopic Scale," J. Phys. Chem. B, **108**(11), pp. 3410–3425.
[167] Zhong, J., Adams, J. B., and Hector, L. G., 2003, "Molecular Dynamics Simulations of Asperity Shear in Aluminum," J. Appl. Phys., **94**(7), pp. 4306–4314.
[168] Chang, W. R., Etsion, I., and Bogy, D., 1988, "Adhesion Model for Metallic Rough Surfaces," ASME J. Tribol., **110**(1), pp. 50–56.
[169] Derjaguin, B. V., Muller, V. M., and Toporov, Y. P., 1975, "Effect of Contact Deformations on Adhesion of Particles," J. Colloid Interface Sci., **53**(2), pp. 314–326.
[170] Mesarovic, S. D., and Johnson, K., 2000, "Adhesive Contact of Elastic–Plastic Spheres," J. Mech. Phys. Solids, **48**(10), pp. 2009–2033.
[171] Maugis, D., 1992, "Adhesion of Spheres: The JKR-DMT Transition Using a Dugdale Model," J. Colloid Interface Sci., **150**(1), pp. 243–269.
[172] Kogut, L., and Etsion, I., 2003, "Adhesion in Elastic-Plastic Spherical Microcontact," J. Colloid Interface Sci., **261**(2), pp. 372–379.
[173] Sahoo, P., and Banerjee, A., 2005, "Asperity Interaction in Elastic-Plastic Contact of Rough Surfaces in Presence of Adhesion," J. Phys. D, **38**(16), pp. 2841–2847.
[174] Johnson, K. L., Kendall, K., and Roberts, A. D., 1971, "Surface Energy and the Contact of Elastic Solids," Proc. R. Soc. London Ser. A, **324**(1558), pp. 301–313.
[175] Du, Y., Chen, L., McGruer, N. E., Adams, G. G., and Etsion, I., 2007, "A Finite Element Model of Loading and Unloading of an Asperity Contact With Adhesion and Plasticity," J. Colloid Interface Sci., **312**(2), pp. 522–528.
[176] Du, Y., Adams, G. G., McGruer, N. E., and Etsion, I., 2008, "A Parameter Study of Separation Modes of Adhering Microcontacts," J. Appl. Phys., **103**(6), p. 064902.
[177] Kadin, Y., Kligerman, Y., and Etsion, I., 2008, "Loading–Unloading of an Elastic–Plastic Adhesive Spherical Microcontact," J. Colloid Interface Sci., **321**(1), pp. 242–250.
[178] Tabor, D., 1977, "Surface Forces and Surface Interactions," J. Colloid Interface Sci., **58**(1), pp. 2–13.
[179] Liu, G., Wang, Q., and Lin, C., 1999, "A Survey of Current Models for Simulating the Contact Between Rough Surfaces," Tribol. Trans., **42**(3), pp. 581–591.
[180] Krick, B. A., Vail, J. R., Persson, B. N. J., and Sawyer, W. G., 2012, "Optical In Situ Micro Tribometer for Analysis of Real Contact Area for Contact Mechanics, Adhesion, and Sliding Experiments," Tribol. Lett., **45**(1), pp. 185–194.
[181] McBride, J. W., 2006, "The Loaded Surface Profile: A New Technique for the Investigation of Contact Surfaces," 23rd International Conference on Electrical Contacts (ICEC), Sendai, Japan, June 6–9, pp. 150–156.
[182] Jackson, R. L., Down, M. P., Hong, L., and McBride, J. W., 2014, "A Comparison of the Predictions of a Multiscale Model and Optical Real Area of Contact Measurements," IEEE 60th Holm Conference Electrical Contacts (Holm), New Orleans, LA, Oct. 12–15, pp. 1–8.
[183] McBride, J. W., and Cross, K. C., 2008, "An Experimental Investigation of the Contact Area Between a Glass Plane and Both Metallic and Carbon-Nano-Tube Electrical Contacts," 54th IEEE Holm Conference on Electrical Contacts (Holm), Orlando, FL, Oct. 27–29, pp. 325–331.
[184] Maegawa, S., Itoigawa, F., and Nakamura, T., 2015, "Optical Measurements of Real Contact Area and Tangential Contact Stiffness in Rough Contact Interface Between an Adhesive Soft Elastomer and a Glass Plate," J. Adv. Mech. Des. Syst., Manuf., **9**(5), p. JAMDSM0069.
[185] Jackson, R. L., Ghaednia, H., Elkady, Y. A., Bhavnani, S. H., and Knight, R. W., 2012, "A Closed-Form Multiscale Thermal Contact Resistance Model," IEEE Trans. Compon. Packag. Technol., **2**(7), pp. 1158–1171.
[186] Almeida, L., Ramadoss, R., Jackson, R., Ishikawa, K., and Yu, Q., 2006, "Study of the Electrical Contact Resistance of Multi-Contact MEMS Relays Fabricated Using the Metal MUMPs Process," J. Micromech. Microeng., **16**(7), pp. 1189–1194.
[187] Drinkwater, B. W., Dwyer-Joyce, R. S., and Cawley, P., 1996, "A Study of the Interaction Between Ultrasound and a Partially Contacting Solid-Solid Interface," Proc. R. Soc. London A, **452**(1955), pp. 2613–2628.
[188] Dwyer-Joyce, R. S., Drinkwater, B. W., and Quinn, A. M., 2001, "The Use of Ultrasound in the Investigation of Rough Surface Interfaces," ASME J. Tribol., **123**(1), pp. 8–16.
[189] Greenwood, J. A., and Wu, J. J., 2001, "Surface Roughness and Contact: An Apology," Meccanica, **36**(6), pp. 617–630.
[190] Luan, B., and Robbins, M. O., 2005, "The Breakdown of Continuum Models for Mechanical Contacts," Nature, **435**(7044), pp. 929–932.
[191] Jackson, R. L., and Green, I., 2011, "On the Modeling of Elastic Contact Between Rough Surfaces," Tribol. Trans., **54**(2), pp. 300–314.
[192] Yastrebov, V. A., Durand, J., Proudhon, H., and Cailletaud, G., 2011, "Rough Surface Contact Analysis by Means of the Finite Element Method and of a New Reduced Model," C. R. Mec., **339**(7–8), pp. 473–490.
[193] Xu, Y., Jackson, R. L., and Marghitu, D. B., 2014, "Statistical Model of Nearly Complete Elastic Rough Surface Contact," Int. J. Solids Struct., **51**(5), pp. 1075–1088.
[194] Xu, Y., and Jackson, R. L., 2017, "Statistical Models of Nearly Complete Elastic Rough Surface Contact-Comparison With Numerical Solutions," Tribol. Int., **105**, pp. 274–291.
[195] Almqvist, A., Campañá, C., Prodanov, N., and Persson, B. N. J., 2011, "Interfacial Separation Between Elastic Solids With Randomly Rough Surfaces: Comparison Between Theory and Numerical Techniques," J. Mech. Phys. Solids, **59**(11), pp. 2355–2369.
[196] Campañá, C., Müser, M. H., and Robbins, M. O., 2008, "Elastic Contact Between Self-Affine Surfaces: Comparison of Numerical Stress and Contact Correlation Functions With Analytic Predictions," J. Phys., **20**(35), p. 354013.
[197] Ciavarella, M., 2016, "An Upper Bound to Multiscale Roughness-Induced Adhesion Enhancement," Tribol. Int., **102**, pp. 99–102.
[198] Bhushan, B., and Majumdar, A., 1992, "Elastic-Plastic Contact Model for Bifractal Surfaces," Wear, **153**(1), pp. 53–64.
[199] Majumdar, A., and Bhushan, B., 1990, "Role of Fractal Geometry in Roughness Characterization and Contact Mechanics of Surfaces," ASME J. Tribol., **112**(2), pp. 205–216.
[200] Majumdar, A., and Bhushan, B., 1991, "Fractal Model of Elastic-Plastic Contact Between Rough Surfaces," ASME J. Tribol., **113**(1), pp. 1–11.
[201] Barber, J. R., 2003, "Bounds on the Electrical Resistance Between Contacting Elastic Rough Bodies," Proc. R. Soc. London A, **459**(2029), pp. 53–66.
[202] Ciavarella, M., Delfine, G., and Demelio, G., 2006, "A 'Re-Vitalized' Greenwood and Williamson Model of Elastic Contact Between Fractal Surfaces," J. Mech. Phys. Solids, **54**(12), pp. 2569–2591.
[203] Ciavarella, M., and Demelio, G., 2001, "Elastic Multiscale Contact of Rough Surfaces: Archard's Model Revisited and Comparisons With Modern Fractal Models," ASME J. Appl. Mech., **68**(3), pp. 496–498.
[204] Ciavarella, M., Murolo, G., Demelio, G., and Barber, J. R., 2004, "Elastic Contact Stiffness and Contact Resistance for the Weierstrass Profile," J. Mech. Phys. Solids, **52**(6), pp. 1247–1265.
[205] Goedecke, A., Jackson, R., and Mock, R., 2013, "A Fractal Expansion of a Three Dimensional Elastic–Plastic Multi-Scale Rough Surface Contact Model," Tribol. Int., **59**, pp. 230–239.
[206] Goedecke, A., and Mock, R., 2008, "A New Fractal Model for Dynamic Contact Phenomena Including Friction," COMSOL Conference, Hanover, Germany, Nov. 4–6.
[207] Hyun, S., Pel, L., Molinari, J. F., and Robbins, M. O., 2004, "Finite-Element Analysis of Contact Between Elastic Self-Affine Surfaces," Phys. Rev. E, **70**(2), p. 026117.
[208] Jackson, R. L., 2010, "An Analytical Solution to an Archard-Type Fractal Rough Surface Contact Model," Tribol. Trans., **53**(4), pp. 543–553.
[209] Kenneth, F., 1990, *Fractal Geometry: Mathematical Foundations and Applications*, Wiley, Hoboken, NJ, p. 38.
[210] Komvopoulos, K., and Yan, W., 1998, "Three-Dimensional Elastic-Plastic Fractal Analysis of Surface Adhesion in Microelectromechanical Systems," ASME J. Tribol., **120**(4), pp. 808–813.
[211] Pei, L., Hyun, S., Molinari, J. F., and Robbins, M. O, 2005, "Finite Element Modeling of Elasto-Plastic Contact Between Rough Surfaces," J. Mech. Phys. Solids, **53**(11), pp. 2385–2409.
[212] Peng, Y. F., and Guo, Y. B., 2007, "An Adhesion Model for Elastic-Plastic Fractal Surfaces," J. Appl. Phys., **102**(5), p. 053510.
[213] Warren, T. L., and Krajcinovic, D., 1995, "Fractal Models of Elastic-Perfectly Plastic Contact of Rough Surfaces Based on the Cantor Set," Int. J. Solids Struct., **32**(19), pp. 2907–2922.

[214] Willner, K., 2004, "Elasto-Plastic Normal Contact of Three-Dimensional Fractal Surfaces Using Halfspace Theory," ASME J. Tribol., **126**(1), pp. 28–33.
[215] Yan, W., and Komvopoulos, K., 1998, "Contact Analysis of Elastic-Plastic Fractal Surfaces," J. Appl. Phys., **84**(7), pp. 3617–3624.
[216] Zhang, X., Xu, Y., and Jackson, R. L., 2017, "An Analysis of Generated Fractal and Measured Rough Surfaces in Regards to Their Multi-Scale Structure and Fractal Dimension," Tribol. Int., **105**, pp. 94–101.
[217] Whitehouse, D., 2001, "Fractal or Fiction," Wear, **249**(5), pp. 345–353.
[218] Borodich, F. M., Pepelyshev, A., and Savencu, O., 2016, "Statistical Approaches to Description of Rough Engineering Surfaces at Nano and Microscales," Tribol. Int., **103**, pp. 197–207.
[219] Zhang, X., and Jackson, R. L., 2017, "An Analysis of the Multiscale Structure of Surfaces With Various Finishes," Tribol. Trans., **60**(1), pp. 121–134.
[220] Jacobs, T., Junge, T., and Pastewka, L., 2017, "Quantitative Characterization of Surface Topography Using Spectral Analysis," Surf. Topogr., **5**(1), p. 013001.
[221] Jacq, C., Nélias, D., Lormand, G., and Girodin, D., 2002, "Development of a Three-Dimensional Semi-Analytical Elastic-Plastic Contact Code," ASME J. Tribol., **124**(4), pp. 653–667.
[222] Sainsot, P., Jacq, C., and Nelias, D., 2002, "A Numerical Model for Elasto-plastic Rough Contact," Comput. Model. Eng. Sci., **3**(4), pp. 497–506.
[223] Wang, Z.-J., Wang, W.-Z., Hu, Y.-Z., and Wang, H., 2010, "A Numerical Elastic–Plastic Contact Model for Rough Surfaces," Tribol. Trans., **53**(2), pp. 224–238.
[224] Liu, S., and Wang, Q., 2000, "A Three-Dimensional Thermomechanical Model of Contact Between Non-Conforming Rough Surfaces," ASME J. Tribol., **123**(1), pp. 17–26.
[225] Liu, H., Leray, D., Colin, S., Pons, P., and Broue, A., 2012, "Finite Element Based Surface Roughness Study for Ohmic Contact of Microswitches," IEEE 58th Holm Conference on Electrical Contacts (Holm), Portland, OR, Sept. 23–26, pp. 1–10.
[226] Sahoo, P., and Ghosh, N., 2007, "Finite Element Contact Analysis of Fractal Surfaces," J. Phys. D, **40**(14), pp. 42–45.
[227] Thompson, M. K., and Thompson, J. M., 2010, "Considerations for the Incorporation of Measured Surfaces in Finite Element Models," Scanning, **32**(4), pp. 183–198.
[228] Thompson, M. K., 2011, "A Comparison of Methods to Evaluate the Behavior of Finite Element Models With Rough Surfaces," Scanning, **33**(5), pp. 353–369.
[229] Wang, F. S., Block, J. M., Chen, W. W., Martini, A., Zhou, K., Keer, L. M., and Wang, Q. J., 2009, "A Multilevel Model for Elastic-Plastic Contact Between a Sphere and a Flat Rough Surface," ASME J. Tribol., **131**(2), p. 021409.
[230] Venner, C. H., and Lubrecht, A. A., 2000, *Multi-Level Methods in Lubrication*, Elsevier, New York.
[231] Megalingam, A., and Mayuram, M., 2012, "Comparative Contact Analysis Study of Finite Element Method Based Deterministic, Simplified Multi-Asperity and Modified Statistical Contact Models," ASME J. Tribol., **134**(1), p. 014503.
[232] Greenwood, J. A., and Williamson, J. B. P., 1966, "Contact of Nominally Flat Surfaces," Proc. R. Soc. London A, **295**(1442), pp. 300–319.
[233] Zhuravlev, V. A., 2007, "On Question of Theoretical Justification of the Amontons–Coulomb Law for Friction of Unlubricated Surfaces," Proc. Inst. Mech. Eng., Part J, **221**(8), pp. 893–898.
[234] Lee, C.-H., Eriten, M., and Polycarpou, A. A., 2010, "Application of Elastic-Plastic Static Friction Models to Rough Surfaces With Asymmetric Asperity Distribution," ASME J. Tribol., **132**(3), p. 031602.
[235] Yu, N., and Polycarpou, A. A., 2004, "Combining and Contacting of Two Rough Surfaces With Asymmetric Distribution of Asperity Heights," ASME J. Tribol., **126**(2), pp. 225–232.
[236] Kogut, L., and Etsion, I., 2003, "A Finite Element Based Elastic-Plastic Model for the Contact of Rough Surfaces," Tribol. Trans., **46**(3), pp. 383–390.
[237] Sepehri, A., and Farhang, K., 2009, "Closed-Form Equations for Three Dimensional Elastic-Plastic Contact of Nominally Flat Rough Surfaces," ASME J. Tribol., **131**(4), p. 041402.
[238] Abdo, J., and Farhang, K., 2005, "Elastic–Plastic Contact Model for Rough Surfaces Based on Plastic Asperity Concept," Int. J. Non-Linear Mech., **40**(4), pp. 495–506.
[239] Jeng, Y.-R., and Peng, S.-R., 2005, "Elastic-Plastic Contact Behavior Considering Asperity Interactions for Surfaces With Various Height Distributions," ASME J. Tribol., **128**(2), pp. 245–251.
[240] Jackson, R. L., Saha, S., and Xu, Y., 2015, "The Influence of Single Asperity Models on Predicting Contact Between Elastic Rough Surfaces Using Statistical Methods," STLE Tribology Frontiers Conference, Denver, CO, Oct. 25–27.
[241] Majumdar, A., and Tien, C. L., 1990, "Fractal Characterization and Simulation of Rough Surfaces," Wear, **136**(2), pp. 313–327.
[242] Kogut, L., and Jackson, R. L., 2005, "A Comparison of Contact Modeling Utilizing Statistical and Fractal Approaches," ASME J. Tribol., **128**(1), pp. 213–217.
[243] Greenwood, J. A., 2006, "A Simplified Elliptical Model of Rough Surface Contact," Wear, **261**(2), pp. 191–200.
[244] Bush, A. W., Gibson, R. D., and Thomas, T. R., 1975, "The Elastic Contact of Rough Surfaces," Wear, **35**, pp. 87–111.
[245] Hassan, E., and George, G. A., 2007, "An Elastic–Plastic Finite Element Analysis of Interacting Asperities in Contact With a Rigid Flat," J. Phys. D, **40**(23), pp. 7432–7439.
[246] Archard, J. F., 1957, "Elastic Deformation and the Laws of Friction," Proc. R. Soc. London A, **243**(1233), pp. 190–205.
[247] Jackson, R. L., and Streator, J. L., 2006, "A Multiscale Model for Contact Between Rough Surfaces," Wear, **261**(11–12), pp. 1337–1347.
[248] Angadi, S. V., Jackson, R. L., Choe, S. Y., Flowers, G. T., Lee, B. Y., and Zhong, L., 2012, "A Multiphysics Finite Element Model of a 35A Automotive Connector Including Multiscale Rough Surface Contact," ASME J. Electron. Packag., **134**(1), p. 011001.
[249] Jackson, R. L., Malucci, R. D., Angadi, S., and Polchow, J. R., 2009, "A Simplified Model of Multiscale Electrical Contact Resistance and Comparison to Existing Closed Form Models," 55th IEEE Holm Conference on Electrical Contacts (Holm), Vancouver, BC, Canada, Sept. 14–16, pp. 27–34.
[250] Zhang, X., and Jackson, R. L., 2014, "The Influence of Multiscale Roughness on the Real Contact Area and Contact Resistance Between Real Reference Surfaces," 27th International Conference on Electrical Contacts (ICEC), Dresden, Germany, June 22–26, pp. 1–6.
[251] Wilson, W. E., Angadi, S. V., and Jackson, R. L., 2008, "Electrical Contact Resistance Considering Multi-Scale Roughness," IEEE Holm Conference on Electrical Contacts (Holm), Orlando, FL, Oct. 27–29, pp. 190–197.
[252] Jackson, R. L., Liu, H., and Leray, D., 2013, "A Comparison of the Predictions of a Finite Element Model and Multiscale Model for a Rough MEMS Electrical Contact," 59th IEEE Holm Conference on Electrical Contacts (Holm), Newport, RI, Sept. 22–25, pp. 1–9.
[253] Morag, Y., and Etsion, I., 2007, "Resolving the Contradiction of Asperities Plastic to Elastic Mode Transition in Current Contact Models of Fractal Rough Surfaces," Wear, **262**(5–6), pp. 624–629.
[254] Chung, J. C., and Lin, J. F., 2004, "Fractal Model Developed for Elliptic Elastic-Plastic Asperity Microcontacts of Rough Surfaces," ASME J. Tribol., **126**(4), pp. 646–654.
[255] Persson, B. N. J., 2001, "Elastoplastic Contact Between Randomly Rough Surfaces," Phys. Rev. Lett., **87**(11), p. 116101.
[256] Persson, B. N. J., Bucher, F., and Chiaia, B., 2002, "Elastic Contact Between Randomly Rough Surfaces: Comparison of Theory With Numerical Results," Phys. Rev. B, **65**(18), p. 184106.
[257] Whitehouse, D. J., and Archard, J. F., 1970, "The Properties of Random Surfaces of Significance in Their Contact," Proc. R. Soc. London A, **316**(1524), pp. 97–121.
[258] Ashby, M. F., and Jones, D. R. H., 2013, *Engineering Materials 2: An Introduction to Microstructures and Processing*, Butterworth-Heinemann, Oxford, UK.
[259] Greer, J. R., and Nix, W. D., 2005, "Size Dependence of Mechanical Properties of Gold at the Sub-Micron Scale," Appl. Phys. A, **80**(8), pp. 1625–1629.
[260] Burek, M. J., Budiman, A. S., Jahed, Z., Tamura, N., Kunz, M., Jin, S., Han, S. M. J., Lee, G., Zamecnik, C., and Tsui, T. Y., 2011, "Fabrication, Microstructure, and Mechanical Properties of Tin Nanostructures," Mater. Sci. Eng. A, **528**(18), pp. 5822–5832.
[261] Nix, W. D., and Gao, H., 1998, "Indentation Size Effects in Crystalline Materials: A Law for Strain Gradient Plasticity," J. Mech. Phys. Solids, **46**(3), pp. 411–425.
[262] Bhushan, B., 2008, *Nanotribology and Nanomechanics: An Introduction*, Springer, New York.
[263] Polonsky, I. A., and Keer, L., 1996, "Scale Effects of Elastic-Plastic Behavior of Microscopic Asperity Contacts," ASME J. Tribol., **118**(2), pp. 335–340.
[264] Polonsky, I., and Keer, L., 1996, "Simulation of Microscopic Elastic-Plastic Contacts by Using Discrete Dislocations," Proc. R. Soc. London A, **452**(1953), pp. 2173–2194.
[265] Bhushan, B., and Nosonovsky, M., 2003, "Scale Effects in Friction Using Strain Gradient Plasticity and Dislocation-Assisted Sliding (Microslip)," Acta Mater., **51**(14), pp. 4331–4345.
[266] Jackson, R. L., 2006, "The Effect of Scale Dependent Hardness on Elasto-Plastic Asperity Contact Between Rough Surfaces," STLE Tribol. Trans., **49**(2), pp. 135–150.
[267] Almeida, L., Ishikawa, K., Yu, Q., Jackson, R., and Ramadoss, R., 2006, "Experimental and Theoretical Investigation of Contact Resistance and Reliability of Lateral Contact Type Ohmic MEMS Relays," Proc. SPIE, **6111**, p. 61110F.
[268] Almeida, L., Ramadoss, R., Jackson, R., Ishikawa, K., and Yu, Q., 2007, "Laterally Actuated Multicontact MEMS Relay Fabricated Using Metal MUMPS Process: Experimental Characterization and Multiscale Contact Modeling," J. Micro/Nanolithogr. MEMS MOEMS, **6**(2), p. 023009.
[269] Adams, G. G., Müftü, S., and Azhar, N. M., 2003, "A Scale-Dependent Model for Multi-Asperity Contact and Friction," ASME J. Tribol., **125**(4), pp. 700–708.
[270] Hurtado, J. A., and Kim, K. S., 1999, "Scale Effects in Friction of Single–Asperity Contacts. I. From Concurrent Slip to Single–Dislocation–Assisted Slip," Proc. R. Soc. London A, **455**(1989), pp. 3363–3384.
[271] Hurtado, J. A., and Kim, K. S., 1999, "Scale Effects in Friction of Single–Asperity Contacts. II. Multiple–Dislocation–Cooperated Slip," Proc. R. Soc. London A, **455**(1989), pp. 3385–3400.
[272] Jackson, R. L., Bhavnani, S. H., and Ferguson, T. P., 2008, "A Multi-Scale Model of Thermal Contact Resistance Between Rough Surfaces," ASME J. Heat Transfer, **130**, p. 081301.
[273] Jackson, R. L., Crandall, E. R., and Bozack, M. J., 2015, "Rough Surface Electrical Contact Resistance Considering Scale Dependent Properties and Quantum Effects," J. Appl. Phys., **117**(19), p. 195101.
[274] Goh, C. H., McDowell, D. L., and Neu, R. W, 2003, "Characteristics of Plastic Deformation Field in Polycrystalline Fretting Contacts," Int. J. Fatigue, **25**(9–11), pp. 1047–1058.

[275] Nicola, L., Bower, A. F., Kim, K. S., Needleman, A., and Van der Giessen, E., 2008, "Multi-Asperity Contact: A Comparison Between Discrete Dislocation and Crystal Plasticity Predictions," Philos. Mag., **88**(30–32), pp. 3713–3729.
[276] Sun, F., Van der Giessen, E., and Nicola, L., 2012, "Plastic Flattening of a Sinusoidal Metal Surface: A Discrete Dislocation Plasticity Study," Wear, **296**(1–2), pp. 672–680.
[277] Ng Wei Siang, K., and Nicola, L., 2016, "Contact Between Two Plastically Deformable Crystals: A Discrete Dislocation Dynamics Study," Philos. Mag., **96**(25), pp. 2583–2599.
[278] Lahouij, I., Dassenoy, F., de Knoop, L., Martin, J.-M., and Vacher, B., 2011, "In Situ TEM Observation of the Behavior of an Individual Fullerene-Like MoS_2 Nanoparticle in a Dynamic Contact," Tribol. Lett., **42**(2), pp. 133–140.
[279] Lockwood, A. J., and Inkson, B. J., 2009, "In Situ TEM Nanoindentation and Deformation of Si-Nanoparticle Clusters," J. Phys. D, **42**(3), p. 035410.
[280] Mook, W. M., Nowak, J. D., Perrey, C. R., Carter, C. B., Mukherjee, R., Girshick, S. L., McMurry, P. H., and Gerberich, W. W., 2007, "Compressive Stress Effects on Nanoparticle Modulus and Fracture," Phys. Rev. B, **75**(21), p. 214112.
[281] Bansal, D. G., and Streator, J. L., 2011, "Voltage Saturation in Electrical Contacts Via Viscoplastic Creep," Acta Mater., **59**(2), pp. 726–737.
[282] Brot, C. C., Etsion, I., and Kligerman, Y., 2008, "A Contact Model for a Creeping Sphere and a Rigid Flat," Wear, **265**(5–6), pp. 598–605.
[283] Goedecke, A., Jackson, R. L., and Mock, R., 2010, "Asperity Creep Under Constant Force Boundary Conditions," Wear, **268**(11–12), pp. 1285–1294.
[284] Goedecke, A., and Mock, R., 2009, "Creep Relaxation of an Elastic-Perfectly Plastic Hemisphere in Fully Plastic Contact," ASME J. Tribol., **131**(2), p. 021407.